DECOVALEX THMC TASK E – Implications of Glaciation and Coupled Thermohydromechanical Processes on Shield Flow System Evolution and Performance Assessment

NWMO TR-2008-03   **August 2008**

T. Chan and F.W. Stanchell

Atomic Energy of Canada Limited

Nuclear Waste Management Organization
22 St. Clair Avenue East, 6th Floor
Toronto, Ontario
M4T 2S3
Canada

Tel: 416-934-9814
Web: www.nwmo.ca

DECOVALEX THMC TASK E – Implications of Glaciation and Coupled Thermohydromechanical Processes on Shield Flow System Evolution and Performance Assessment

NWMO TR-2008-03

August 2008

T. Chan and F.W. Stanchell
Atomic Energy of Canada Limited

ABSTRACT

Title:	**DECOVALEX THMC TASK E – Implications of Glaciation and Coupled Thermohydromechanical Processes on Shield Flow System Evolution and Performance Assessment**
Report No.:	**NWMO TR-2008-03**
Author(s):	T. Chan and F.W. Stanchell
Company:	Atomic Energy of Canada Limited
Date:	August 2008

Abstract

A Deep Geologic Repository (DGR) situated on the Canadian Shield will be subject to long-term climate change that will markedly alter surface conditions as a result of glaciation and permafrost penetration. Task E of DECOVALEX THMC[1] is a systematic numerical case study of the subsurface THM processes and mechanisms arising from long-term climate change. The case study focuses on predicting the magnitudes and rates of change in groundwater flow and state of stress caused by time-varying glacial boundary conditions acting on a 1.6-km deep, subregional scale (≈100 km^2), fractured Shield flow system adapted from Sykes et al. (2004) and includes a simplified version of the stochastic Fracture-zone Network Model (FNM) of Srivastava (2002). Transient, 2- and 3-dimensional (2D and 3D) MOTIF finite-element, coupled THM, subsurface simulations were completed. Depth-dependent fluid salinity and temperature-dependent fluid density and viscosity have been included, as well as initial and transient thermal, hydraulic and mechanical boundary conditions developed from two 120,000-year Laurentide glaciation scenario realizations of the University of Toronto's Glacial Systems Model (GSM) (Peltier's 2003). The GSM model provides varying magnitudes and rates of change in basal normal stress, temperature, meltwater fluxes and permafrost evolution.

Selected key findings of Task E coupled THM subsurface modelling include: i) for this particular conceptual model, the flow domain appears to have little memory of previous glacial cycles, with respect to carryover of significant thermal and hydraulic effects; ii) the increase of hydraulic head under ice loading, primarily caused by consolidation effects, is not equal to the total stress imposed by the glacier on the bedrock, but rather is about 1/3 of the glacial basal normal stress, in part due to the ratio between the compressibilities of the rock and the water; iii) the incremental head values resulting from ice loading and HM coupling are relatively uniform throughout the modelled subregion both horizontally and vertically, in contrast to what would occur if one used a hydraulic head boundary condition equivalent to the ice-sheet thickness in an uncoupled flow model; iv) head values in fracture zones (FZs) differ from those in the adjacent rock mass (RM) by a few metres; v) sensitivity analyses showed that a combination of a temperate glacier, very low permeability rock (~10^{-20} m^2) and limited FZ connectivity is necessary for residual anomalous hydraulic heads to persist at depth for thousands of years following deglaciation; vi) during the glacial cycle, Darcy fluxes (velocities) in the FZs and highly permeable RM near surface are on the order of 10^{-2} to 10^{-1} m/a and range between 10^{-7} to 10^{-5} m/a in the RM below 350 m; vii) through using 2D simulations and thereby removing most of the FZ interconnectivity, groundwater velocities in the FZs were reduced by a factor of 100; viii) conservative particle-tracking analysis indicated that 72% of glacial meltwater particles did not penetrate more than 70m below surface and only 6% penetrated to 500m or further[2] below surface; ix) meltwater penetration depths are slightly enhanced by thermal effects, slightly diminished by density effects from depth dependent salinity, slightly enhanced by simulating a smooth glacial topography, hardly influenced by the glacial scenario (within the two scenarios simulated), but severely underestimated by using a 2D model that truncates most of the FZ connectivity; x) during glacial advance/retreat, principal effective stresses are re-oriented, factor of safety is slightly enhanced in the RM and reduced in the FZs.

A limited 2D numerical study was conducted on subregional Shield groundwater flow dynamics under permafrost conditions. A time-invariant, uniform 350-m thick layer of low-permeability (~10^{-19} m^2) rock was used to model the permafrost. Results of the coupled HM simulations with salinity are summarized with a focus on comparing Darcy flux trends with depth with and without permafrost.

DECOVALEX THMC Task E has contributed to an improved understanding of the impact of glaciation on the geosphere including deep flow system behaviour and geomechanical stability. In particular, the application of coupled thermal-hydraulic-mechanical modelling to study glaciation impacts has been demonstrated and the resulting geosphere responses relevant to performance assessment for a DGR have been highlighted.

---

[1] An International Project for DEvelopment of COupled models and their VALidation against EXperiments in nuclear waste isolation involving coupled Thermal-Hydraulic-Mechanical-Chemical processes, 2004-2007.

[2] The meltwater penetration depth might have been overestimated because simplification of the original FNM has led to higher predicted groundwater velocities in FZs.

TABLE OF CONTENTS

TABLE OF CONTENTS

Page

Note: An Addendum to this report contains Attachment 1, Attachment 2 and associated appendices that give further details on Task E activities including conceptual model development and early HM/THM simulations. It is available as a separate document.

LIST OF TABLES

LIST OF FIGURES

LIST OF FIGURES **(continued)**

LIST OF FIGURES **(continued)**

LIST OF FIGURES (continued)

LIST OF FIGURES (concluded)

1. INTRODUCTION

1.1 MOTIVATION AND CONTEXT

A Deep Geologic Repository (DGR) situated on the Canadian Shield will be subject to long-term climate change that will markedly alter surface conditions. This will include periods of prolonged peri-glacial (permafrost) conditions and glacial ice-sheet advance and retreat over the repository site. Transient thermal, hydraulic and mechanical (THM) boundary conditions that result could influence long-term DGR performance. The work reported herein is a systematic numerical case study of the subsurface THM processes and mechanisms arising from long-term climate change. The case study focuses on predicting the magnitudes and rates of change in groundwater flow and state of stress caused by time-varying glacial boundary conditions acting on a 1.6-km deep, subregional scale ($\approx$100 km^2), fractured Shield flow system described in Sykes et al. (2004), which includes a connected Fracture-zone Network Model (FNM) generated by geostatistical methods (Srivastava 2002). The study has been conducted as Task E within the DECOVALEX THMC (DTHMC) framework, an international program with a 4-year duration that began in 2004. DECOVALEX is a multi-disciplinary, co-operative international research effort in modelling coupled Thermo-Hydro-Mechanical-Chemical (THMC) processes in fractured rocks and buffer materials and addressing their role in Performance Assessment for radioactive waste storage (Stephansson et al. 2006). The project deals with several processes of importance for radioactive release and transport. Fourteen funding organizations from industry and regulatory authorities participated in one or more modelling tasks within the project. The primary purpose of Task E is to provide a reasoned basis to support the treatment of long-term climate change in Performance Assessment (PA) and an overall Safety Case for a DGR of used nuclear fuel in a crystalline Shield setting. The Nuclear Waste Management Organization (NWMO) is the lead Funding Organization of Task E and is supported by a research team from Atomic Energy of Canada Limited (AECL). This report presents and discusses the implications of glaciation on several performance related issues based on Task E modelling activities.

The work program of Task E is closely linked and integrated to work programs previously completed under Ontario Power Generation's Deep Geologic Repository Technology Program (DGRTP) including: i) the Subregional Shield Flow System case study (Sykes et al. 2004) ; ii) the international PERMAFROST project (Frape et al. 2004); iii) the Long-term climate change program (Peltier 2003 and 2004) and; iv) the Whiteshell Research area (WRA) Paleohydrogeologic Case Study (Gascoyne et al. 2004).

1.2 BACKGROUND

Within the northern latitudes long-term climate change during the latter half of the Pleistocene (0-1 Ma) has resulted in marked change of surface conditions. Nine glacial events occurred within this time period. During each event it is estimated that peri-glacial (permafrost) and glacial ice-sheet conditions (Peltier 2003) could have existed across the Canadian Shield for approximately 100,000 years. As the ground surface is subjected to changing conditions, from present day boreal to peri-glacial, then followed by variable ice-sheet thickness cover and then rapid glacial retreat (a few thousand years), coincident transient thermal, hydraulic, mechanical, and geochemical conditions will influence groundwater flow system evolution and stability. An

important aspect related to such boundary condition changes is the magnitude and rate of change in hydraulic heads, groundwater flow rates, fracture-matrix fluid chemistry and stress magnitude and orientation; and how such change may influence Shield flow system evolution (e.g., redox front migration; end member chemistry mixing, depth of penetration by recharge) and ultimately the long-term performance of a DGR (e.g. fracture rejuvenation/ propagation/generation; stress re-orientation/magnitude change) at depths of 500-750 m within a fractured crystalline rock environ. In this respect, Task E is focused on increasing the awareness of Site Characterization and Performance Assessment groups as to the impact that Long-term Climate Change has on geosphere stability at time scales relevant to repository performance ($\sim 10^5$ a). By extension, Task E can also serve to demonstrate the possible magnitude and extent of flow system changes that accompanied previous glaciation events, thus providing additional support to present-day hydraulic, hydrogeochemical and isotopic studies of Shield flow systems.

In a previous study known as Benchmark Test 3 (BMT3) of the international DECOVALEX III project Chan et al. (2005) utilized a highly idealized geosphere model based on data from the Whiteshell Research Area (WRA) in Manitoba and transient hydraulic and mechanical glaciated surface boundary conditions generated by the University of Edinburgh's continental scale model of the Laurentide ice sheet (Boulton et al. 2004) to provide an illustrative example that explored the transient mechanical and hydraulic responses of a fractured crystalline rock mass to a glacial cycle. Chan and Stanchell (2005) have demonstrated that the application of a coupled THM code (MOTIF, Guvanasen and Chan 2000) can provide a systematic framework in which reasoned 'insight' or 'what-if' sensitivity analyses can be performed to convey an understanding of local scale groundwater dynamics and change during a glacial event.

Recently, Peltier (2003) has constructed a new class of Laurentide (North American) glaciation models that are able to meet relative sea level and surface geomorphologic constraints, as well as recent geodetic observations. Task E has made use of time-dependent surface thermal and normal stress boundary conditions, as well as glacial meltwater production rates derived from two of Peltier's University of Toronto Glacial System Model scenarios (GSM Realization 2008 and 2778). Making use of site characteristics based on the subregional Shield flow system study (Sykes et al. 2004), Task E subsurface THM modelling was undertaken in order to gain further insight into the evolution of Shield flow systems in response to long-term climate change as it may affect repository performance.

1.3   OBJECTIVE AND SCOPE

A key goal of Task E is to derive a complementary geoscientific basis to address the implications of Long-term Climate Change on groundwater flow system dynamics as it could affect repository performance. In this regard finite-element, subsurface, coupled THMC (salinity) simulations were undertaken on a subregional scale to address the following flow system/geosphere responses associated with a glacial event:

1. Infiltration of glacial meltwaters to the subsurface;
2. Anomalous hydraulic head, which is defined as the difference between the present-day equivalent freshwater head and the corresponding topographically driven head; and
3. Evolution of the state of stress.

In the study the influence on modelled responses to various model parameters, including the degree of coupling of THMC (salinity) processes and model dimensionality (2D vs. 3D), as well as surface boundary conditions including alternative representations of ice-sheet topography, and two alternative glacial scenarios, were investigated.

In addition, a limited numerical study was conducted to simulate groundwater flow dynamics under permafrost conditions.

2. CONCEPTUAL AND NUMERICAL MODELLING

2.1 SITE CHARACTERISTICS

The site characteristics for Task E are based on those used for the subregional scale groundwater flow modelling conducted by Sykes et al. (2004). The latter is part of a 3D numerical case study of groundwater flow within hypothetical regional (1000 km^2) and subregional (100 km^2) scale Shield flow domains (Sykes et al. 2003, 2004). For the subregional flow domain a geostatistical methodology was used to develop multiple realizations of a complex, 3D Fracture-zone Network Model (FNM) constrained by actual, aerial photography-based, surface lineaments and relevant fracture geometry statistics (Srivastava 2002).

For this Task E modelling exercise a single realization of the FNM, identical to the one used by Sykes et al (2004) and designated as Realization 1 (Figure 1), was used. This FNM is comprised of 548 fracture zones and has dimensions of approximately 14.5 km x 13.7 km by 1.6 km (Srivastava 2002).

The model domain developed for the subregional scale groundwater flow study further incorporated GIS data sources such as a digital elevation map (DEM) and digital NTS maps, including a surface hydrology model. Figure 2 depicts the digital elevation map (DEM) and the surface hydrology used in the subregional groundwater flow study. A second-generation site boundary (Site2a), which was somewhat expanded from the earlier version used in Sykes et al (2004) to improve the representation of topographic divides, is also illustrated. The general local topographic gradient is approximately 0.005. Maximum elevation is 420 masl (metres above present-day mean sea level) while the minimum elevation, within southern water bodies, is 350 masl.

The digital files for FNM Realization 1, the DEM, GIS data sets of surface water bodies, streams, wetlands and domain boundaries were transferred electronically by the University of Waterloo to the DECOVALEX THMC Task E research team.

2.2 SIMPLIFYING THE FNM

Practical limitations in construction of the finite element mesh and computer runtime for fully coupled THM analysis required that a systematic approach be applied to reduce the number of FZs to a more manageable number. This requirement was based on experience gained during DECOVALEX III BMT3 modelling activities using AECL's MOTIF code (Chan and Stanchell 2004) and other THM codes (Chan et al. 2005). A systematic and traceable approach utilizing

scientific visualization methods and tools was applied to simplify the full FNM from 548 FZs to 19 FZs. The approach and some results of the early stages of this project are detailed in Attachment 1 and have also been summarized in two conference papers (Chan and Stanchell 2006; Chan et al. 2006). Figure 3 shows the reduced FNM with fracture zones represented as near planar polygons and the Site2a model boundary.

2.3   2-DIMENSIONAL AND 3-DIMENSIONAL CONCEPTUAL MODEL GEOMETRIES

The Site2a boundary (Figures 2 and 3) was also slightly simplified yielding the 3-dimensional (3D) conceptual geometric model illustrated in Figure 4. Most HM and THM simulations for Task E were based on this 3D conceptual model. However, in subsequent investigations addressing the effects of variable salinity, a smoothed glacial topography, alternative glacial scenarios and permafrost conditions (as described in later subsections of the report), it was found that the complexity of these factors combined with the high contrast in hydraulic properties between the rock mass and the FZs presented severe numerical challenges to 3D MOTIF THM modelling. Attempts to overcome the numerical difficulties by finite-element (FE) mesh refinement led to impractical computational times estimated to exceed one month per complete transient run. It was decided to carry out some of the simulations using a 2D conceptual model geometry, which facilitated mesh refinement without excessive computer run time.

Various NE-SW vertical sections were considered, examples of which are depicted by red lines in Figure 5. The section labelled Slice 2 was chosen because it captures more spatial variability in the topographic head gradient (Figure 6) and glacial normal stress gradient (snapshot at a particular time period shown in Figure 7) based on GSM Realization nn2008 as provided by Peltier (private communication 2004, 2006). As well, Slice 2 intersects several different classes of FZs (Figure 8).

2.4   PHYSICAL PROPERTIES

2.4.1   Hydraulic Properties

Hydraulic properties (Table 1) follow those utilized in Sykes et al. (2004). The permeability profile given in this table has been obtained by converting the Case 2 hydraulic conductivity values assigned to 19 model grid layers in Sykes et al. (2004) using freshwater properties at 5°C. Table 2 provides standard handbook values for freshwater density, viscosity and compressibility at two different temperatures. During the conversion, rock mass (RM) layers with identical permeability were combined so that there are seven units in the Task E model domain, with isotropic permeability, k, decreasing with depth from 1.08×10^{-13} m^2 near surface to 1.08×10^{-18} m^2 at depths below 525m and further to 1.55×10^{-19} m^2 at depths greater than 725m below surface. All the FZs were assumed to have the same uniform permeability (1.55×10^{-13} m^2) and porosity. Porosity was assumed to be 0.002 for the background RM and 0.1 for the FZs. Figure 9 illustrates the permeability profiles for the rock mass and for the FZs. The higher permeabilities for the shallow depths represent the presence of moderately fractured rock, while the lower values at depth reflect the dominance of sparsely fractured (SFR) to intact rock. Consistent with the methodology described in Sykes et al. (2004), the elevation of the top unit is governed by the DEM (not 350 m as in Table 1) and the bottom elevations of units 1 to 4

are linearly scaled to account for the variation in thickness between the actual ground surface and an elevation of zero.

Table 1: Hydraulic Properties of Rock Mass and Fracture Zones

Unit	Elevation (m)	Thickness (m)	Permeability (m^2)	Porosity	Zone Type
1	$350^1 \rightarrow 340^1$	10	1.08×10^{-13}	0.002	Overburden
2	$340 \rightarrow 280^1$	60	1.08×10^{-14}	0.002	Shallow rock
3	$280 \rightarrow 200^1$	80	1.24×10^{-16}	0.002	Shallow rock
4	$200 \rightarrow 0^1$	200	1.08×10^{-17}	0.002	Middle rock
5	$0 \rightarrow -200$	200	4.64×10^{-18}	0.002	Deep rock
6	$-200 \rightarrow -375$	175	1.08×10^{-18}	0.002	Deep rock
7	$-375 \rightarrow -1400$	875	1.55×10^{-19}	0.002	Deep rock
	All fracture zones	20	1.55×10^{-13}	0.1	Fracture zones

[1] Top elevation of Unit 1 varies according to DEM. Bottom elevations of Units 1 to 3 are linearly scaled between the DEM and the mean sea level (0 elevation)

Table 2: Fresh Water Properties (after DeMarsily 1986)

Temperature	5°C	25°C
Fluid Compressibility	4.928×10^{-10} Pa^{-1}	4.524×10^{-10} Pa^{-1}
Fluid density	1.000×10^3 kg/m^3	9.970×10^2 kg/m^3
Fluid viscosity	1.518×10^{-3} Pa·s	8.900×10^{-4} Pa·s

For THM modelling (with/without salinity) the equations of state for water density and viscosity followed those given in Chan et al. (1999).

2.4.2   Thermal, Mechanical and Hydroelastic Properties

Table 3 lists the thermal, mechanical and hydroelastic properties of the rock mass and the FZs. The following mechanical properties were assumed for the RM: density = 2650 kg.m^{-3}; Poisson's ratio = 0.25; Young's modulus = 20 GPa for 0≤depth≤150m, 30 GPa for 150m≤depth≤350m and 60 GPa for depth≥350m; tensile strength = 6 MPa; and Hoek-Brown (1988) parameter m = 25 and s = 1. For the FZs Poisson's ratio = 0.25, Young's modulus = 5 GPa, cohesion = 3 MPa and friction angle = 25°. Biot's (1941) hydroelastic coefficient, α, was assumed to be 0.73 everywhere. The rationale for the choice of the majority of these values has been discussed in Attachments 1 and 2. Initially, the shear strength parameters

(cohesion = 0 MPa and friction angle = 30°) listed in Table 2 of Attachment 1 were utilized to evaluate the Coulomb failure criterion for the FZs (see below). However, it was found that this set of strength parameters would cause all FZs to fail under the present-day (nonglacial) in situ state of stress assumed for Task E (see below). Thus the initial choice of the combination of stress and strength were inconsistent. Subsequently, an attempt was made to adjust the strength parameters until no FZ would fail under nonglacial in situ stress. Unfortunately, it was found that this could only be achieved using unrealistic FZ strength parameters. Eventually, the FZ shear strength parameters for BMT3 (Chan et al. 2005) were adopted for Task E. The consequence of this approach will be further discussed with the modelling results.

**Table 3: Thermal, Mechanical and Hydroelastic Properties of
Rock Mass and Fracture Zones**

Property	Rock Mass	Fracture Zones
Young's modulus E	Shallow rock: 20 GPa Middle rock[a]: 30 GPa; Deep rock[a]: 60 GPa	5.0 GPa
Poisson's ratio ν	0.25	0.25
Biot's coefficient, α	0.73	0.73
Cohesion	16.7 MPa	3.0 MPa
Friction angle	54°	25°
Tensile strength	6 MPa	0 MPa
Uniaxial compressive strength	150 MPa	N/A
Hoek-Brown parameter m	25	N/A
Hoek-Brown parameter s	1	N/A
Thermal conductivity	3.0 W/(m °C)	2.5 W/(m °C)
Specific heat	1.0 kJ/(kg °C)	1.0 kJ/(kg °C)
Density	2650 kg/m^3	2400 kg/m^3
Coefficient of linear thermal expansion	10 x 10^{-6}/°C	10 x 10^{-6}/°C

[a] See Table 1

In the rock mass we assumed that the Hoek-Brown failure criterion (Hoek and Brown 1988), which was originally given in terms of total stress, still holds for coupled THM analysis when it is expressed in terms of effective stress as follows:

$$\sigma'_{1f} = \sigma'_3 + \sqrt{m\sigma_c\sigma'_3 + s\sigma_c^2}$$

(1)

with:

σ'_{1f} = major effective principal stress at failure, and

σ'_3 = minor effective principal stress.

σ_c is the uniaxial compressive strength, and m and s are empirical constants. In OPG-Specs (Appendix A of Nguyen 2004), the Hoek-Brown criterion, with recommended values of σ_c, m and s, is given in terms of total stress. Herein, we assumed the validity of the same expression of the criterion in terms of effective stresses, with the same parameters. The effective stress is defined as:

$$\sigma'_{ij} = \sigma_{ij} - p\delta_{ij}$$
(2)

with:

σ'_{ij} = effective stress
σ_{ij} = total stress
δ_{ij} = Kroenecker delta
= 1   (i = j) and 0 (otherwise)
p = pore pressure.

It should be noted that following the recommendation of Bouteca and Gueguen (1999) based on their experimental and theoretical studies, we are using Terzaghi's effective stress (with Biot's hydroelastic coefficient, α = 1) in the failure criterion, but Biot's effective stress (with α = 0.73) in the constitutive relationship in the MOTIF THM model.

Coulomb's shear failure analysis with a linear Mohr envelope (see Jaeger and Cook 1976) was adopted for the fracture zones. The Mohr-Coulomb failure criterion (adapted for a saturated rock mass) states that shear failure will occur when the effective shear stress τ' across a critical plane reaches the critical value:

$\tau_c' = c + \sigma_n'\tan \phi$
(3)

where τ_c' is the shear strength in terms of effective stress, σ_n' is the effective normal stress across this plane; c is the cohesion and ϕ is the internal friction angle. As mentioned previously, the BMT3 values of cohesion (3 MPa) and friction angle (25°) were adopted for Task E.

A fracture zone was treated as a plane of weakness. To analyze its thermomechanical stability we resolved the effective stress tensor calculated by the THM model into its normal and shear components, σ_n' and τ', across the fracture plane using the following equations (Jaeger and Cook 1976):

$$\sigma'_n = \ell_1^2\sigma'_1 + \ell_2^2\sigma'_2 + \ell_3^2\sigma'_3$$
(4)

where
σ'_1 = major principal effective stress,
σ'_2 = intermediate principal effective stress,
σ'_3 =   minor principal effective stress, and
ℓ_1, ℓ_2, ℓ_3 =   direction cosines of the normal to the fracture plane with reference to the principal axes.

It should be mentioned that both the principal effective stress magnitudes and the direction cosines vary with time in the THM model of glacial loading/unloading.

The resultant stress R is given by:

$$R = (\ell_1^2 \sigma_1'^2 + \ell_2^2 \sigma_2'^2 + \ell_3^2 \sigma_3'^2)^{1/2} \tag{5}$$

The effective shear stress acting across the fracture plane is:

$$\tau' = (R^2 - \sigma_n'^2)^{1/2} \tag{6}$$

To determine whether the rock would fail, we substituted the value of σ_n' obtained by Equation (4) into Equation (3) to calculate the effective shear strength τ_c' and compared it with the effective shear stress value τ' calculated by Equation (6). This comparison was expressed as a factor of safety (SF):

$$SF = \tau_c' / |\tau'| \tag{7}$$

If FS>1, the fracture zone would be stable. If FS≤1, shear failure would occur. It should be noted that since Equation (3) is valid for shear failure analysis under compressive normal effective stress ($\sigma_n' \geq 0$), $\tau_c' \geq 0$.

Tensile failure was evaluated by comparing any tensile effective normal stress with the appropriate tensile strength.

2.5   NUMERICAL DISCRETIZATION

For 3D simulations the model domain in the 3D conceptual model (Figure 4) was discretized with a mesh comprising 40,005 nodes and 36,447 hexahedral elements, as depicted in Figure 10, along with the FZs, which were assumed to have a uniform thickness of 20m for all coupled modelling in Task E. An automatic mesh generator PATRAN^{TM} was utilized to develop this mesh. The choice of PATRAN input parameters, e.g., maximum number of nodes and element aspect ratio, used for this mesh generation was based on a compromise amongst various factors, including the need for mesh refinement at interfaces between material property zones, general rules of thumb governing element shape (mostly built into PATRAN) and computational time for fully coupled transient THM MOTIF modelling given the computer hardware available to this project at AECL. Experience gained in the DECOVALEX III BMT3 study had guided the Task E mesh construction process. Several trials were necessary to arrive at an appropriate mesh. Using this 3D mesh, computer run time for a transient THM simulation with variable salinity was slightly under two days.

For 2D simulations the model domain in Slice 2 conceptual model (Figure 8) was discretized using approximately 7,500 nodes and 3600 quadrilateral elements (Figure 11), based on similar considerations to those described for 3D modelling above. Using this 2D mesh, computer run time for a transient THM simulation with variable salinity was somewhat less than two hours.

2.6   BOUNDARY CONDITIONS

2.6.1   Overview

Spatially and temporally varying thermal, hydraulic and mechanical boundary conditions during the last glacial event were derived from two of Peltier's (private communications 2004, 2005 and 2006) glacial scenario realizations using the University of Toronto Glacial Systems Model (GSM). These were Realization nn2008, which is referred to as the Base Scenario Realization, and Realization nn2778, which is one realization of a temperate glacial scenario. To facilitate the simulation of variable ice sheet thickness across the subregion, the time series of basal normal stress was provided at nine (1° longitude x 0.5° latitude or 69.03 km x 55.61 km) grid cells of the continental-scale glaciation model, approximately centred on the smaller subregional domain. The modelled subregion was contained within Cell 5 of the continental-scale model, as depicted in the normal stress time series for Realization nn2008 in Figure 12. Temperature and meltwater flux at the base of the ice sheet were each provided as a time series at grid Cell 5 only from the continental-scale glaciation model. As the time evolution of Cell 5 basal temperature and normal stress for the two realizations (Figures 13 and 14) shows, there were three cycles of glacial loading/unloading over the subregion during the past 121, 000 years. The two realizations differ primarily in the basal temperature evolution. According to nn2008 (Figure 13) basal temperature is below the pressure-adjusted freezing point of freshwater throughout the 121, 000-yr glacial event except for ~2, 000 years towards the end of this period. In contrast, Realization nn2778 predicted extended periods of basal melting during periods of ice sheet coverage (Figure 14). For the purpose of this report Realizations nn2008 and nn2778 will be referenced as "cold-based" and "warm-based" scenarios, respectively. Figure 15 depicts the basal meltwater production rate for these two scenarios. It should be noted that the melting rate is well below 10 cm/yr most of the time.

2.6.2   Mechanical Boundary Conditions

As is evident from Figure 12, the basal normal stress values for the nine cells are not identical, but indicate a certain degree of spatial variability. This is to be expected since the modelled subregion is not directly beneath one of the domes of the continental glacier at any time. For this reason, adopting an approach to mechanical boundary conditions that assumes the ice sheet thickness to be uniform and equivalent to the Cell 5 value across the model domain at every time step was not favoured. Instead, a more realistic, and necessarily more complicated, approach was utilized. At each time step, the nine values of basal normal stress were bilinearly interpolated to yield an areal variation over the ground surface in the Task E model domain. This interpretation of the GSM normal stress output was undertaken to help investigate the impact of the variable shape of the ice front/terminus as the ice sheet advanced and retreated across the model domain.

Figure 16 depicts the interpolated glacial basal normal stress contours from the "cold-based" scenario (GSM Realization nn2008) for several time steps during the third, or most recent, advance/retreat cycle. Note that the values of the colour legend change as normal stresses increase or decrease between time steps. From the interpolations in Figure 16, it can be observed that: i) large-scale advance and retreat of the ice sheet tends to occur in a ENE-WSW direction across the modelled subregion; ii) while the ice sheet tends to be primarily thinner towards the WSW, fluctuations do occur during the peak thickness period that can result in the

ice sheet thinning in other directions, such as to the NW or NE; iii) during the large-scale advance/retreat periods (~30.4 to 29 ka BP and ~12.6 to 11 ka BP), the variability in ice sheet thickness across the subregion could be 100 to 150 m; iv) throughout most of the third cycle (~27 to 13 ka BP), the variability of ice sheet thickness could be within a few 10's of metres; and iv) at the LGM (at ~24 ka BP) the spatial variability of the ice sheet thickness falls in the 5 to 10-m range.

Two approaches have been taken at different stages of the Task E study. Early in the project the interpolated spatially variable normal stress was directly superimposed as distributed mechanical load on the actual subregional ground surface topography as given in the DEM (Figure 2) without any further processing. Hereafter this will be called the "real (land) topography" approach. While this approach honours all data in a straightforward manner, the ground surface topography is reflected in the glacial surface topography. In reality, given the 100, 000-year time scale we are modelling, the viscoplastic ice would have flowed and filled up the depressions in the land, resulting in a smoother ice-sheet surface. Therefore, a more realistic approach is to apply a mechanical stress boundary condition such that the glacial surface topography from the GSM scenarios is reproduced. This was achieved by adjusting the areal distribution of basal normal stress given by GSM nn2008 by an amount equivalent to the difference between the subregional ground surface topography and the continental scale ground surface topography used in the GSM. This was the approach adopted at a later stage of Task E numerical modelling. This approach will be called "smoothed (ice-sheet) topography" approach.

While the "smoothed (ice-sheet) topography" approach better represents the rheology of ice, the resulting smaller gradient in glacial normal stress, which is the main driving force of the dynamics of the subsurface THM system, leads to numerical difficulties with 3D MOTIF THM modelling with variable salinity. Consequently, 2D modelling with more refined discretization was undertaken in an attempt to overcome these numerical difficulties.

As the rock mass is assumed to be a linear poroelastic medium in MOTIF, only the glacial loading was applied as mechanical boundary conditions to the top surface. Zero-displacement (roller) boundary conditions were assumed at the bottom and perimeter boundaries. The MOTIF HM and THM simulations calculated effective stress changes. These were superimposed onto the far-field in situ stress (given in Equations (8) – (10) in a later subsection) prior to the evaluation of the factor of safety.

2.6.3   Hydraulic Boundary Conditions

During glaciation, time-dependent infiltration flux boundary conditions, as provided by the basal meltwater production rate from the continental glaciation model, were applied to the top boundary of the Task E subregional model with zero-flux during periglacial periods or periods when the basal temperature of the ice sheet has been predicted to be below the pressure-adjusted freezing point. During the approximately 11, 000 years after the ice sheet has retreated completely from the subregional model domain, an infiltration flux of 3 mm/year, based on the work of Thorne and Gascoyne (1993) at the WRA, was assumed to represent typical Shield surface condition. The bottom boundary was assumed to be a no-flow boundary. All perimeter boundaries were assigned spatially and temporally varying head boundary conditions. During nonglacial periods these boundary values corresponded to hydrostatic head values equal to the ground surface elevation. Initially, it was planned that (vertical) perimeter boundary head values under glacial conditions would be estimated using an auxiliary column

HM model with the time-varying ice-sheet normal load applied to the top boundary and no-flow boundary conditions at the bottom. It was found, however, by numerical testing with a constant normal load that this coupled HM column settled to an equilibrium solution with a hydrostatic head approximately equal to 1/3 times the normal stress converted to equivalent freshwater head units, plus the initial head, which is practically equal to the elevation head. Thus, as illustrated in Figure 17 for an idealized glacial loading/unloading history, the calculated HM equilibrium head curve (red) is completely hidden by the blue line, which represents the relationship,

Equivalent freshwater head change = 1/3x [ice-sheet basal normal stress]

It should be noted that each point on the calculated head curve has been obtained from the HM equilibrium column model with a top boundary normal stress given by the ice-sheet thickness (black curve) converted to normal stress units at the same time.

Figure 18a-e illustrates for six of the many nodes along the perimeter of the Task E subregional model (Figure 18a) the time evolution of ice-sheet basal normal stress and hydraulic head for the cold-based glacial scenario (Figures 18b and 18c) and for the warm-based scenarios (Figures 18d and 18e). Inspection of these figures and corresponding numerical model outputs indicates that both the ice-sheet thickness and the hydraulic head vary along the perimeter boundary, although the difference between values at the various locations may not be always conspicuous due to the plotting scale.

Ideally, the mechanical and hydraulic boundary conditions at the vertical sides should have been calculated using a larger HM or THM model. For 3D modelling this is beyond the scope of the Task E study. For 2D modelling the impact of side boundary conditions was tested using an extended model and it was found that the values of the output variables did not differ appreciably from those obtained using the methodology for assigning the vertical side boundary conditions described in the preceding paragraphs of this subsection.

2.6.4   Thermal Boundary Conditions

Thermally, the top boundary (ground surface) was assumed to be an isothermal surface with a time-dependent temperature provided by Peltier (2004); all perimeter boundaries were treated as adiabatic (no-heat flow) boundaries. Figures 13 and 14 depict the complex and dynamic evolution of ground surface temperatures and ice-sheet basal normal stress appropriate to the subregional Shield modelling domain from the continental-scale GSM Realizations nn2008 and nn2778. The bottom boundary was also treated as a prescribed isothermal boundary with a time-varying temperature determined by means of preliminary thermal modelling using a 3-km vertical column MOTIF heat conduction model using the thermal properties given in Table 3. For the thermal column model we assumed a constant upward geothermal heat flux of 60 mW/m^2 flowing through the bottom boundary, as was done in Peltier's 1D heat conduction model, which extended to 3 km below ground surface. The time-varying temperature calculated at 1.6 km below ground surface by this 1D simulation run was assigned as the bottom boundary condition for MOTIF THM modelling.

2.7 INITIAL CONDITIONS

2.7.1 Initial Mechanical Conditions

Initially the rock mass was assumed to be in static mechanical equilibrium under the non-glacial in situ state of stress with zero displacement everywhere. Based on the recommendation of Kaiser (2004) the following equations were used for the present-day (interglacial), far-field in situ stress state for Task E:

$$\sigma_1 = \sigma_H = 0.041 MPa/m_{depth} + 10.08 MPa \tag{8}$$

$$\sigma_2 = \sigma_h = 0.030 MPa/m_{depth} + 5.37 MPa \tag{9}$$

$$\sigma_3 = \sigma_v = 0.0265 MPa/m_{depth} \tag{10}$$

where

σ_H = maximum horizontal stress, oriented in the E-W direction,
σ_h = minimum horizontal stress, and
σ_v = vertical stress;

and
σ_1, σ_2, σ_3 are the major, intermediate and minor principal stresses respectively.

2.7.2 Initial Hydraulic Conditions

Initial hydraulic heads were determined from a steady-state MOTIF HM or THM simulation, as appropriate for the case, assuming non-glacial topographic head surface boundary conditions and zero-displacement along the bottom and perimeter boundaries.

2.7.3 Initial Thermal Conditions

For Task E THM modelling temperatures from Peltier's (2004) thermal model at 121 ka BP were assigned as initial thermal conditions.

2.8 NUMERICAL MODELLING

The MOTIF Galerkin finite-element code was utilized to solve the thermoporoelastic equations of heat transfer, fluid flow and mechanical equilibrium (Guvanasen and Chan 2000), which are natural extensions of Biot's (1941) theory of poroelasticity. The coupled THM simulations calculate temperatures, hydraulic heads, linear groundwater velocities, displacements and effective stress changes. These effective stress changes were superimposed onto the contemporary far-field in situ stress prior to the evaluation of the factor of safety.

Various 2-dimensional (2D) and 3-dimensional (3D) MOTIF simulations were performed to investigate the subsurface THM responses to glacial loading/unloading cycles using different degrees of coupling and different approximations of glacial boundary conditions. Table 4 summarizes the simulation runs that are utilized in this report to address the performance related issues.

Table 4: Summary of Simulation Runs to be Presented in this Report

Simulation Run	Description
3D[a] R_HM	Glacial normal stress superimposed on actual subregional topography
3D R_THM	As above but includes thermal-hydraulic and thermomechanical coupling
3D S_THM	Smooth glacial topography as per GSM scenario nn2008 (Peltier, private communication 2004, 2006)
3D R_THMC	As for R_THM[b] but includes saline groundwater with specific gravity 1.10 below elevation −375 masl (approximately 725m below surface)
2D[c] HM	As for R_HM but 2D Slice 2 vertical section model with smooth glacial topography (see text for description)
2D THM[d]	As for S_THM but 2D Slice 2 vertical section model with smooth glacial topography
2D THMC	As for R_THMC but 2D Slice 2 vertical section model with smooth glacial topography
2D HMC_P350	As for 2D HM but includes saline groundwater with specific gravity 1.10 below elevation −375 masl and 350m thick permafrost

Notes:

[a]   All 3D runs used cold-based glacial scenario GSM nn2008.
[b]   The qualifier 3D will be omitted when there is no ambiguity.
[c]   All 2D runs simulated smooth glacial topography.
[d]   There are two such runs, one using GSM nn2008 (understood unless otherwise stated) and the other using GSM nn2778.

It should be noted that only the density effect of salinity was included in the simulations labeled "C". Attempts at simulations including groundwater viscosity as a function of salinity failed to yield acceptable solutions due to numerical instability problems. However, both density and viscosity are temperature dependent.

3. INFILTRATION OF GLACIAL MELTWATERS

3.1   THE ISSUE

An important issue with respect to flow system evolution and repository performance is the influence of climate change and glaciation, and altered physical and chemical boundary conditions on redox stability at the repository horizon. With regard to glaciation, the question is whether altered hydrogeologic conditions could potentially allow oxygenated recharge water to reach typical repository depths. Gascoyne et al. (2004) investigated the stability of a groundwater system in a fractured crystalline rock environment in a previous

paleohydrogeologic case study of the Whiteshell Research Area (WRA) in eastern Manitoba, near the western edge of the Canadian Shield. This study found no substantive indicators for low-temperature mineral reactions with oxidizing waters below a depth of 50 metres. These results were further corroborated by reactive chemical transport modelling (Spiessl et al. 2006).

During a glacial event transient hydraulic heads and transient groundwater flux are expected. In this section we examine the potential penetration of glacial meltwaters by means of advective/convective particle tracking using the TRACK3D code (Nakka and Chan 1994) based on the flow field predicted by coupled THMC (THM with depth-dependent salinity) modelling. The results of Simulation 3D R_THMC, which made use of the cold-based glacial scenario nn2008 (Table 4) and included all the relevant coupled processes, were utilized for this purpose. It should be emphasized that the penetration depth estimated by this type of particle-tracking analysis represents an absolute maximum for the particular conceptual model since diffusion, dispersion, sorption and chemical interactions are not simulated.

Results from other simulations will also be presented and compared to illustrate the influence of various model parameters, including: a) degree of coupling of THMC (salinity) processes, b) top boundary conditions, i.e., ice-sheet topography, c) fracture zone orientation and interconnectivity, d) model dimensionality (2D vs. 3D), and e) glacial scenario ("cold-based vs. "warm-based" glacier).

3.2   MODELLING RESULTS AND DISCUSSIONS

Twelve (12) points, as illustrated in Figure 19, were selected for graphical display of time evolution of dependent variables. These points were selected at different locations and elevations to illustrate a possible range of coupled THM responses in the permeable fracture zones (Points 1, and 12), fracture zone intersections (Points 4-7) and the less permeable rock mass (Points 2, 3, and 8-11(in a vertical line through the origin)). Table 5 summarizes the physical location and elevation for each of these 12 points.

Table 5: Location and Elevation of the 12 Points Selected for Graphic Display

Location No.	Physical Location	Elevation (m)
1	Fracture – V16	-340
2	Rock	-360
3	Rock	-340
4	Fracture – H2 & V13	185
5	Fracture – H5 & V16	150
6	Fracture – H6, V8 & V9	280
7	Fracture – H5 & V15	80
8	Rock	380
9	Rock	0
10	Rock	-360
11	Rock	-700
12	Fracture - V10	-85

3.2.1 Hydraulic Head and Darcy Flux Magnitude

Figure 20 depicts the temporal evolution of the subsurface equivalent freshwater head at the 12 selected points throughout the simulated glacial-interglacial period. It should be noted that the time axis has been labelled in increasing time since the first simulated time[3] step (at 121.0 ka BP) prior to the first ice-sheet advance/retreat cycle. During glaciation, the evolution of equivalent freshwater head follows the advance/growth and retreat/decay of the ice sheet. The Shield subregional flow system appears to have little memory of previous glacial cycles, with head values returning to non-glacial conditions shortly after each cycle. Consolidation effects due to glacial loading increase the equivalent freshwater head by somewhat more than 1/3 of the normal stress that the ice sheet imposes on the bedrock. For glacial Cycle 3, the maximum (total) equivalent freshwater head (initial nonglacial head plus glacially induced head) in the subsurface is in excess of 1,450 m. Note that the head values are relatively uniform throughout the modelled subregion both horizontally and vertically, except at depths greater than 725 m below ground surface where denser saline water gave rise to a vertical head gradient (see below).

In Figures 21 and 22 we have plotted the horizontal variation of equivalent freshwater head at –320 masl (approximately 670m below surface) and the vertical profile through the model origin at various stages of the third glacial cycle. During glacial advance and retreat across the subregion the horizontal hydraulic gradient is steeper than the nonglacial topographically driven hydraulic gradient (approximately 0.003 at 75 kyr) by up to a factor of two, while at the Last Glacial Maximum (LGM, at 97 kyr) the hydraulic gradient is slightly less than the nonglacial condition. It should be noted that superimposing the spatially variable glacial normal stress onto the actual land surface topography might have exaggerated the predicted horizontal hydraulic gradient around the time of the LGM. The effect of a smooth ice-sheet surface will be examined in a later subsection.

Vertical equivalent freshwater head gradient (Figure 22) in the rock mass down to the top of the saline groundwater unit (elevation –375 masl) is small throughout the glacial cycle, considering the enormous normal stress imposed by the glacier. Although not easily visible because of the large horizontal (head) scale, from surface to approximately 725m below, the mean vertical head gradient is less than 0.05. This is in sharp contrast to the very high vertical hydraulic gradients (>3) predicted over certain depth ranges in BMT3 (Chan et al. 2005). A plausible explanation may be as follows. In BMT3 prescribed head boundary conditions, calculated by G. Boulton's continental glaciation modelling team at the University of Edinburgh (see Chan et al. 2005), were applied to the top of the local subsurface HM model. In this case the subsurface flow dynamics resulted from two driving forces, the very high top boundary heads and the poroelastic drive due to the normal stress applied to the top. In BMT3, as was shown by coupled flow simulations much of the subsurface hydraulic gradient was due to the head boundary conditions. In Task E the basal meltwater production rates, which were applied to the top boundary of the subsurface model, were orders of magnitude lower than those that corresponded to the BMT3 head boundary conditions. Thus, in Task E there is essentially only one driving force, the poroelastic driving force due to the boundary normal stress. Since the

---

[3] Unless otherwise stated, all modelling results are reported in the modelling time scale such that t = 0 is 121 ka BP; the main phase of glacial Cycle 3 started at t = 90.6 kyr (30.4 ka BP); the LGM occurred around t = 101 kyr (20 ka BP); rapid retreat/decay of the glacier occurred around t =106.6 kyr (14.4 ka BP); glacial meltwater production started at t = 107.6 kyr (13.4 ka BP) and ends at t = 109.6 kyr (11.4 ka BP).

rock mass has been assumed to be linear poroelastic, vertical ice mechanical loading causes instantaneous compression of the pore space, yielding instantaneous increase in hydraulic head, which is essentially independent of depth. Below 725-m depth the equivalent freshwater head increases quite rapidly with depth due to the higher density of the assumed saline groundwater. In fact, the equivalent freshwater head gradient in the saline water unit is, in general, approximately 0.1, i.e., nearly the same as the hydrostatic head gradient in a column of saline water with specific gravity 1.1. The high equivalent freshwater head[4] gradient is not indicative of high upward Darcy velocity, which has to be calculated from the pressure gradient and the gravitational force gradient considering the saline water density[5].

Figure 23 depicts the head distribution at LGM near two FZs according to the 3D R_HM model. In this case the head values in each FZ differ from the adjacent RM by no more than a few metres. At other times head differences between FZs and the adjacent RM may be marginally larger but are still just a few metres. Generally similar results were obtained from all Task E simulations.

Figure 24 illustrates the temporal evolution of the resultant Darcy flux (also known as Darcy velocity) magnitude ($|\mathbf{q}|$) at the 12 selected locations during the three cycles of glacial advance/retreat. The Darcy flux magnitudes fall into two groups: i) Absolute values on the order of 10^{-2} to 10^{-1} m/a at Points 1, 4-7, and 12 in the FZs at various elevations, plus Point 8 in the high-permeability rock mass (actually overburden) near ground surface[6]; and ii) Absolute values on the order of 10^{-7} to 10^{-5} m/a at Points 2, 3, and 9-11 in the rock mass at depths of 350 m or more below ground surface. However, pulse-like spikes, with half-width[7] of approximately 200 years, do occur coincident with advance/retreat of the glacier across the modelled subregion in each of the three cycles. During the advance/retreat stages, the simulated Darcy flux magnitudes reached peak values of 4×10^{-5} m/a at Points 2 and 3 (near FZ V16) at approximately 670 m below ground surface and 6×10^{-5} m/a at Point 9 at 35-m depth. Elsewhere peak values of Darcy flux magnitudes rarely reach 2×10^{-5} m/a. A Darcy flux of 10^{-5} m/a corresponds to an average linear groundwater velocity of 5 mm/a.

For the geometry, hydraulic properties and cold-based glacial scenario (nn2008) simulated, Darcy flux magnitudes generally vary within a factor 2 or 3 in the FZs and within an order of magnitude in the rock mass during the glacial loading/unloading cycles.

3.2.2   Particle-tracking Results

As the most conservative estimate of glacial meltwater infiltration and recharge to the subsurface, advective/convective particle tracking was performed from ground surface. A total of 2432 water-coincident particles (i.e., without diffusion and dispersion) moving under the flow

---

[4] Equivalent freshwater head h_f is calculated as: $h_f = p/(\rho_f g) + z$, where p is the fluid pressure predicted by the MOTIF THMC model with depth dependent density; ρ_f = freshwater density; g = gravitational acceleration and z = elevation (masl). In saline groundwater the fluid pressure is higher than the freshwater hydrostatic pressure because of the higher density.

[5] Vertical Darcy velocity $q_z = (k/\mu_s)\partial/\partial z (p + \rho_s gz)$, where μ_s and ρ_s are the viscosity and density, respectively, of saline groundwater.

[6] Darcy flux in FZ might have been over-estimated by up to an order of magnitude as a consequence of FNM simplification.

[7] Pulse duration measured at half peak value.

field from the 3D R_THMC simulation were followed from their initial surface locations at the beginning of meltwater production at 107.6 kyr to the present (121 kyr) and slightly beyond. Figure 25 illustrates the starting locations, and the plan view and vertical plane projections of thirty-eight (38) of the particle paths. All the 38 particles illustrated except one were started at random surface locations in FZs in an attempt to acquire a general understanding of meltwater behaviour. Although the majority of particle paths shown in Figure 25 are confined within the upper portion of the model domain, at least one path penetrates to typical repository depths of 500-750 m. Histograms of maximum meltwater penetration depth (as represented by 2432 particle paths) and time to reach maximum depth are plotted in Figures 26-28. The normalized histogram in Figure 26 indicates that 80% of the meltwaters recharge to ≤100m below surface. Figure 27 further shows that approximately 17% of the meltwaters did not recharge below the 10-m thick overburden and could exit the model as surface water; another 55% did not penetrate beyond the shallow rock layer (10m-70m). A small percentage (<6%) of meltwaters did penetrate to a 500-m depth or greater. Over 85 % of all the water-coincident particles reached the maximum recharge depth during the 2000-year melting period of the glacier (Figure 28).

One must bear in mind that the 6% of particles that recharged to great depth in the above particle-tracking analysis represent only the advective movement of a small percentage of meltwater. After recharging through the rock formation, the meltwater would not retain its original chemical characteristics through diffusion, dispersion and reaction with the surrounding rock mass (Spiessl et al. 2006).

3.2.3   Impacts of Physical and Geometrical Attributes of the Model

In this subsection we examine the impacts on meltwater recharge of salinity, thermal coupling, fracture zone orientation and interconnectivity, ground surface boundary conditions and model dimensionality.

3.2.3.1 Impact of Salinity

Saline water is denser and more viscous than freshwater. In the conceptual model for the saline groundwater THMC simulations for this Task E study, saline water lies below freshwater at a specified elevation. For our simulated situation, the relevant mechanism associated with saline water is that its higher density may be expected to cause lower Darcy velocity at depth, thus generally improving the barrier performance of the geosphere.

In the event of a glaciation/deglaciation cycle over a domain where the subsurface environment is characterized by increasing groundwater salinity with depth, a pertinent question is whether saline water would act to retard or alter the movement of groundwater, thereby limiting the recharge depth of glacial meltwaters that infiltrate into the subsurface.

As expected, a comparison of corresponding freshwater (R_THM) and saline water (R_THMC) model predictions does indicate that salinity leads to shallower recharge of meltwater "particles" (Figures 29 and 30). In the freshwater model, 85% of meltwater particles would not recharge to depths greater than 500m below surface (Figure 29), which is the upper limit of the range of DGR depths considered, while 58% of recharge (Figure 30) would not penetrate below the bottom of the shallow rock unit (Unit 2), which lies 70m below surface. With saline water of specific gravity 1.1 represented in the lowest permeability unit (below an elevation of -375 m),

these percentages would become 94% (Figure 29) and 72% (Figure 30), respectively. Concomitant with shallower recharge, it also would take somewhat shorter time for meltwater particles to reach their maximum recharge depth in the saline water case. As shown in Figure 31, whereas 77% of meltwater recharge would attain maximum penetration within the 2000-year glacier-melting period in the freshwater R_THM simulation, this percentage would increase to 85% in the R_THMC saline water run.

3.2.3.2 Impact of Thermal Coupling

The transient temperature field that is associated with long-term climate change and continental glaciation affects a Shield flow system through variation of groundwater density and viscosity with temperature, thermal hydraulic coupling and thermal mechanical coupling. Inspection of normalized histograms for maximum meltwater penetration in Figure 32 reveals that 2.5% of the meltwater particles penetrate to depths of 500 m or more in the R_HM model, whereas the corresponding percentage increases to 15% when the thermal effect is included in the R_THM model Presumably, this is due to a combination of higher groundwater velocity that has resulted from reduced viscosity in the warmer water at depth and a downward density gradient between colder, near-surface water and warmer, deeper water.

3.2.3.3 Impact of Fracture Zone Orientation and Interconnectivity

In Canadian Shield settings, groundwater movement occurs predominantly in fractures and fracture zones. Consequently, it is important to understand how fracture zone orientation and interconnectivity would affect groundwater flow velocity and glacial meltwater recharge during a glacial event.

In this subsection, simulation results from Run R_THMC are examined in an attempt to delineate the impact of FZ orientation and interconnectivity. Furthermore, when a 2D sectional model approximates a 3D conceptual descriptive model, there is a drastic reduction in FZ interconnectivity. In the next subsection we will investigate the impact of this type of change in FZ interconnectivity in conjunction with other model dimensionality effects.

3.2.3.3.1 Fracture Zone Orientation

As illustrated in Figure 33, the FZs in our FNM fall into four sets: Vertical Set 1, which includes NE-SW FZs V9, V10 and V12; Vertical Set 2, which includes NW-SE FZs V16, V17, V13, V11, V15, V14, V18, V19 and V8; Low and Intermediate Dip (LID) Set 1, which includes the north-dipping H1, H2a, H3 and H7; and LID Set 2, which includes the south-dipping H5, H2b, and H6. The presence of these FZ sets in the MOTIF model was a direct result of the FNM simplification approach detailed in the Task E case definition as mentioned in Section 2.2. From the box-whisker summary statistics plot of Darcy flux magnitude (Figure 34) obtained from Simulation Run R_THMC for the four FZ sets at 109.3 kyr (near the end of meltwater production), there appears to be only minor differences between the FZ orientation sets. For the south-dipping LID set 2, mean Darcy velocity magnitude is twice that in the other sets. The dip direction of this set tends to parallel the direction of the topographic gradient, which may have contributed to the slightly higher velocities. A reason for the general similarity in Darcy velocities may be that many of the FZs are connected across orientation sets and all of them are well connected through the top two RM units, where the permeabilities lie within approximately an order of

magnitude of uniform FZ value. Although only summary statistics are shown here, individual Darcy velocities (or groundwater velocities) are available numerically and can be utilized to derive probability distribution functions for integrated system safety assessment.

3.2.3.3.2 Fracture Zone Interconnectivity

Inspection of the FNM in Figure 33 using 3D visualization techniques with Gocad[TM] and Raider3D[TM] indicated that the FZs could be grouped into three sets according to their interconnectivity: Connected Set 1 consisting of H1, H2a, H2b, H5, V11, V12, V13, V15, V16, and V17; Connected Set 2 consisting of H6, V8, V9, and V19; and unconnected FZs H3, H7, V10, V14 and V18. From Figure 35, which depicts the arithmetic mean and standard deviation of $|\mathbf{q}|$ from the R_THMC Simulation, the influence of FZ interconnectivity in this 3D model is apparently small, possibly for the same reason as that stated in the preceding sub-section.

The impact of FZ interconnectivity can also be studied by comparing Darcy velocities predicted by a 3D model with a corresponding 2D model. In the next subsection we will investigate the impact of this drastic change in FZ interconnectivity along with other model dimensionality effects.

3.2.3.4 Impact of Model Dimensionality

Figure 36 depicts the temporal evolution of equivalent freshwater head from the 2D Slice 2 THM model at the 13 locations illustrated in Figure 37. These points are located at various depths below surface in the RM (Points 1-4) and in FZs (Points 5-13). Comparison with 3D R_THMC head results in Figure 20 shows that model dimensionality has very little effect on head values or their temporal variation. The only noticeable differences appear to be the higher heads at depth in the R_THMC model in Figure 20 due to the higher density of saline water.

The situation is very different when it comes to Darcy flux and meltwater penetration. In Figure 38 we compare the mean and standard deviation of $|\mathbf{q}|$ in FZs from the 2D Simulation Run Slice 2 THM and its 3D equivalent Run S_THM. Simulation results plotted in these figures for the 3D run have been taken from elements that are intersected by the Slice 2 plane. Mean $|\mathbf{q}|$ from the 3D run is larger than corresponding values from the 2D run practically at all locations and times (although results are shown only at one time). This is especially true below modern mean sea level (approximately 350m below surface), where the RM permeability is 4.64×10^{-18} m^2, decreasing even further with depth below surface. At these depths the RM permeability is lower than that in the FZs by over four orders of magnitude and the RM effectively isolates any FZ that is not directly connected to another FZ. Evidently, from Figure 37 there are no interconnected FZs in the 2D model below a few hundred-metre depth. Furthermore, since in a 2D model groundwater movement is confined to the model plane, $|\mathbf{q}|$ values are much lower (by two orders of magnitude or more) than those in a comparable 3D model.

The effects of model dimensionality (and thereby FZ interconnectivity) also show up in our conservative estimate of glacial meltwater recharge using advective/convective particle tracking. Figure 39 displays the paths traced out by 134 water-coincident particles released at ground surface into the flow field predicted by the Slice 2 THM simulation. Evidently, all these paths remain in the shallow portion of the subsurface. The normalized histograms of maximum meltwater particle penetration for Simulation Runs 3D S_THM and 2D THM in Figure 40 indicate that the 2D model predicted much shallower recharge. Whereas in the 2D model all

glacial meltwater particles would not recharge deeper than 100m below surface, in the 3D model due to the presence of a much better connected FZ network, this percentage would be reduced to 50%. Furthermore, in the 3D model 22% of the meltwater particles would recharge deeper than 500m below ground surface.

3.2.3.5 Impact of Glacial Topography

From a detailed comparison of head values predicted by the R_THM and S_THM simulations, it was found that the primary effect of a gentler, smoother glacial topography is to slightly reduce and smooth out the horizontal hydraulic gradient (Figure 41 a and b). Although not easily recognizable by a casual comparison of Figure 41a to Figure 41b, numerical values indicate that the horizontal hydraulic gradient at LGM (97 kyr) from S_THM (Figure 41b) is approximately half that from R_THMC (Figure 41a). Interestingly, the resulting smaller horizontal groundwater velocities do not lead to shallower recharge of glacial meltwater particles. On the contrary, the S_THM case actually predicted slightly deeper meltwater penetration, as is evident from a comparison of the 38 particle paths plotted in Figure 42a for R_THM and Figure 42b for S_THM. This somewhat paradoxical result is partly due to the larger number of particle paths in the S_THM case going in an east to west direction, which caused more to intersect the long vertical N-S trending FZ at the western boundary, and partly due to the smaller horizontal flow velocities, which allows these particles to penetration deeper than those in the R_THM case. This is further confirmed by normalized histograms of maximum penetration depth depicted in Figure 43. The smoother and gentler glacial topography also leads to somewhat longer time for meltwater recharge to reach maximum depth below surface (Figure 44).

3.2.4   Impact of Glacial Scenario

Numerical modelling to investigate the impact of the glacial scenario by using an alternative (warm-based) scenario, University of Toronto's GSM Realization nn2778, was undertaken late in the work program. In order to expedite the work, a 2D modelling approach was adopted. As discussed in Subsection 3.2.3.5, the drawback of this approach is that Darcy flux and meltwater recharge predictions from 2D modelling are not representative of the response of the 3D subsurface Shield flow system. However, a comparison of 2D simulations using models that are identical in every aspect except for the glacial scenario may still, in a relative sense, shed some light on the impact of choice of glacial scenario on flow system dynamics.

Comparison of 2D THM simulation results using the cold-based scenario nn2008 and warm-based scenario nn2778 suggests that while the temporal evolution of hydraulic head for the two cases differ slightly in details (Figure 45) because of the different temporal variations of ice-sheet basal normal stress, temperature and meltwater flux (see Figures 13-15), the 134 particle paths (Figure 46 for the warm-based scenario compared with Figure 39 for the cold-based scenario) and frequency distributions of meltwater particle penetration depths (Figure 47) are very similar. Apparently, the longer period of (generally lower) meltwater infiltration flux (Figure 15) in the warm-based glacial scenario (GSM nn2778) in comparison with the cold-based scenario (GSM Realization nn2008) does not alter the flowpaths in the Task E Shield subregion flow domain.

4. ANOMALOUS HYDRAULIC HEAD

4.1 THE ISSUE

In the literature an "anomalous" hydraulic head is usually defined as an equivalent freshwater head, which cannot be interpreted in terms of normal gravitational advective (i.e., topographically controlled) flow under steady-state conditions (Horseman et al. 1991). The anomalies in hydraulic head may provide insight into the groundwater flow system evolution and the distribution of physical flow system properties.

Anomalous heads occur worldwide in a variety of geologic settings (Neuzil 1986 and 2003). Three possible causes include: 1) long-term transient flow, 2) high salinity, and 3) osmotically driven flow. In the Canadian Shield setting for this Task E modelling study the first two causes are more relevant.

Stevenson et al. (1996) reported field data from deep boreholes drilled from surface or from underground workings at the WRA in eastern Manitoba showing anomalous equivalent freshwater head values ranging from a few tens of metres to 120m above ground surface elevation. They also observed anomalously low equivalent freshwater heads in one borehole. These anomalies occurred in borehole intervals that intersected large domains of very low permeability, sparsely fractured rock (SFR). It is currently believed that true anomalous heads in the SFR of the WRA are a result of past glaciations (Chan et al. 1998, Chan and Stanchell 2004), possibly in combination with high salinity (Ophori et al. 1996) in the SFR. Modelling results have indicated that either explanation for anomalously high heads may be valid. However, salinity variations could not account for anomalously low heads.

In the following section, Task E THM modelling (with/ without salinity) results are examined in an attempt to gain further insights into the mechanisms that contribute to anomalous heads. The assumption is that if the glacial effects being modelled and the flow system properties are appropriate, these simulations should duplicate anomalous head observed at present day.

4.2 MODELLING RESULTS AND DISCUSSIONS

In accordance with hydrogeologic literature, anomalous head (h_{an}) in this report is defined as follows:

$$h_{an} = h_{mod} - h_{ss} \qquad\qquad\qquad (11)$$

where

h_{mod} is the present-day equivalent freshwater head predicted by one of the Task E models, and

h_{ss} is the nonglacial, topographically driven steady-state freshwater head.

In Figure 48 we have plotted the spatial distribution of anomalous head based on the 3D R_HM model at t = 121 kyr (approximately 11,000 years after the ice sheet has disappeared from the model subregion, i.e. present day). Evidently, this simulation predicted hardly any anomalous head (<2m equivalent freshwater head over most of the model domain). This is consistent with

the expectations of the instantaneous poroelastic effect due to mechanical loading/unloading by the ice sheet, but is at variance with both previous DECOVALEX III BMT3 glaciation-modelling results (Chan and Stanchell 2005) and field observations (Stevenson et al. 1996) at the WRA. In the BMT3 numerical study, residual anomalous head was predicted to be tens of metres to 250m, which is in qualitative agreement with the field data reported by Stevenson et al. and cited in Subsection 4.1. Three possible reasons for the absence of anomalous head in the Base Case simulations may be postulated:

1. In the base-case (cold-based) glacial scenario (GSM Realization nn2008) simulated, because of the hydraulic boundary conditions imposed, the consolidation effects of mechanical ice loading cause most of the changes in subsurface hydraulic head. In the poroelastic formulation imbedded in MOTIF, the pore-space compression and the concomitant fluid pressure increase upon glacial loading, as well as elastic recovery of pore volume upon glacial unloading, are instantaneous.

2. Transient recovery of hydraulic head to the interglacial value after ice-sheet unloading is dependent on the permeability and porosity distribution in the model. The Base Case permeability of the rock mass at depth may not be sufficiently low resulting in any glacially induced excess pore pressure to dissipate shortly after glacial retreat from the modelled subregion.

3. The well-connected fracture zone network in the present study allows the excess pore pressure to dissipate rapidly after deglaciation.

4.2.1 Generic Studies

Generic sensitivity analyses have been conducted to test the first two hypotheses. In the first additional run (Generic Case 1 or GC1) the rock and FZs were assumed to have the same physical properties as in DECOVALEX III BMT3, for which the rock mass permeabilities at depth were 1-2 orders of magnitude lower than in the Task E Base Case. The glacial scenario was the Base Case (BC) Scenario (GSM Realization nn2008) described in Subsection 2.4. In the second additional run (Generic Case 2 or GC2) the physical properties were identical to the BC, but a generic wet-based glacier (Boulton glacier for the purpose of this report) was assumed for all three glacial cycles, whereby a prescribed hydraulic head corresponding to a spatially variable basal water pressure equal to 80% of the basal normal stress from Peltier's (private communication 2004, 2006) GSM Realization nn2008 was assumed at the ice-sheet base/land surface boundary. This basal water pressure distribution mimics the hydraulic boundary conditions that Prof. G.S. Boulton of the University of Edinburgh (see Boulton et al. 2004 and Chan et al. 2005) extracted from his team's ice-sheet/drainage model to provide to the DECOVALEX III BMT3 subsurface modelling teams. This prescribed hydraulic head boundary condition, which could reach values >2000 m over an extended duration (>10 000 years) around the LGM, was in sharp contrast with the prescribed flux boundary condition for the BC (see Section 2), which had a zero value to represent a cold-based glacier, except for the 2 000-year, meltwater production stage with a flux of ≤10 cm/a toward the end of the scenario.

Figure 49 summarizes the vertical profiles of equivalent freshwater head predicted by 3D HM simulations for the three sensitivity study cases. In this figure the three sets of curves represent the BC, GC1 (cold-based BC glacial scenario with BMT3 hydraulic and mechanical properties) and GC2 (BC hydraulic and mechanical properties with BMT3 Boulton-type glacier after Boulton et al. 2004). Evidently, at 600 years after glacial retreat from the study site (at

110, 200 years in model time) there is practically no residual elevated head according to the BC simulation, a maximum of 20-30 m residual elevated head at an elevation of -400 masl (~750m below surface) according to the GC1 simulation, and up to 300 m residual elevated head at an elevation near -1200 masl (~1550m below surface) according to the GC2 simulation. Numerical results indicate that only the GC2 simulation predicts any elevated head to persist for a few thousand years. This is illustrated further in Figure 50, where vertical head profiles at the model origin from the GC2 simulation are plotted at various times following glacial retreat from the site. The model predicts present-day (at 121,000 years in the model time scale) residual anomalously high heads to exist at depths greater than 725m below surface, having values increasing with depth to 30-40 m near the bottom (1600-m below surface) of the model domain. These anomalous head values are smaller than those observed at WRA. It appears that both a temperate (wet-based[8]) glacier and very low rock mass permeability ($\leq10^{-20}$ m^2) may be required to yield anomalous heads comparable to those observed at the WRA. Further sensitivity analysis has been undertaken using the warm-based glacial scenario GSM Realization nn2778 (see below).

4.2.2 Model Dimensionality

To address Reason 3 listed above with regard to the influence of the interconnected FZ network, we examine the spatial distribution of anomalous head depicted in Figure 51 for the 2-dimensional (2D) Slice 2 HM model. Clearly, the absence of an interconnected FZ network, together with the inability to dissipate excess pressure in the third dimension, has yielded localized anomalous (high and low) heads ranging from –15m to +15m. During ice-sheet retreat the basal normal stress load is distinctively higher on the right-hand side of the model domain than on the left (see basal normal stress distribution at 11.2 ka BP in Figure 16). This uneven load would cause flexure in the elastic rock mass. Consequently, pore space on the left-hand side of the model would tend to rebound leading to reduced pore pressure, i.e., negative anomalous head, whereas on the right-hand side, the downward flexure would lead to pore space compression resulting in excess pore pressure, i.e., positive anomalous head. As there is limited FZ interconnectivity and rock mass permeability is generally low, the system has not yet recovered hydraulically about 11, 000 years after the ice sheet has retreated off the modelled subregion. It can also be observed in Figure 51 that the absolute value of the anomalous head generally tends to be higher in areas far away from long FZs and from side boundaries than near them. In addition, the impact of adding thermal processes in the 2D simulations was minimal as indicated by the similarity between the anomalous head distributions shown in Figure 51 (HM model) and Figure 52 (THM model).

4.2.3 Salinity Effect

Figure 53 shows the density effects of saline water on anomalous head distribution from the 2D THMC (salinity) coupling. By comparing Figures 52 and 53, one can infer that for the Task E case study, salinity has a major influence on the predicted anomalous head distribution. The high (up to 90-m equivalent freshwater head), stratified anomalous head at depths of more than 750m below surface are associated closely with the lowest permeability unit where saline groundwater with density 1.10 kg/L was assumed in the simulation. Thus this coupled THMC model does predict substantial anomalous head, which is partly due to the density effect of

---

[8] With sufficient meltwater production to justify prescribed head boundary conditions at ground surface.

salinity and partly due to residual coupled THM effect from the last glacial event. Furthermore, all the simulation results depicted in Figures 51 to 53 exhibit both positive and negative anomalous heads, in qualitative agreement with what was reported for the WRA (Stevenson et al. 1996).

One may be tempted to infer from the anomalous head distribution depicted in Figure 53 that the hydraulic gradient would imply substantial upward flow velocity. However, as explained in Subsection 3.2.1, most of the increase in equivalent freshwater head simply represents the depth-dependent hydrostatic head from a column of saline water. Perhaps in a saline groundwater environment, the concept of anomalous head defined by Equation (11), is not the best measure to delineate residual excess pressure from a previous glacial event. The pressure p predicted by a THM model with depth-dependent salinity has already taken into account the variable density of water due to variable temperature and salinity. Corresponding to this, rather than using the hydrostatic pressure at a subsurface location due to the weight of the freshwater column above as the reference, we should be using the saline hydrostatic pressure p_{sh} calculated from the total weight of the variable-density water column above it, thus

$$p_{sh} = \int_0^{\Delta z} \rho_s(z) g \, dz \, , \qquad (12)$$

where ρ_s is the saline groundwater density, z is the elevation (masl) of the subsurface location and Δz is the depth of this location below ground surface. In site characterization, there is seldom enough density measurement to facilitate the calculation in Equation (12). In a numerical model, however, this information is available and, perhaps, the excess pressure (p - p_{sh}) is a better measure of residual effects from past glaciation.

4.2.4 Alternative Glaciation Scenario

To investigate the impact of an alternative glaciation scenario, a 2D THM simulation was undertaken using the warm-based GSM Realization nn2778. The anomalous head contours resulting from this simulation are plotted in Figure 54. The distribution is quite similar to that depicted in Figure 52 for the cold-based model, although there are some fine-structure differences due to the somewhat different spatial and temporal distributions of ice sheet basal normal stress between the two scenarios. The longer meltwater production duration, but lower rate, of the warm-based scenario compared to the cold based one did not contribute to significantly greater anomalous heads in the 2D model.

4.2.5 Summary

Simulation results for anomalous head can be summarized as follows:

- The 3D R_HM simulation based on the Task E conceptual model predicted hardly any anomalous head (<2m equivalent freshwater head over most of the model domain) at t = 121 kyr (approximately 11,000 years after the ice sheet has disappeared from the model subregion.

- From a generic sensitivity analysis it appears that both a temperate (wet-based) glacier and very low rock mass permeability ($\leq 10^{-20}$ m^2) may be required to yield anomalous heads comparable to those observed at the WRA.
- Effectively truncating most of the FZ interconnectivity by means of 2D modelling yielded small anomalous heads in the range –15m to +15m. Thermal effects have little impact while density effects from salinity significantly increase the predicted anomalous head, with a maximum value reaching 90m at depths 1,400m or greater below surface. In this case, most of the anomalous head reflects just the hydrostatic head in saline groundwater, which would not drive flow.
- Simulations using the two glacial scenarios nn2008 and nn2778 resulted in very similar anomalous head distributions.

5. STATE OF STRESS

5.1 THE ISSUE

According to the two GSM realizations used in this study, during the last glacial event mechanical loading by the Laurentide ice sheet can impose large normal stress on the surface of the Task E Shield flow domain, which can reach 25-30 MPa (Figures 13 and 14). It is therefore important to investigate how glaciation affects the stability of the sparely fractured rock mass (SFR) and the fracture zones, which in turn can impact the safety of a DGR. Repository designers may also want to know whether it would be necessary for them to take into account any significant rotation of principal effective stresses that accompanies a glacial event. In the BMT3 case study, for example, it was found that the SFR would become more stable when a thick ice sheet covers the flow domain under study. Fracture zones might have enhanced or diminished stability depending on orientation. However, it was predicted that for the model parameters and glaciation scenario utilized in BMT3 the few simulated fracture zones would not fail at depths greater than 100m below surface.

The state of stress and stability predicted in a THM model are expected to be quite sensitive to the distribution of mechanical and, to a lesser extent, hydraulic properties, FNM geometry, as well as the prevailing present day in situ state of stress. Therefore, Task E modelling activities included an examination of stress and stability changes on the sub-regional domain geosphere subjected to the same GSM glaciation scenarios discussed in previous sections.

5.2 MODELLING RESULTS AND DISCUSSIONS

Numerical results indicate that the predicted displacements and stresses are practically independent of salinity and the details of ice-sheet topography. Therefore, the impact of these two modelling alternatives will not be discussed in the following sections.

5.2.1 Displacement

Figure 55 depicts the temporal evolution of vertical mechanical and thermomechanical displacement from the R_THMC simulation for the 12 selected points located in rock mass and fracture zones as listed in Table 5. It should be noted that displacement was calculated relative

to the bottom of the model and therefore are not representative of values that would be generated from a crustal scale model that would include mantle viscosity (Peltier 2002). The evolution of downward displacement with time follows primarily the time varying ice-sheet normal loading/unloading at the top boundary, with some delay due to transient consolidation effects. Maximum downward displacement occurring at LGM is approximately 0.7 m. Horizontal displacements are much smaller. Some of the curves do illustrate more downward displacement at points in fracture zones, which are more compliant, than in the rock mass at comparable elevations. For example, there is more downward displacement at Point 6 at almost 100 m below surface in a fracture zone than at Point 8 on the surface in the rock mass. The thermal mechanical coupling effect (thermal expansion/contraction) is evident in the temporal variation of displacement during periods when no ice sheet overlies the flow domain, but when surface temperatures steadily decrease (Figure 13).

5.2.2 Effective Stress and Thermomechanical Stability/Failure Analysis

Temporal evolution of the maximum, intermediate and minimum, principal, effective stresses from the R_THMC simulation is shown in Figures 56 to 58, respectively. During glaciation both thermal stress and glacial mechanical loading contribute to change the effective state of stress. In addition, pore pressure changes due to thermal expansion/contraction of pore water and hydraulic-mechanical coupling produce a counterbalancing effect so that the net change in effective stress is less than the algebraic sum of the thermomechanical and mechanical components. Changes in the maximum (σ'_1 in Figure 56) and minimum (σ'_3 in Figure 58) effective stresses are less pronounced than changes in the intermediate effective stress (σ'_2 in Figure 57). During glaciation the effective stress in a FZ, e.g., at Point 1, is significantly lower than at nearby Points 2 and 3 in rock mass due to stress redistribution around the less stiff FZs. The change in vertical normal effective stress resulting from mechanical ice loading is much higher than changes in the horizontal components, such that σ'_2, which was initially horizontal and oriented north - south, becomes vertical during the glacial loading/unloading cycles (see below). Consequently, the ratios $\sigma'_1 : \sigma'_2$ and $\sigma'_1 : \sigma'_3$ become smaller during glaciation and the rock mass becomes more stable.

The thermomechanical contribution to the change in state of stress is illustrated by comparison of σ'_1 in Figure 56 for the R_THMC model with Figure 59a for the R_HM model, as well as by plotting, in Figure 59b, the differences in maximum effective principal stresses between the R_THMC and R_HM cases for selected points in the RM. The thermomechanical contribution was found to be both depth and time dependent as temperatures vary with depth and time.

Several locations in the model domain were selected to investigate stress rotation and illustrate stability/failure analysis. These locations are shown in Figure 60 and include S1 and S2 in the rock mass (RM), S3 and S4 in subvertical FZs at 670m below surface and S5 in a LID at a shallower depth. Figure 61 depicts the temporal evolution of the angle between σ'_2 and the horizontal y-axis at locations S1 and S2. Evidently, the intermediate principal effective stress rotates between the horizontal orientation and a nearly vertical orientation in phase with the three glacial loading/unloading cycles. Consequently, an underground repository design that has been optimized with respect to contemporary stress orientations could potentially no longer be optimized during a future glacial event similar to scenario GSM Realization nn2008.

In Figure 62, σ'_1 at locations S1 and S2 in RM from the R_THM model is plotted as a function of σ'_3 at four stages during the third ice sheet advance/retreat cycle: at a nonglacial stage

(75 kyr), at glacial advance (90.8 kyr), at LGM (98 kyr) and near the end of glacial retreat (109.5 kyr). The Hoek-Brown failure envelope is also plotted for comparison. It can be seen that the RM has a large factor of safety during the glacial cycle. Although both σ'_1 and σ'_3 increase as the ice-sheet cover thickens, the failure envelope has a steeper gradient and therefore RM stability is actually enhanced.

The situation is quite different in FZs. As is evident from Figure 63, given the assumed, nonglacial, contemporary far-field in situ state of stress and assumed mechanical, thermomechanical and thermoelastic properties, subvertical FZs were shown to be in a failure condition even prior to a glacial event. The glacial event contributed to a worsening of the failure condition. Failure potential in the fracture zones requires further analysis. For proper evaluation of the stability (or failure) of the FZs, their possible failure under the contemporary, nonglacial far-field in situ stress should be analyzed first. The failure of a fracture zone would lead to stress relief within it and accompanying stress redistribution in the nearby rock mass. This type of failure would have occurred in the distant past in the course of the tectonic history of the study site. Glaciation occurred long afterwards and, therefore, in our failure analysis the glacially induced stress changes should be superimposed on the relaxed state of stress in the model domain for this study, rather than on the contemporary far-field in situ stress, which is applicable to the RM only. A simpler, though less rigorous, approach may be to repeat the type of stability/failure analysis exemplified in Figures 62 and 63 using a nonglacial far-field in situ stress that corresponds to the lower end of the confidence interval in the statistical compilation by Kaiser and Maloney (2005).

The factor of safety, as evaluated according to the Hoek-Brown failure criterion, is plotted at the glacial advance phase in Figure 64a, at LGM in Figure 64b and at the glacial retreat phase in Figure 64c. The factor of safety is highest at LGM, with a value close to 10 in the RM away from the FZs. It is lower during glacial advance and, especially, during glacial retreat. Nevertheless, a factor of safety >2 is still available in the RM at all times.

A cursory investigation of the impact of choice of glacial scenario on thermomechanical stability/failure was conducted based on the results of 2D THM simulations using the cold-based scenario GSM Realization nn2008 and the warm-based scenario GSM Realization nn2778. Effective state of stress calculated for Points 1-4 in RM as illustrated in Figure 65 and for Point 1 in a subvertical FZ, as illustrated in Figure 66, were utilized for the stability/failure analysis. As shown in Figure 67 for the cold-based glacial scenario and Figure 68 for the warm-based scenario, the RM is more stable during glaciation, with large factors of safety similar to the 3D simulation results in both cases. In contrast to the 3D analysis (presented in Figure 63), Point 1 in a subvertical FZ is stable during glaciation in either glacial scenario (Figures 69 and 70 for the cold-based and warm-based glacial scenarios, respectively). One conclusion from this brief analysis is that 2D THM simulations in a fractured rock mass may over-estimate the stability of FZs. In the 3D THM model the subvertical FZs were allowed to undergo strike-slip failure, which is not possible in the 2D model due to constraints in the out-of-plane direction. Another conclusion is that the glacial scenario (within the limitation of the two scenarios considered) has very little impact on the effective state of stress and thermomechanical stability.

6. GROUNDWATER FLOW DYNAMICS UNDER PERMAFROST CONDITIONS

The GSM glaciation scenarios used for the Task E simulations predicted time-dependent depths for permafrost penetration, assumed to be represented by the zero-degree isotherm. MOTIF simulation results discussed in the previous sections did not incorporate a change in material properties to represent the time-dependent thickness of permafrost. Representing permafrost in the Task E simulations, although desirable from the point of view of studying flow system dynamics during a glacial cycle, presented several challenges. Firstly, there is a dearth of information regarding the physics of permafrost in rock. Therefore, as a first approximation, permafrost was represented as a very low-permeability rock mass having the same permeability (1.55×10^{-19} m^2) as the lowest rock unit in the Task E subregional Shield flow system but with unchanged mechanical parameters. To simulate the formation and temporal evolution of permafrost, a special coupled THM analysis was performed by incorporating an algorithm into MOTIF to assign the permeability of the RM or FZ elements according to the values listed in Table 1 or to the assumed permafrost value depending on whether the temperature at a particular time step is above or below the pressure adjusted freshwater freezing point. Secondly, the moving permafrost front introduced severe numerical challenges into MOTIF THM modelling, which could not been overcome during the course of this study. As a result of these numerical challenges, the impact of permafrost was only investigated through a very limited, simplistic approach described in the next subsection.

6.1 HIGHLY SIMPLIFIED REPRESENTATION OF PERMAFROST CONDITIONS

Based on a MOTIF THM simulation of the temporal evolution of the pressure-adjusted zero-degree C isotherm (Figure 71), which agrees with thermal modelling results reported by Peltier (2004), permafrost penetration varies with time, with a maximum depth of approximately 400m below surface. In the simplified approach reported in this section, a constant, time-invariant permafrost layer with a uniform thickness of 350 metres was incorporated into a 2D HMC model. This permafrost thickness spans the first four permeability units from the top of the domain (Figure 72). This model was designated as 2D HMC_P350 (Table 4). It should be noted that according to MOTIF THM simulations the bottom of the permafrost is not flat, but is a subdued replica of ground topography (Figure 73). However, for the purpose of this limited study, a flat permafrost bottom was considered a reasonable representation.

The top, the bottom and the sides of the model, from the top to 350m below surface, were assumed to be no-flow boundaries, while prescribed hydraulic heads were assigned to the remainder of the side boundaries based on the time-dependent HM equilibrium approach described in Subsection 2.6.3.

6.2 MODELLING RESULTS AND DISCUSSIONS

Comparison of the temporal evolution of hydraulic head at the 13 selected points (Figure 37) from 2D HMC modelling without (Figure 74a) and with a 350-m thick permafrost (Figure 74b) reveals only minor differences. This is not surprising, considering that the hydraulic head is caused solely by coupled HM effects due to glacial mechanical loading/unloading. However, the presence of constant permafrost alters the Darcy flux field dramatically, as illustrated by comparison of the vertical profiles of Darcy flux magnitude from 2D HMC modelling in Figure 75a and from the 2D HMC_P350 modelling in Figure 75b. Darcy flux magnitudes in the low-

permeability permafrost generally fall in the $10^{-7} - 10^{-6}$ m/a range, similar to values in the lowest RM unit. Between the permafrost and the lowest RM unit (0 to –375 masl), permeabilities are higher and Darcy flux magnitudes are higher, ranging between $10^{-6} - 10^{-5}$ m/a. In Figure 76 we compare the mean and standard deviation of Darcy flux magnitudes in progressively deeper model layers at LGM (98 kyr) predicted by the 2D HMC (black) and 2D HMC_P350 models (red). This confirms the information in Figure 75b that the mean Darcy flux magnitude is low in the permafrost. However, the mean value in the unfrozen Unit 5 is about a factor of four higher in HMC_P350 than in HMC. Given the vertical hydraulic boundary conditions of the 2D model, coupled with the very little flux transmitted through the permafrost, the modelled flow system compensates by passing more flux through the comparatively more permeable Unit 5.

Simulations were also performed for 70-m thick and 150-m thick permafrost, which, as expected, produced relatively higher Darcy flux magnitudes in the layers immediately below the respective permafrost layer.

Simulation HMC_P350 was repeated using the warm-based glacial scenario GSM nn2778, with little difference in results. This is not surprising since the largest difference between the two glacial scenario realizations is the length of the meltwater production period and the magnitude of meltwater production, which occurs concurrently with the absence of permafrost.

7. SUMMARY, CONCLUSIONS AND CHALLENGES

7.1   SUMMARY

This report documents numerical modelling activities that have been undertaken as Task E of the international DECOVALEX THMC (Thermal-Hydraulic-Mechanical-Chemical processes) project to address the implications of Long-term Climate Change, particularly glaciation, on groundwater flow system dynamics as it could affect Deep Geologic Repository (DGR) performance. Systematic, 2-dimensional and 3-dimensional THM simulations with varying degrees of coupling, including depth dependent salinity (represented as a change in groundwater density) and temperature dependent density and viscosity, were undertaken using the MOTIF finite-element code. The modelling domain for the THM simulations consisted of an hypothetical, 1.6-km deep, sub-regional scale ($\approx$100 km^2) fractured Shield flow system and transient boundary conditions were developed from two realizations (nn2008 with a cold-based glacier and nn2778 with a warm-based glacier) of the University of Toronto Glacial Systems Model (GSM) of the last North American continental glaciation.

DGR performance related issues addressed by this Task E case study include the infiltration of glacial meltwaters to the subsurface, anomalous hydraulic head and evolution of the effective state of stress during a glacial event. The impact of various model parameters were also investigated including the degree of coupling of THMC (salinity) processes, the surface boundary conditions (ice-sheet topography), model dimensionality, and two alternative glacial scenarios. In addition, a limited numerical study was conducted to simulate groundwater flow dynamics under permafrost conditions.

7.2   CONCLUSIONS

Key findings related to DGR performance were:

- During glaciation, the evolution of equivalent freshwater head (hereafter referred to as "head") in the Shield subregional flow system follows the advance/growth and retreat/decay of the ice sheet. For this particular conceptual model, the flow domain appears to have little memory of previous glacial cycles, with respect to carryover of significant thermal and hydraulic effects.

- Coupled 3D HM or THM simulations predicted practically no anomalous head in contrast to the results of BMT3. However, sensitivity analyses suggest that a combination of a "wet-based" glacier, very low rock mass (RM) permeability ($\sim 10^{-20}$ m^2) and limited fracture zone (FZ) interconnectivity appears to be the necessary condition for residual glacially induced anomalous head.

- The increase of hydraulic head under ice loading is not equal to the total stress imposed by the glacier. Consolidation effects increase the head by about 1/3 of the normal stress that the ice sheet imposes on the bedrock, in part due to the ratio between the compressibilities of the rock and the water.

- The incremental head values resulting from ice loading and HM coupling are relatively uniform throughout the modelled subregion both horizontally and vertically. This is in contrast to what would occur if one used a hydraulic head boundary condition equivalent to the ice-sheet thickness in an uncoupled flow model.

- Head values in Fracture Zones differ from those in the adjacent Rock Mass by a few metres.

- During the short-lived glacial advance and retreat stages, the horizontal hydraulic gradient is steeper than the nonglacial topographically driven hydraulic gradient (approximately 0.003) by up to a factor of two, while near the Last Glacial Maximum (approximately 20, 000 years ago) the hydraulic gradient is slightly less than the nonglacial value. These differences resulted from imposing non-uniform glacial stresses across the surface of the domain to better represent passage of the glacier terminus. Throughout the glacial cycle the vertical head gradient is generally less than 0.05 from surface to approximately 725m below. Below this level, saline groundwater with an assumed density of 1.10 kg/L gives rise to an equivalent freshwater vertical head gradient of approximately 0.1.

- During the glacial cycle, the Darcy flux magnitudes (absolute values) fall into two groups: (i) values on the order of 10^{-2} to 10^{-1} m/a in the FZs at various elevations and in the highly permeable RM near surface, and (ii) values between 10^{-7} to 10^{-5} m/a in the RM at depths 350 m or more below ground surface. These latter values are representative of diffusion-dominated transport environments. It is important to note that in the conceptual model, FZ permeability was assumed to be constant with depth. Assigning lower FZ permeabilities with depth would have resulted in lower flux magnitudes.

- Within the context of the Task E conceptual model, FZ sets with different orientations or belonging to different interconnectivity groupings exhibited relatively consistent groundwater velocities. This finding likely resulted from the uniform FZ permeability and from the good FZ connectivity provided by the high-permeability, upper rock mass layers. Through using 2D simulations and thereby removing most of the FZ interconnectivity, groundwater velocities in the FZs were reduced by a factor of 100. Consequently, the approach to representing FZ connectivity in a conceptual model will play an important role in the resulting simulated velocities and should be carefully considered while acknowledging site characterization uncertainties.

- Based on water-coincident particle-tracking analysis associated with meltwater production periods from the GSM realizations, approximately 72% of glacial meltwater particles did not recharge below the bottom of the shallow rock unit at 70m below surface and less than 6% penetrated to the 500-m level and beyond. The meltwater penetration depth might have been overestimated since simplifying the Fracture-zone Network Model has been shown to over-predict the groundwater velocities in FZs. Furthermore, particle tracking analysis alone does not account for diffusion, dispersion, sorption and chemical reactions along pathways that would further limit glacial meltwater penetration.

- Simulations using different coupling mechanisms and model parameters suggest that meltwater penetration depths are (i) slightly enhanced by thermal effects, (ii) slightly diminished by salinity (density) effects, (iii) slightly influenced by the glacial scenario (within the two scenarios simulated) and by the approach to representing ice sheet topography, but (iv) severely underestimated by using a 2D model. Ultimately, the nature of the flux-based, surface hydraulic boundary condition imposed on the model, as well as the assumed distribution of hydraulic parameters played a significant role on simulated meltwater penetration depths.

- Effectively truncating most of the FZ interconnectivity by means of 2D modelling yielded small anomalous heads in the range –15m to +15m. Thermal effects have little impact while density effects from salinity significantly increase the apparent anomalous head at depth. In this case, most of the anomalous head reflects just the hydrostatic head in saline groundwater. Simulations using the two glacial scenarios nn2008 and nn2778 resulted in very similar anomalous head distributions.

- During glacial coverage, the mechanical factor of safety increases in the RM, but principal effective stress reorientation also occurs. Given the assumed, nonglacial, in situ state of stress and assumed mechanical, thermomechanical and poroelastic properties, subvertical FZs were determined to be in a failure condition even prior to a glacial event. The glacial event contributed to a worsening of the failure condition. This finding indicates that the geomechanical input parameters assumed in the conceptual model would need to be carefully revised to allow for an appropriate prediction of subvertical FZ stability/failure during glaciation. Low-dip FZs, although stable under the assumed in-situ conditions, tended only to approach failure during glaciation. In this numerical study, salinity, glacial topography and the type of glacial scenario had little effect on the predicted effective state of stress. However, 2D modelling was found to drastically overestimate the stability of the FZs.

- A limited, 2D, numerical study was conducted on subregional Shield groundwater flow dynamics under permafrost conditions. A time-invariant, uniform, 350-m thick, low-permeability (~10^{-19} m^2) rock layer was used to represent the permafrost. Elevated hydraulic heads continued to be generated in the pseudo-permafrost layer during glacial loading since other material properties remained unchanged. Coupled HM simulation with salinity predicted low Darcy flux in the permafrost, but somewhat higher flux only in the RM unit immediately below the permafrost near LGM when compared to the no-permafrost condition.

7.3   COUPLED MODELLING CHALLENGES

A number of challenging issues pertaining to THM and THMC modelling of subsurface response to long-term climate change include:

- THM and THMC modelling of transient evolution of permafrost incorporating correct physics and of THM processes and THM properties associated with phase change.
- Influence of repository heat on permafrost evolution.
- Fully coupled THMC modelling, i.e., including spatially continuous variable salinity and saline water transport.
- Fracture or fracture zone reactivation (slip, dilation or failure) with these features and mechanisms explicitly modelled, not just by post-processing.
- Stress and depth-dependent fracture or fracture zone permeability in THM modeling.
- Question of side boundary conditions, i.e., large-scale THM modelling to obtain boundary conditions for the subregional scale model or more accurately imbedding the near-field sub-model in a far-field model.
- Coupling a THM model to a reactive transport model to investigate consistency with paleo-hydrogeochemical studies.
- Coupling of far-field THM or THMC modelling of glaciation to near-field modelling of impact on potential repository features such as he shafts, tunnels and disposal rooms.
- THMC simulations with site-specific lithostructural model without the DTHMC-type of fracture zone network simplification, requiring High Performance Computing facilities.

ACKNOWLEDGEMENTS

REFERENCES

Biot, M.A. 1941. General theory of three-dimensional consolidation. Journal of Applied Physics $\underline{12}$, 155-164.

Boulton G., T. Chan, R. Christiansson, L. Ericsson, J. Hartikainen, M.R. Jensen, F.W. Stanchell and T. Wallroth. 2004. Thermo-hydro-mechanical (T-H-M) impacts of glaciation and implications for deep geologic disposal of nuclear waste. In Geo-engineering Book Series, Vol. 2: Coupled thermo-hydro-mechanical-chemical processes in geo-systems. (Editors, O. Stephansson, J. A. Hudson and L. Jing). Amsterdam, Elsevier, p 299-304.

Bouteca, M. and Y. Gueguen. 1999. Mechanical properties of rocks: Pore pressure and scale effects. Oil & Gas Science and Technology – Rev.IFP, V$\underline{ol. 54, No. 6}$, 703-714.

Chan, T. and F.W. Stanchell. 2004. DECOVALEX III BMT3 (The Glaciation Bench Mark Test) Final Research Team Report. Prepared by Atomic Energy of Canada Limited for Ontario Power Generation. Ontario Power Generation, Nuclear Waste Management Division Report 06819-REP-01300-10091-R00. Toronto, Ontario.

Chan T and F.W. Stanchell. 2005. Subsurface hydro-mechanical (HM) impacts of glaciation: Sensitivity to transient analysis, HM coupling, fracture zone connectivity and model dimensionality. Int. J. Rock Mech. Min. Sci. $\underline{42}$, 828-849.

Chan, T. and F.W. Stanchell. 2006. Numerical Modelling of Subsurface Coupled THM Processes in a Sub-regional-Scale Groundwater Flow System in a Canadian Shield Setting During a Glacial Event: II. Coupled HM Modelling. In Proc. GeoProc 2006: Advances on Coupled Thermo-Hydro-Mechanical-Chemical Processes in Geosystems and Engineering. (Editors, W. Xu, X. Tan and S. Yang). Nanjing, China, May 22-25, 2006, p 485-490.

Chan T., P.A. O'Connor and F.W. Stanchell. 1998. Finite-element modelling of effects of past and future glaciation on the host rock of a used nuclear fuel waste vault. Ontario Hydro Nuclear Waste Management Division Report, 06819-REP-01200-0020 R00. Prepared by Atomic Energy of Canada Limited for Ontario Hydro (now Ontario Power Generation). Toronto, Ontario.

Chan, T., N.W. Scheier and V. Guvanasen. 1999. MOTIF Code Version 3.2 Theory Manual. Prepared by Atomic Energy of Canada Limited for Ontario Hydro. Ontario Hydro Nuclear Waste Management Division Report 06819-REP-01200-0091-R00, Toronto.

Chan T, R. Christiansson, G.S. Boulton, L.O. Ericsson, J. Hartikainen, M.R. Jensen, D. Mas Ivars, F.W. Stanchell, P. Vistrand and T. Wallroth. 2005. DECOVALEX III BMT3/ BENCHPAR WP4: The thermo-hydro-mechanical responses to a glacial cycle and their potential Implications for deep geological disposal of nuclear fuel waste in a fractured crystalline rock mass. Int. J. Rock Mech. Min. Sci. $\underline{42}$, 805-827.

Chan, T., M.R. Jensen, F.W. Stanchell and A. Vorauer. 2006. Numerical modelling of subsurface coupled THM processes in a sub-regional-scale groundwater flow system in a

Canadian Shield setting during a glacial event: I. Conceptual Model Development. In Proc. GeoProc 2006: Advances on Coupled Thermo-Hydro-Mechanical-Chemical Processes in Geosystems and Engineering, (Editors, W. Xu, X. Tan and S. Yang). Nanjing, China, May 22-25, 2006, p 155-164.

DeMarsily, G. 1986. Quantitative Hydrogeology. Academic Press.

Frape, S.K., R.L. Stotler, T. Ruskeeniemi, L. Ahonen, M. Paananen and M.Y. Hobbs. 2004. Hydrogeochemistry of groundwaters at and below the base of the permafrost at Lupin: Report of Phase II. Ontario Power Generation Nuclear Waste Management Division Report 06819-REP-01300-10047-R00. Toronto, Canada.

Gascoyne, M., J. McMurry and R. Ejeckam. 2004. Paleohydrogeologic case study of the Whiteshell Research Area. Ontario Power Generation, Nuclear Waste Management Division Report 06819-REP-01200-10121-R00, Toronto, Ontario.

Guvanasen, V. and T. Chan. 2000. A three-dimensional numerical model for thermo-hydromechanical deformation with hysteresis in a fractured rock mass. International Journal of Rock Mechanics and Mining Sciences 37, 89-106.

Hoek, E. and E.T. Brown. 1988. The Hoek-Brown Failure Criterion-a 1988 Update. In Rock Engineering for Underground Excavations, (Editor, J.C. Curran). In Proceedings of the 15th Canadian Rock Mechanics Symposium, Toronto, Canada, p. 31-8.

Horseman, S.T., J. Alexander and D.C. Holmes. 1991. Implications of long-term transient flow, coupled flow and borehole effects on hydrogeological testing in opalinus clay: Preliminary study with scoping calculations. NAGRA Report, NAGRA-NTB-91-16, Wettingen, Switzerland.

Jaeger, J.C. and N.G.W. Cook. 1976. Fundamentals of Rock Mechanics, 2nd Edition. Halsted Press, New York, NY.

Kaiser, P. K. 2004. In-situ stress state for DECOVALEX modelling. MIRARCO letter to OPG, Ontario Power Generation, Nuclear Waste Management Division Correspondence, 06819-CORR-03787.2-0117357, Nov. 7, 2004.

Kaiser, P.K. and S. Maloney. 2005. Review of ground stress database for the Canadian Shield. Prepared by MIRARCO Mining Innovation. Ontario Power Generation, Nuclear Waste Management Division Report 06819-REP-01300-10107-R00.

Nakka, B.W. and T. Chan. 1994. A particle-tracking code (TRACK3D) for convective solute transport modelling in the geosphere: Description and User's Manual. Atomic Energy of Canada Limited Report AECL-10881, COG-93-216.

Neuzil, C.E. 1986. Groundwater flow in low-permeability environments. Water Resour. Res., 22(8), 1163-1195.

Neuzil, C.E., 2003, Hydromechanical coupling in geologic processes: Hydrogeology Journal, 11 (1), 41-83

Nguyen, T. S. 2004. Influence of near field coupled THM phenomena on the performance of a spent fuel repository: Task A-1 (DECOVALEX THMC) – Preliminary scoping calculations Rev. 1, April 2004. Available at www.decovalex.com

OPG-Specs. 2004. Appendix A of Nguyen (2004). Technical specification from OPG recommended for Horizontal Borehole Concept for DECOVALEX-THMC model, Rev. 0a, 15 April 2004.

Ophori, D.U., D.R. Stevenson, M. Gascoyne, A. Brown, C.C. Davison, T. Chan and F.W. Stanchell. 1996. Revised model of regional groundwater flow of the Whiteshell Research Area. Atomic Energy of Canada Limited Report, AECL-11435, COG-95-443.

Peltier, W.R. 2002 A design basis glacier scenario. Ontario Power Generation, Nuclear Waste Management Division Report 06819-REP-01200-10069-R00. Toronto, Ontario.

Peltier, W.R. 2003. Long-term climate change – glaciation. Ontario Power Generation, Nuclear Waste Management Division Report 06819-REP-01200-10113-R00. Toronto, Ontario.

Peltier, W.R. 2004. Permafrost influences upon the subsurface. Ontario Power Generation, Nuclear Waste Management Division Report 06819-REP-01200-10134-R00, Toronto, Ontario.

Peltier, W.R. 2006. Boundary conditions data sets for spent fuel repository performance assessment. Ontario Power Generation, Nuclear Waste Management Division Report 06819-REP-01200-10154-R00, Toronto, Ontario.

Spiessl, S. M., K. U. Mayer and K. T. B. MacQuarrie. 2006. Reactive transport modelling in fractured rock - Redox Stability Study. Ontario Power Generation, Nuclear Waste Management Division Report No. 06819-REP-01200-10160-R00, Toronto, Ontario.

Srivastava, R.M. 2002. The discrete fracture network model in the local scale flow system for the third case study. Ontario Power Generation, Nuclear Waste Management Division Report 06819-REP-01300-10061-R00. Toronto, Ontario.

Stephansson, Ove, C-F.Tsang, L. Jing and F. Kautsky. 2006. DECOVALEX Project 1992 – 2006: Purposes, tasks and main achievements. In Proc. GeoProc2006 International Symposium: 2nd International Conference on Coupled Thermo-Hydro-Mechanical-Chemical Processes in Geosystems and Engineering, (Editors, W. Xu, X. Tan and S. Yang), p. 31-44, HoHai University, Nanjing, China, May 22-25, 2006.

Stevenson, D.R., A. Brown, C.C. Davison, M. Gascoyne, R.G. McGregor, D.U. Ophori, N.W. Scheier, F. Stanchell, G.A. Thorne and D.K. Tomsons. 1996. A revised conceptual hydrogeologic model of a crystalline rock environment, Whiteshell Research Area, Southeastern Manitoba, Canada. Atomic Energy of Canada Limited Report, AECL-11331, COG-95-271.

Sykes, J.F., S.D. Normani and E.A. Sudicky. 2003. Regional scale groundwater flow in a Canadian Shield setting. Ontario Power Generation, Nuclear Waste Management Division Report 06819-REP-01200-10114-R00, Toronto, Ontario.

Sykes, J.F., S.D. Normani, E.A. Sudicky and R.G. McLaren. 2004. Sub-regional scale groundwater flow within an irregular discretely fractured Canadian Shield setting. Ontario Power Generation, Nuclear Waste Management Division Report 06819-REP-01200-10133-R00, Toronto, Ontario.

Thorne, G.A. and M. Gascoyne. 1993. Groundwater recharge and discharge characteristics in granitic terranes of the Canadian Shield. Presented at IAH 24th Congress on 'Hydrogeolory of Hard Rock', Oslo, Norway, June 28 - July 2, 1993.
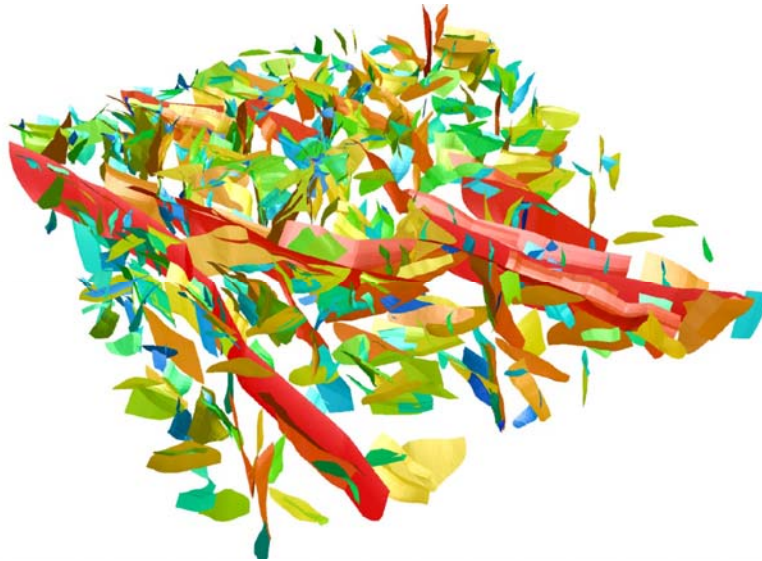
Figure 1: FNM Realization 1 for the Subregional Scale Groundwater Flow Study
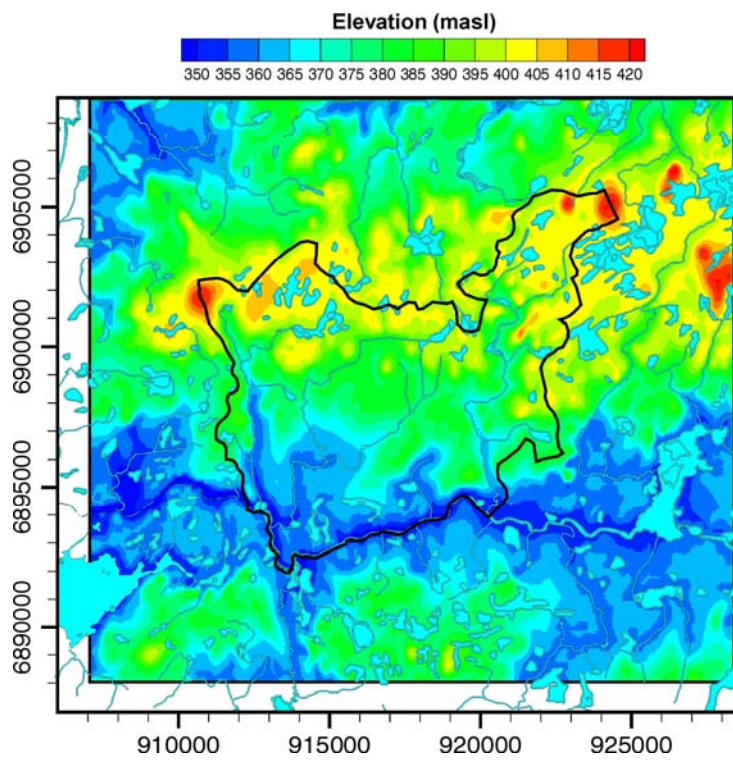
Figure 2: DEM and Water Bodies in the Subregional Flow Study and Site 2a Boundary
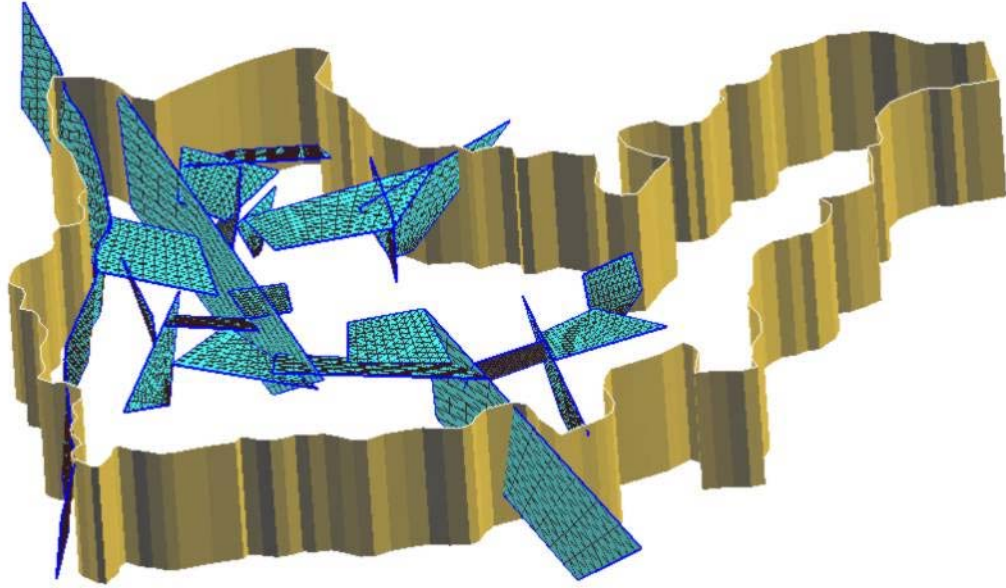
Figure 3: Final Reduced FNM Showing Fracture Zones as Blue Polygons and the Site 2a Model Boundary in Yellowish Grey
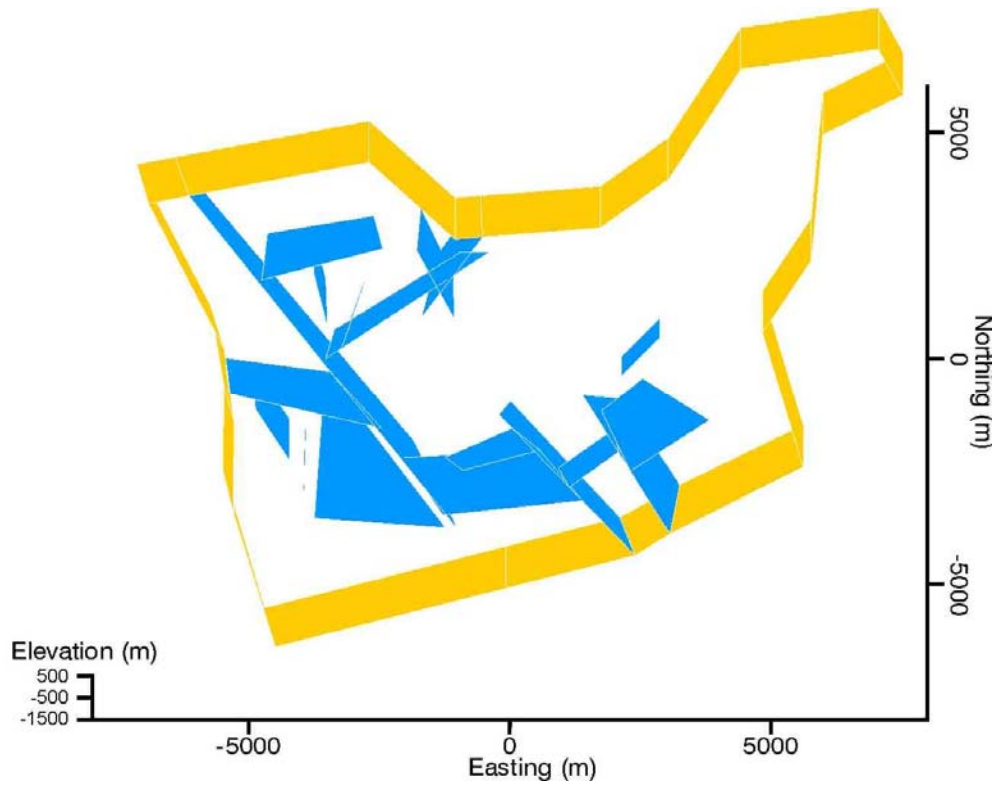
Figure 4: Final Adjusted Simplified Fracture Network Model (blue) with 19 Fracture Zones Shown with Task E Boundary (yellow)
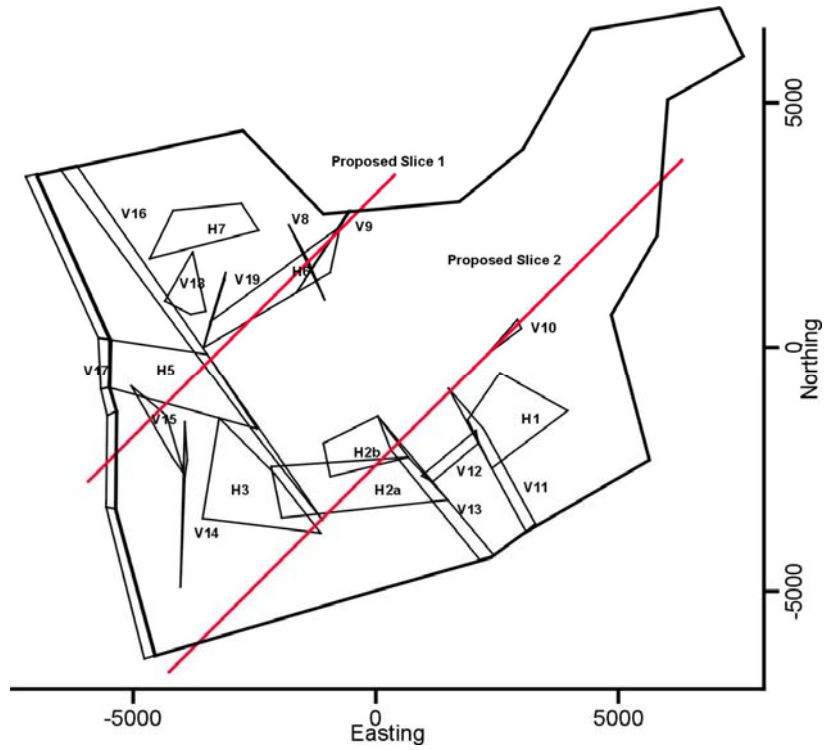
Figure 5: Vertical Sections Considered for 2D THM Modelling
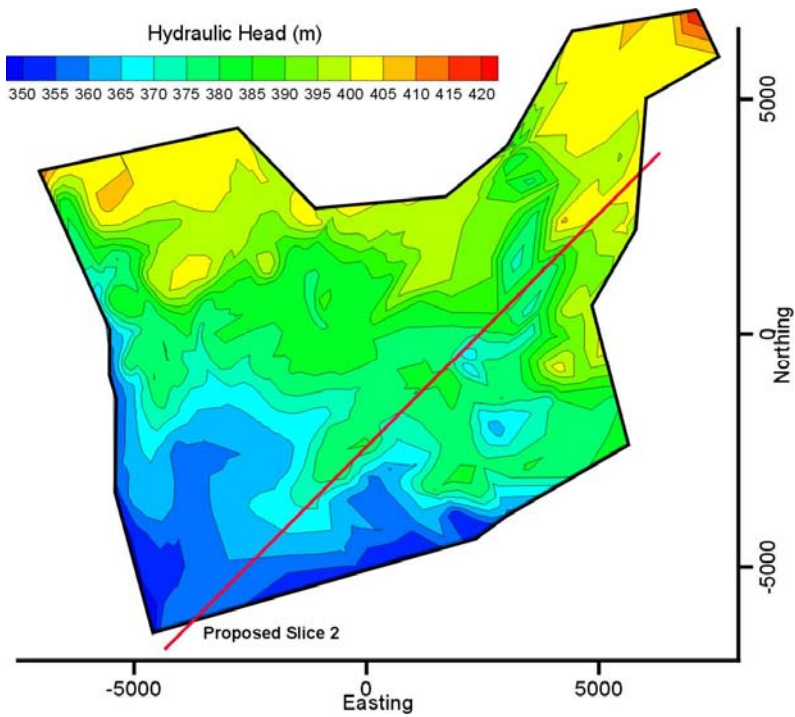
Figure 6: Vertical Section 2 Used for the 2D THM Modelling shown with Steady-State Head Contours under Topographic Drive
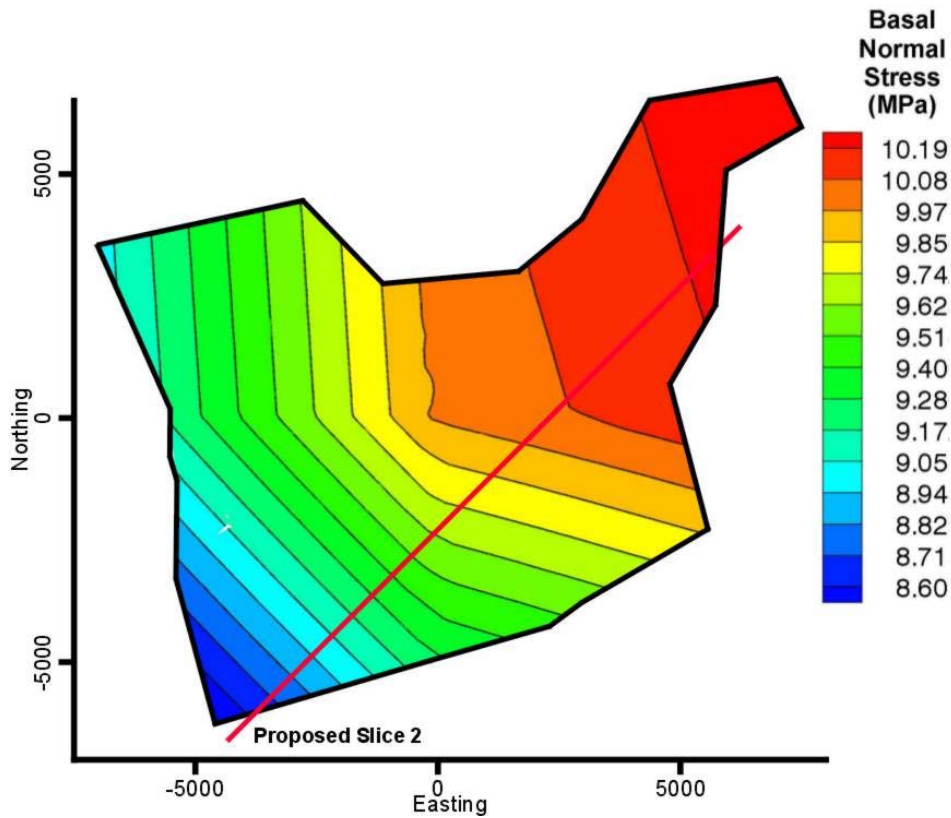
Figure 7: Vertical Slice 2 Used for the 2D THM Modelling Shown with Basal Normal Stress Contours (after GSM Realization nn2008, Peltier, private communication 2004, 2006)
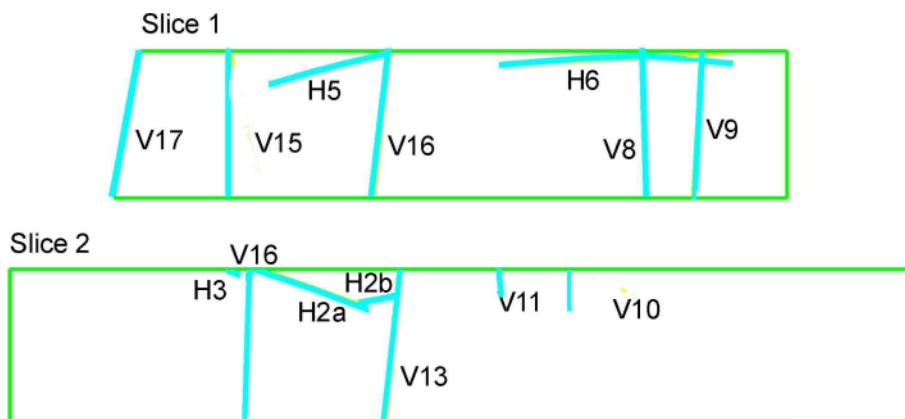
Figure 8: The Two Vertical Sections Through the 3D Conceptual Model Showing Fracture Zone Traces
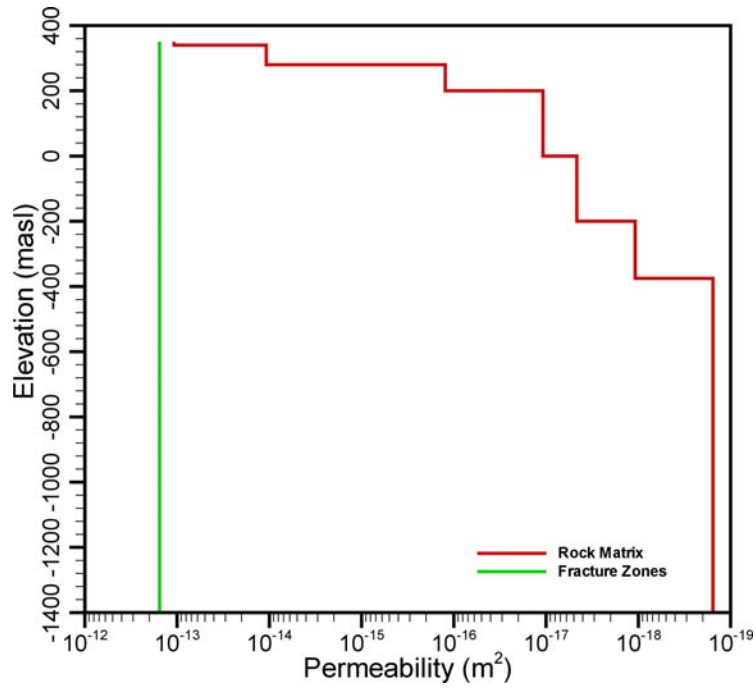
Figure 9: Vertical Profile of Permeability in Rock Mass and in Fracture Zones
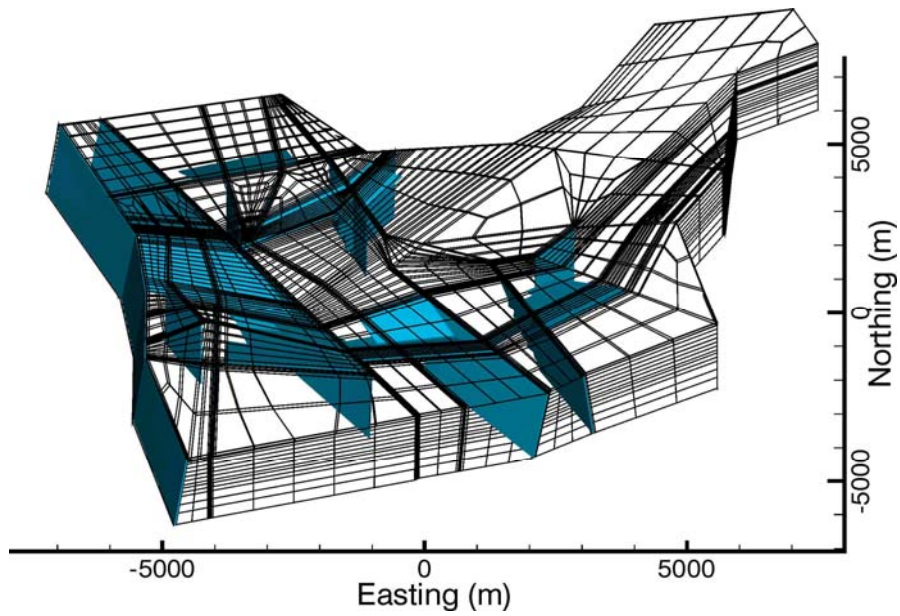
Figure 10: A 3D View of Finite-Element Mesh for Coupled HM and THM Modelling In Task E Showing Fracture Plane Locations (blue)
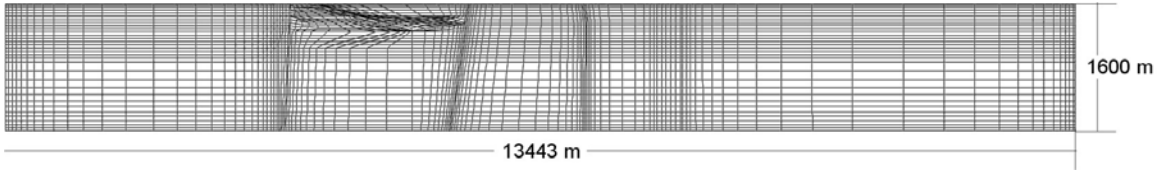
Figure 11: Finite-Element Discretization of Slice 2, the Vertical Section Selected for 2D THM Modelling
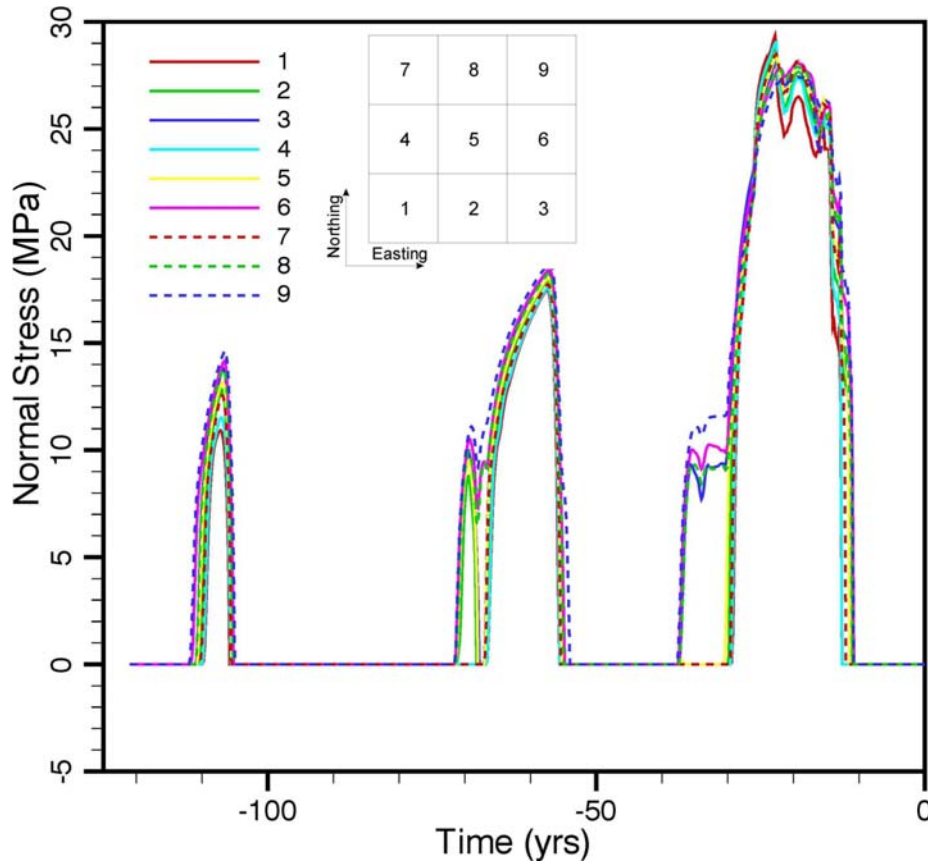
Figure 12: Basal Normal Stress (MPa) at 9 Grid Cells (after Peltier's GSM Realization nn2008, private communication, 2004, 2006)
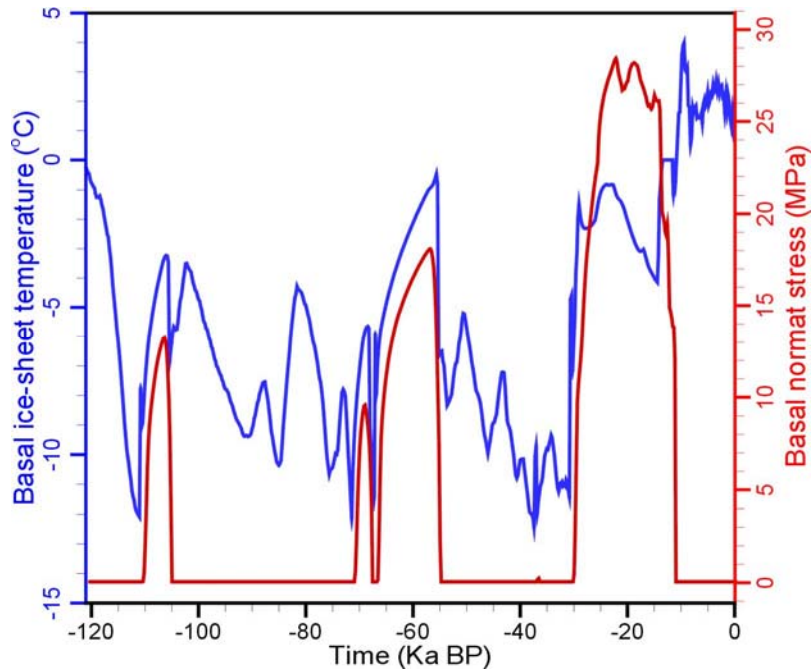
Figure 13: Temporal Evolution of Basal Temperature and Normal Stress at Centre of Grid Cell 5 for the Cold-based Scenario (GSM Realization nn2008, Peltier, private communication, 2004, 2006)
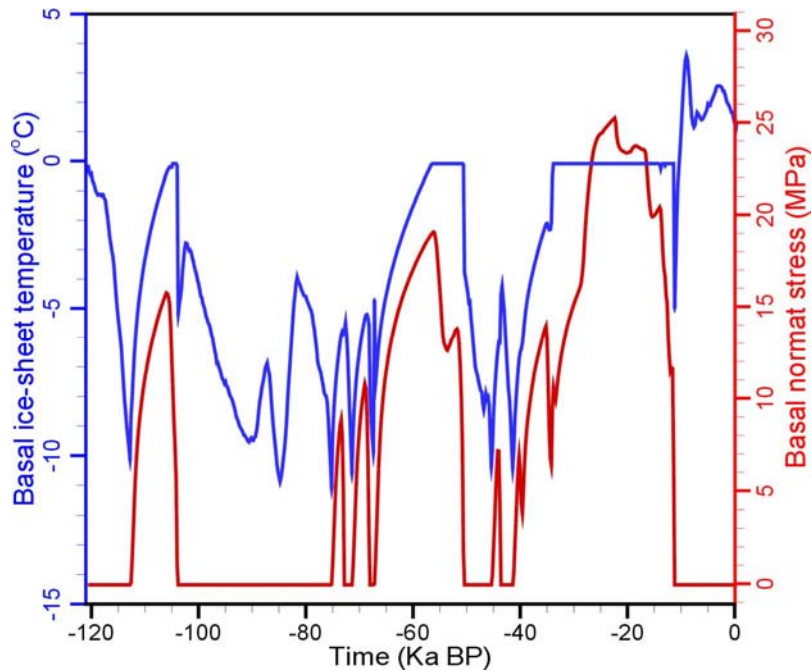
Figure 14: Temporal Evolution of Basal Temperature and Normal Stress at Centre of Grid Cell 5 for the Warm-based Scenario (GSM Realization nn2778, Peltier, private communication, 2005, 2006)
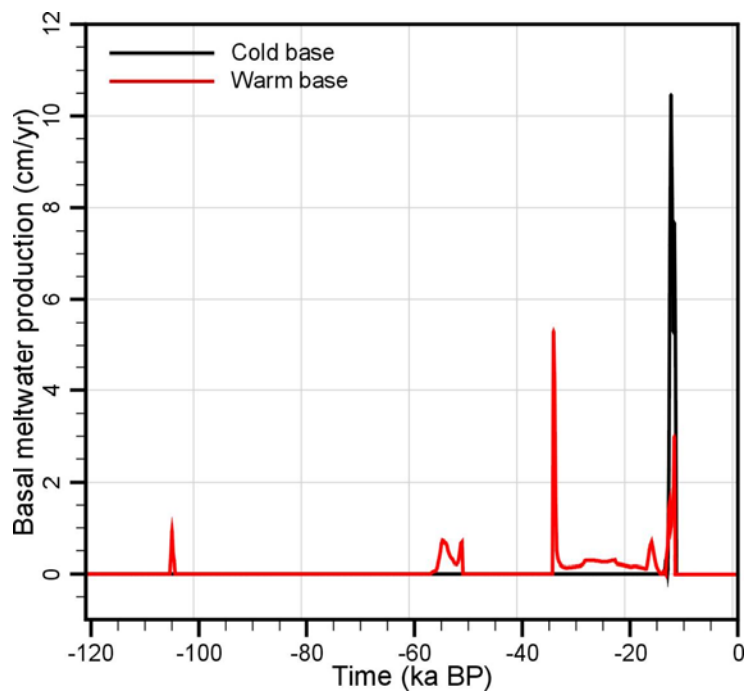
Figure 15: Temporal Evolution of Basal Meltwater Production Rate for the Two Glacial Scenarios (nn2008 and nn2778)
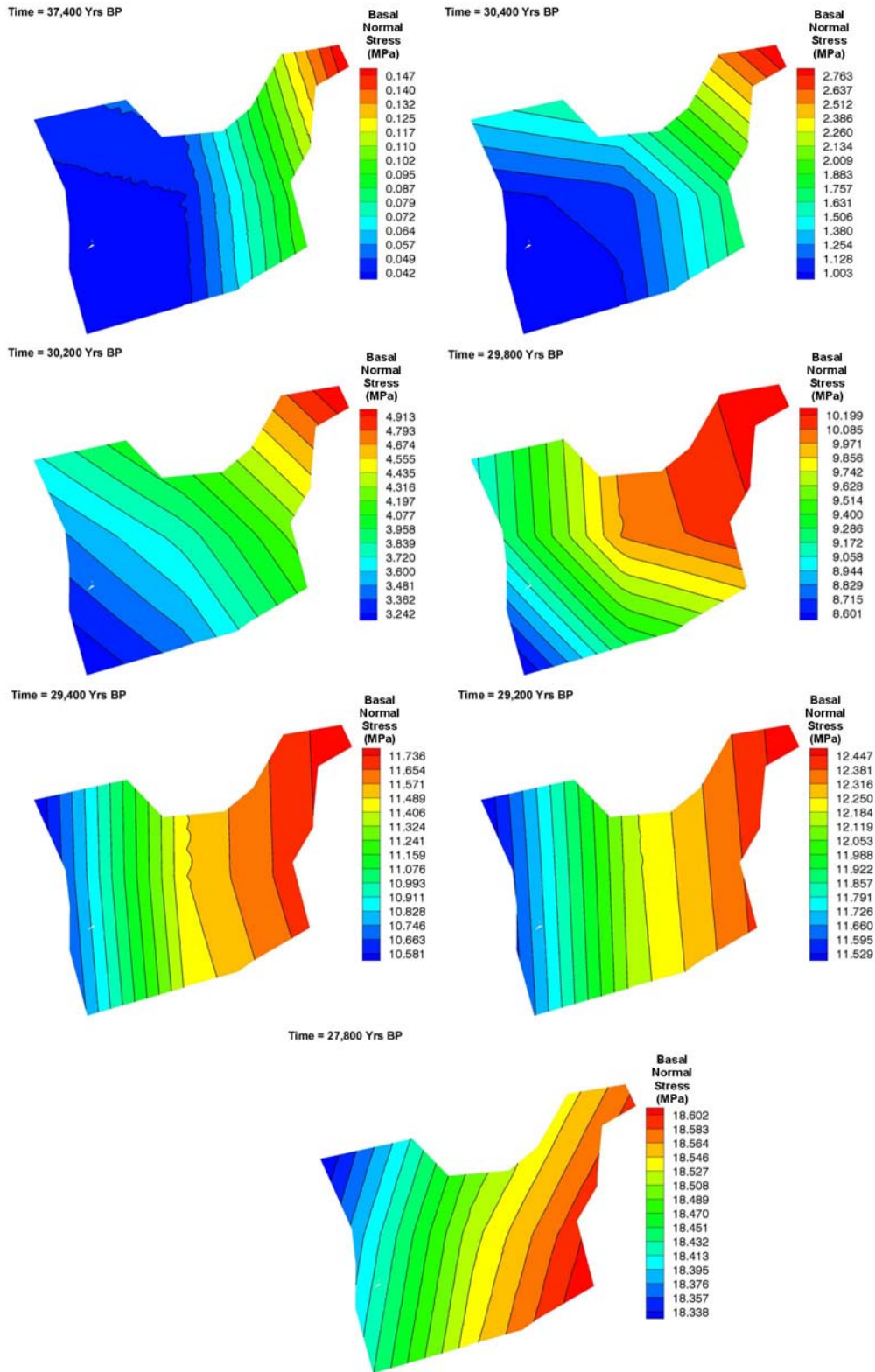
Figure 16: Basal Normal Stress (MPa) Contours at Various Times Interpolated from Peltier's Model Results (private communication, 2004, 2006)
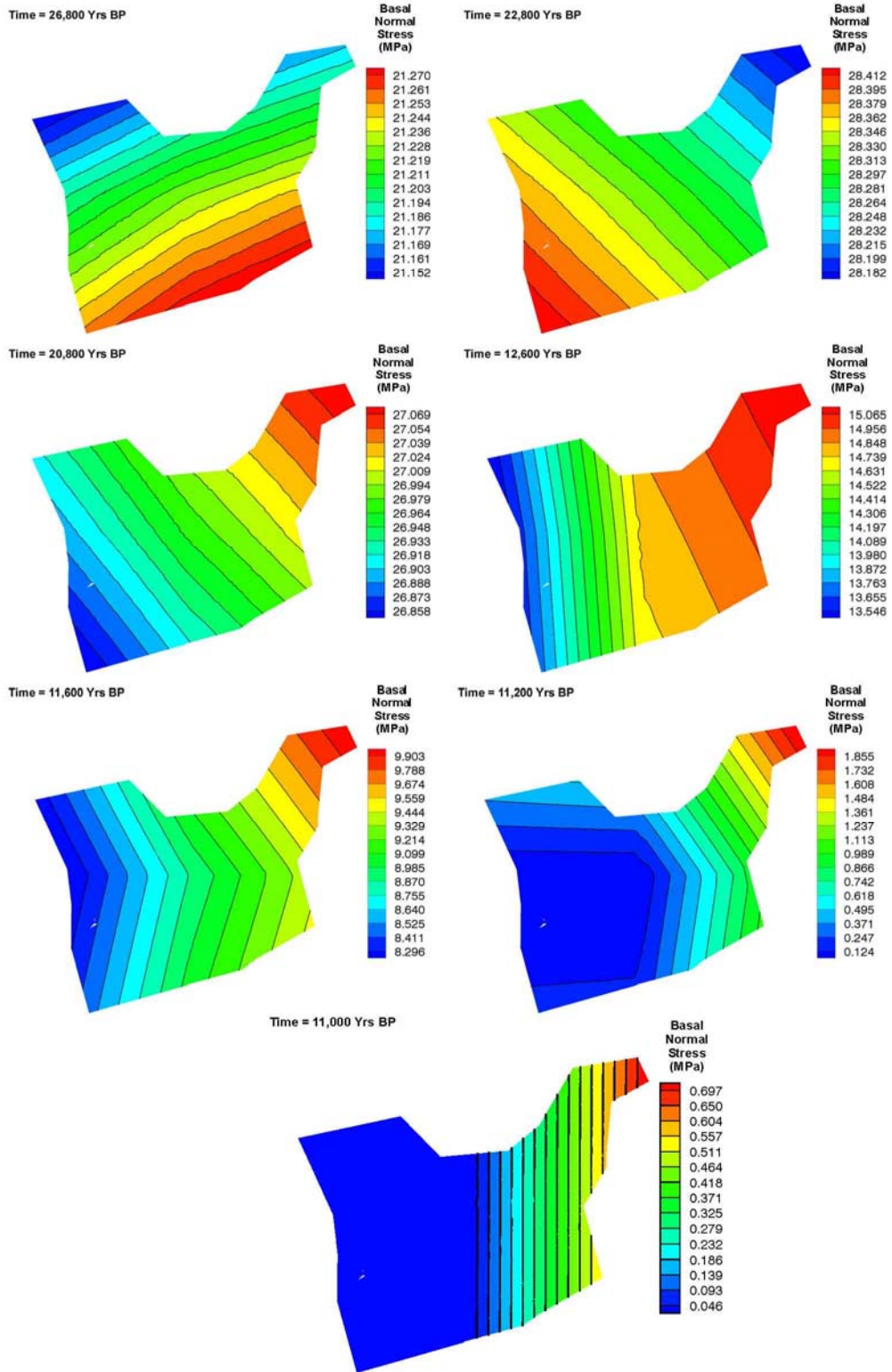
Figure 16 (continued): Basal Normal Stress (MPa) Contours at Various Times Interpolated from Peltier's Model Results (private communication, 2004, 2006)
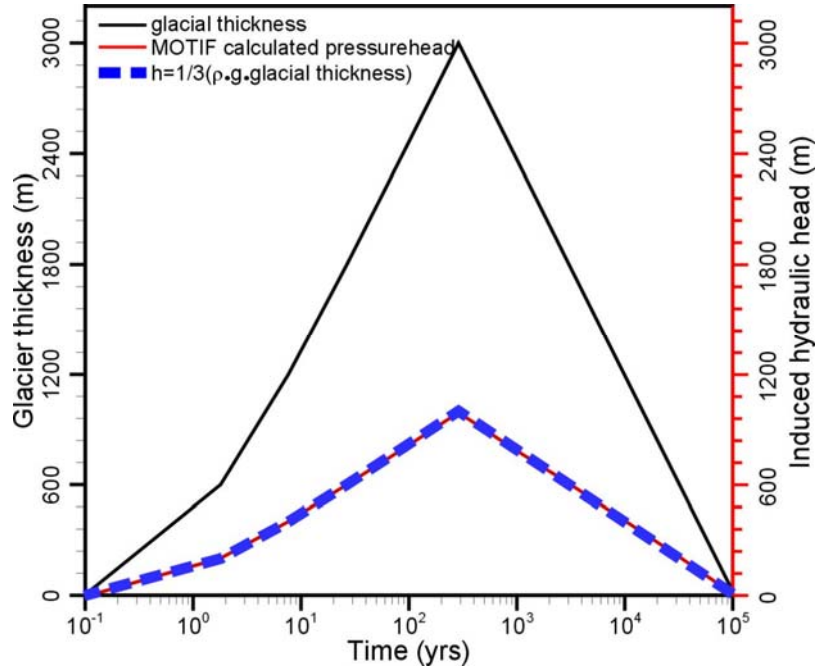
Figure 17: Temporal Evolution of Idealized Glacial Loading/Unloading and Resulting Equivalent Freshwater Head Change According to a Simple HM Column Model

a).
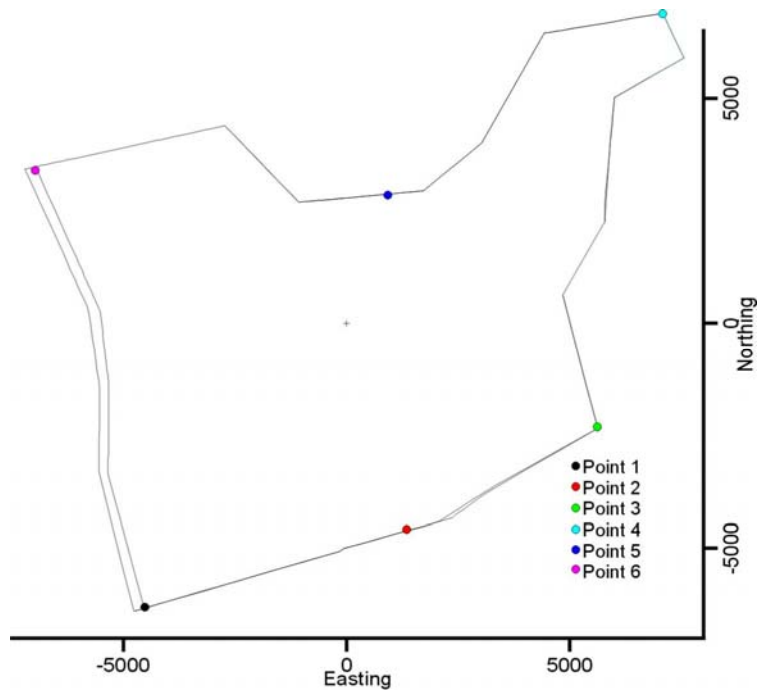
b).
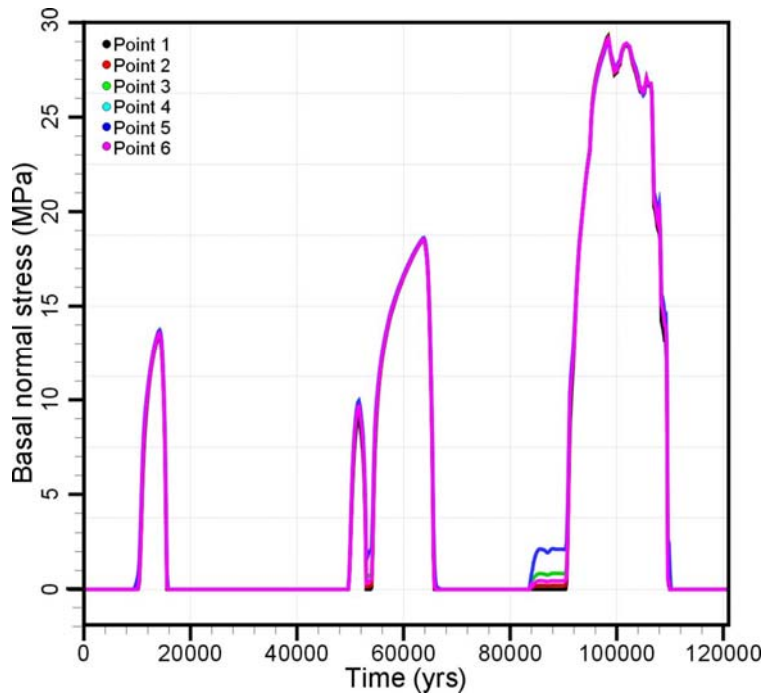
Figure 18: Temporal Evolution of Mechanical and Hydraulic Boundary Conditions at Selected Locations Along the Task E Model Perimeter: a) Locations and b) Basal Normal Stress for Cold-based Scenario

c).
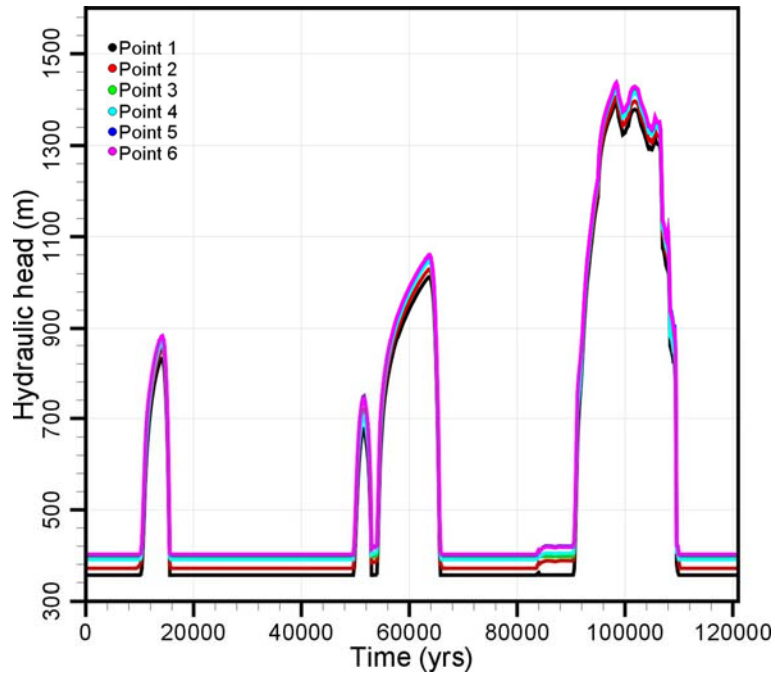
d).
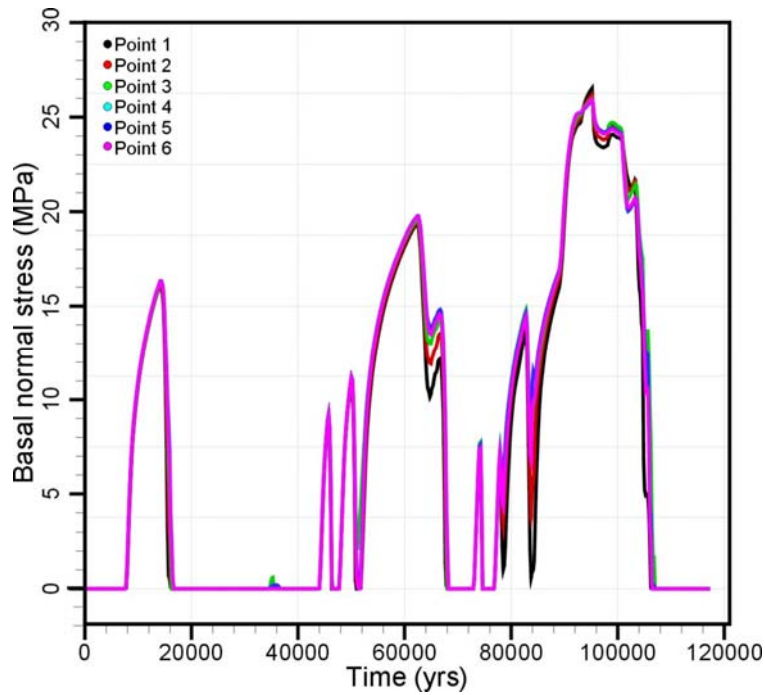
Figure 18 (continued): Temporal Evolution of Mechanical and Hydraulic Boundary Conditions at Selected Locations Along the Task E Model Perimeter: c) Hydraulic Head for Cold-based Scenario and d) Basal Normal Stress for Warm-based Scenario

e).
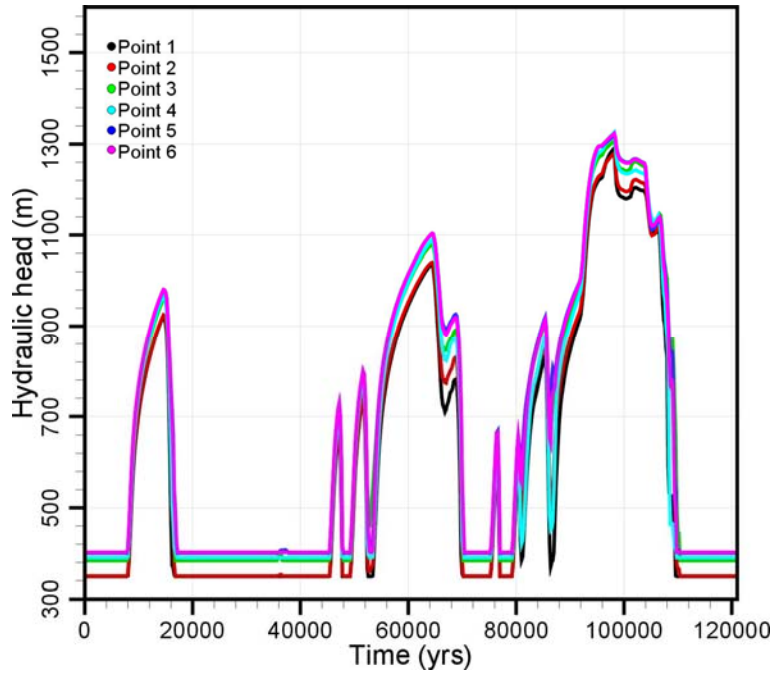
Figure 18 (concluded): Temporal Evolution of Mechanical and Hydraulic Boundary Conditions at Selected Locations Along the Task E Model Perimeter: e) Hydraulic Head for Warm-based Scenario.
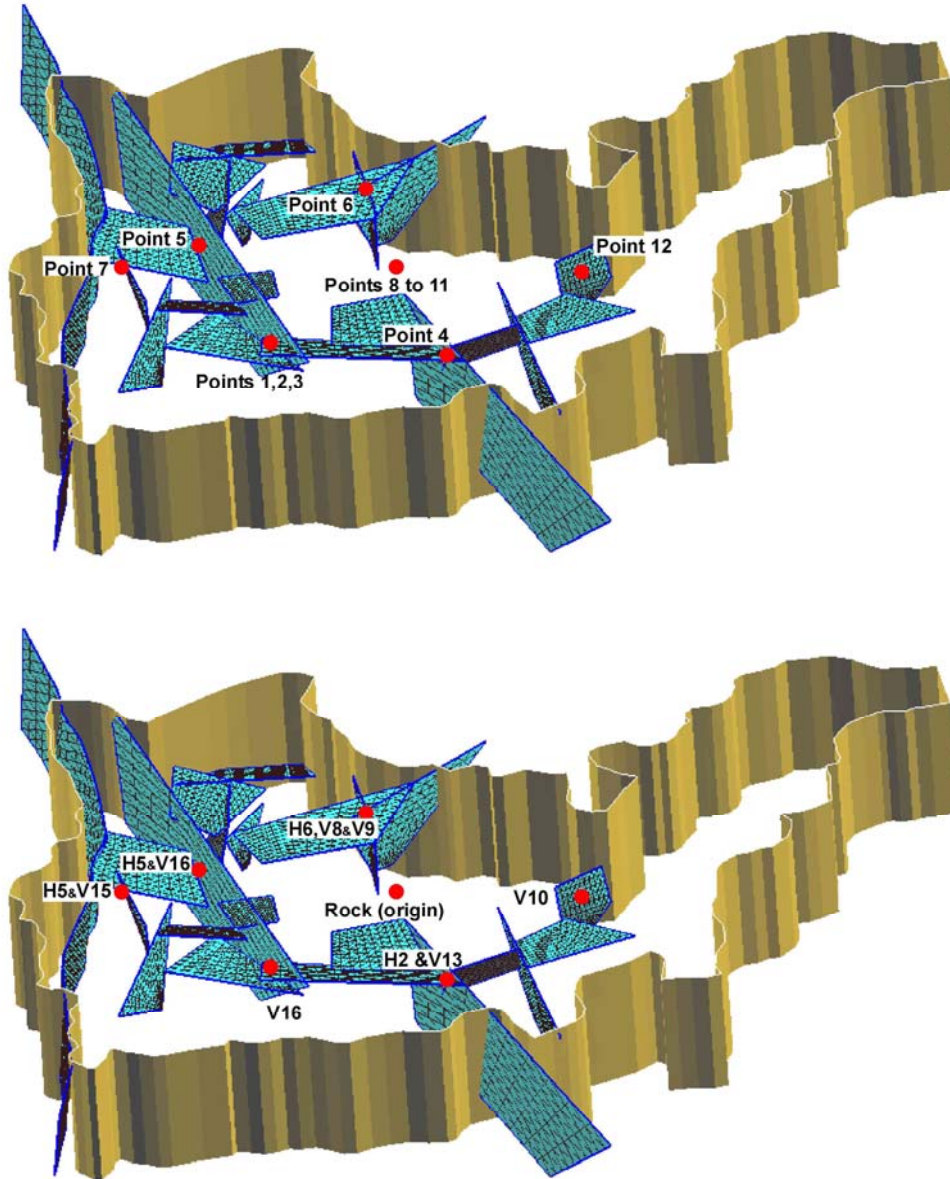
Figure 19: Selected Locations for Graphical Display of Temporal Evolution of Dependent Variables. Top - With Locations Labelled; Bottom - With FZs Labelled
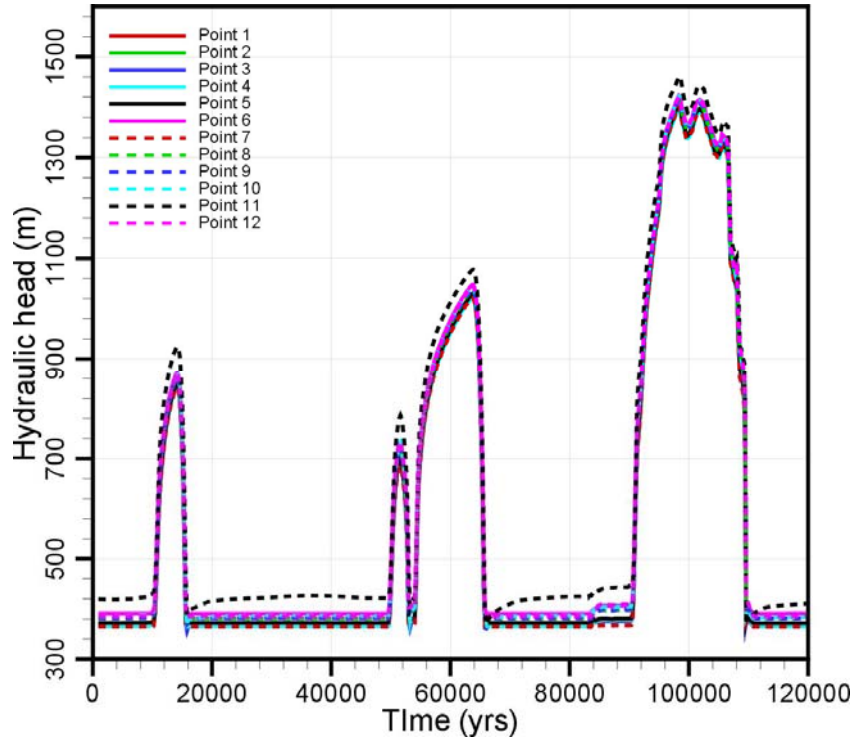
Figure 20: Temporal Evolution of Hydraulic Head at Selected Points from R_THMC Simulation (THM with Depth Dependent Salinity)
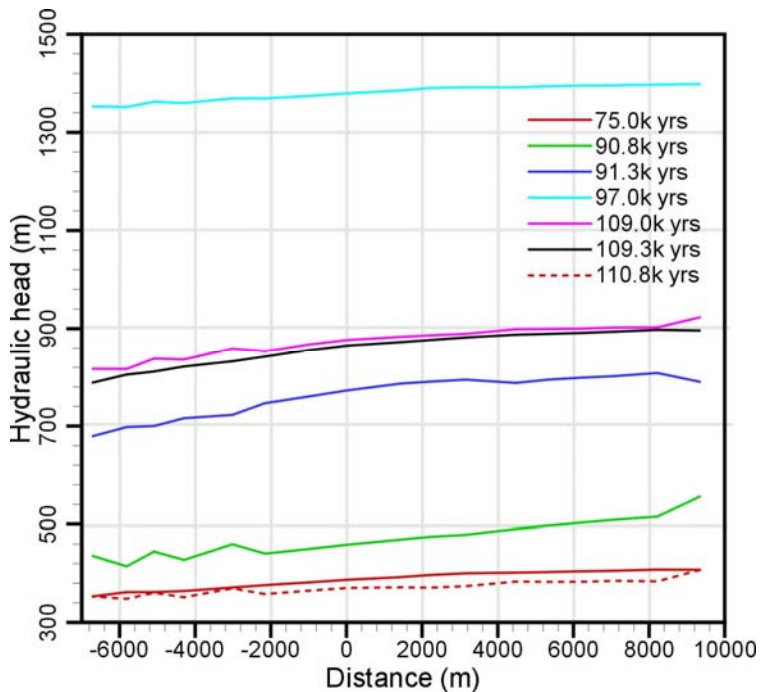
Figure 21: Hydraulic Head from R_THMC Simulation (THM with Depth Dependent Salinity) Versus Horizontal Distance Along a Horizontal Line at 670 m Below Surface Lying in a Vertical Plane Through the Model Origin Parallel to the Two Slices Shown in Figure 5 for Specified Times
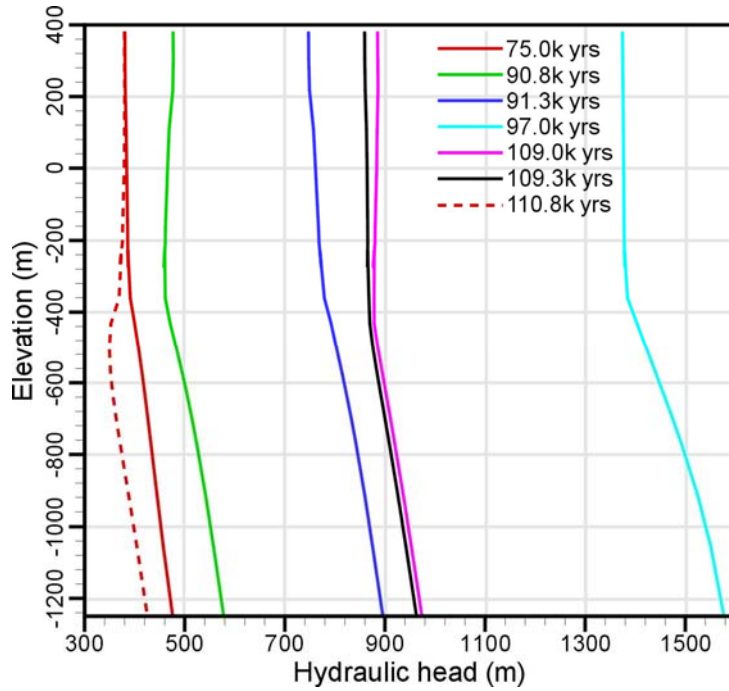
Figure 22: Hydraulic Head Through Model Origin from R_THMC Simulation (THM with Depth Dependent Salinity) Versus Elevation (masl) for Specified Times
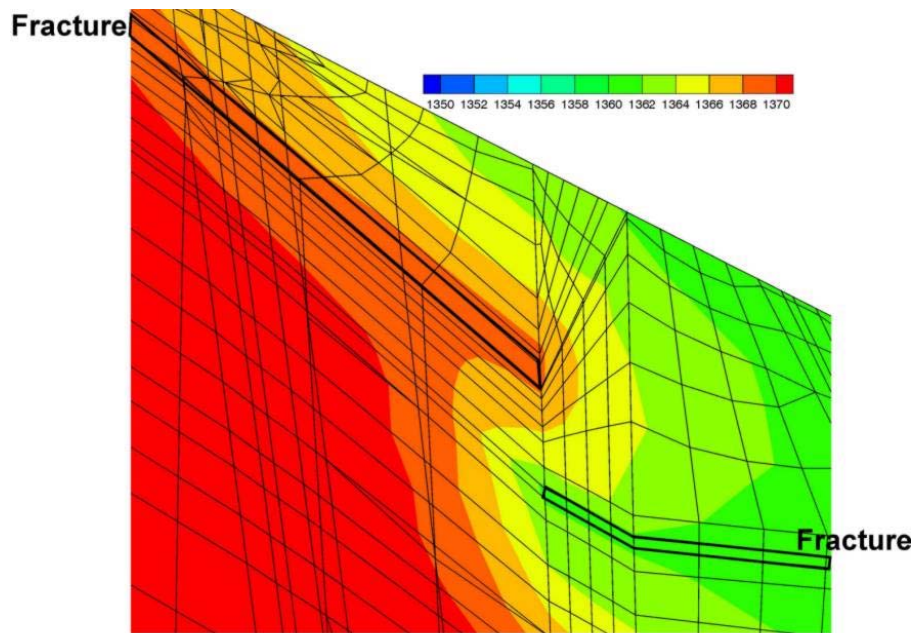
Figure 23: Hydraulic Head in Fracture Zones and Adjacent Rock Mass as Predicted by 3D R_HM Model. Contour Interval = 2 m.
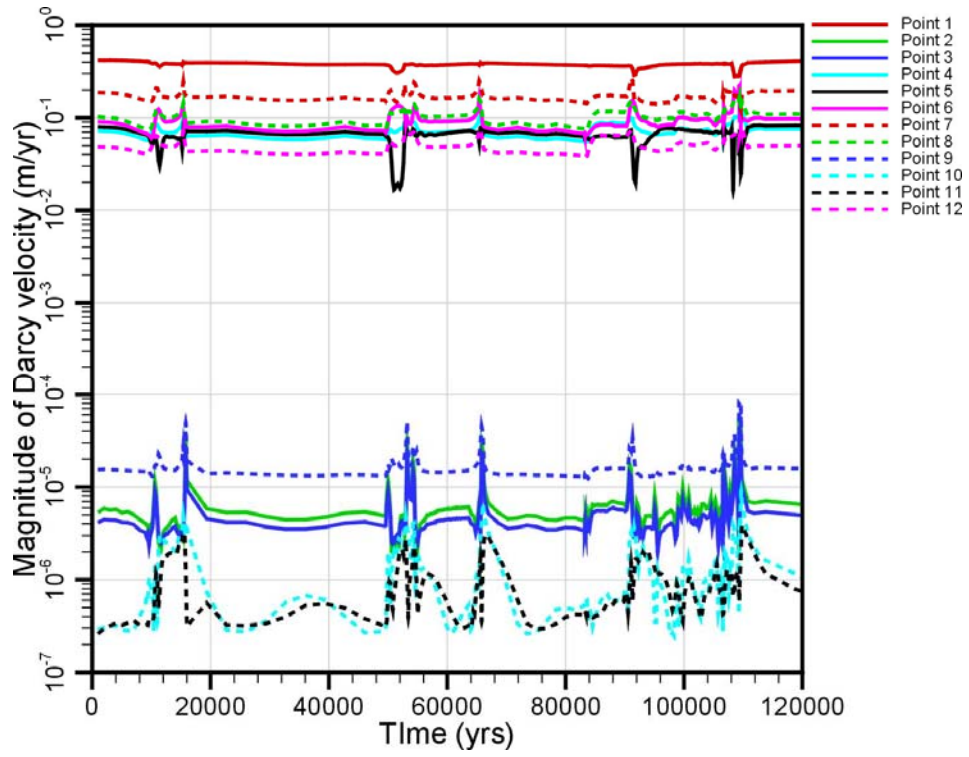
Figure 24: Temporal Evolution of Darcy Flux Magnitude from Real_THMC (THM with Depth Dependent Salinity) Simulation
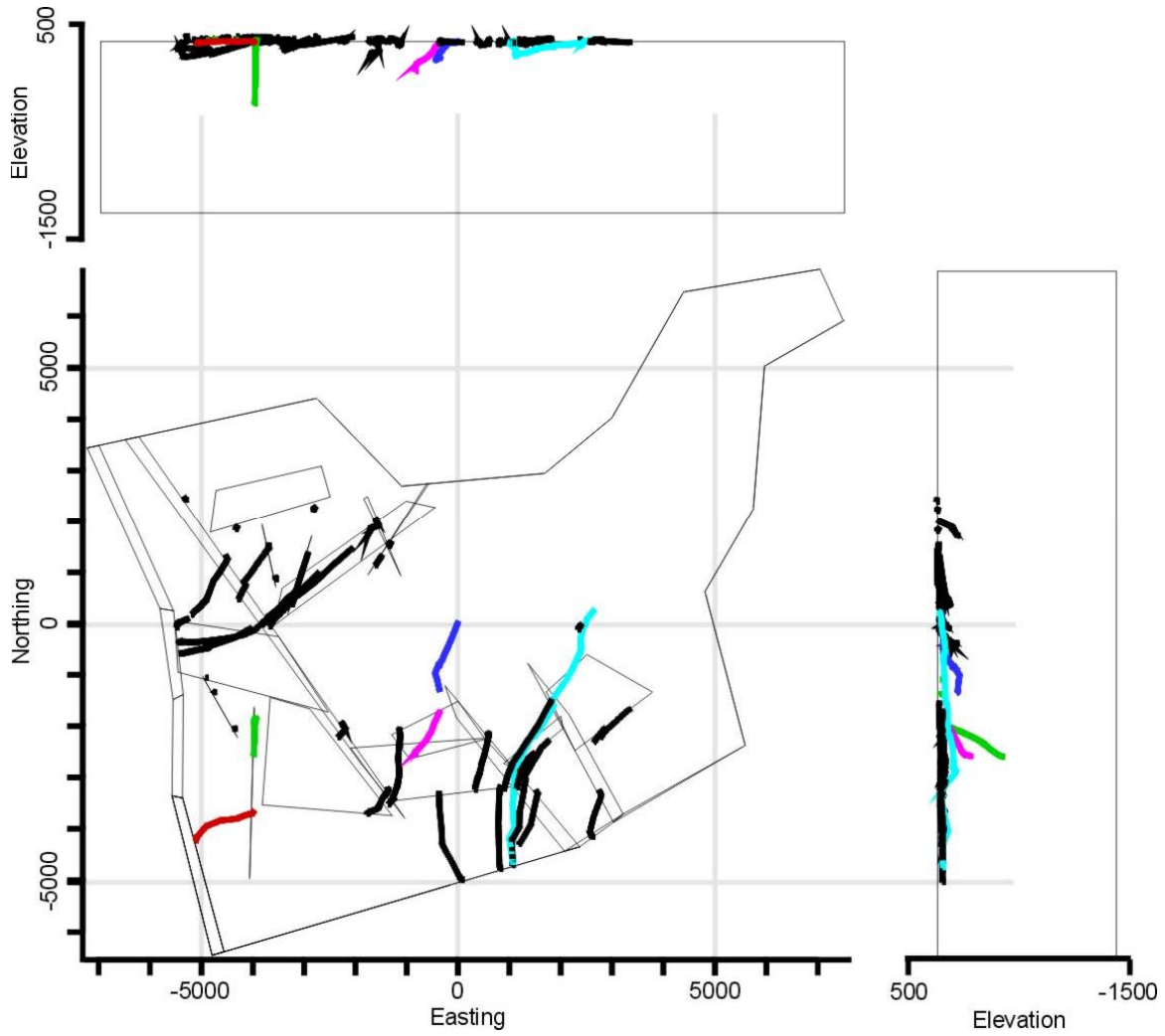
Figure 25: Plan and Section Views of 38 Particle Tracks Starting at Beginning of Meltwater Production According to R_THMC (THM With Depth Dependent Salinity) Simulation. Deepest particle paths are highlighted by colour.
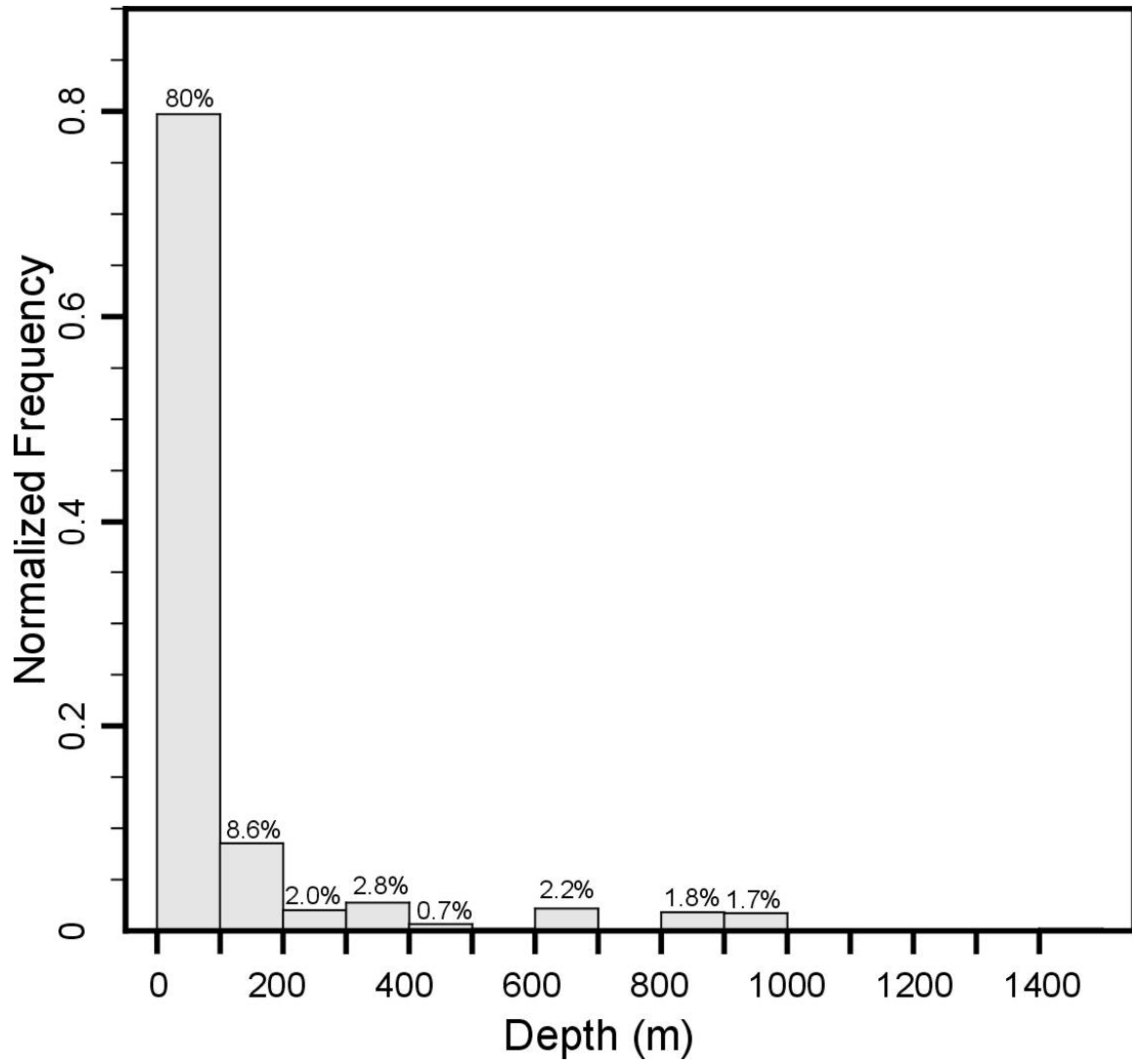
Figure 26: Normalized Histogram of Maximum Depth of Meltwater Recharge as Predicted by R_THMC (THM with Depth Dependent Salinity) Simulation
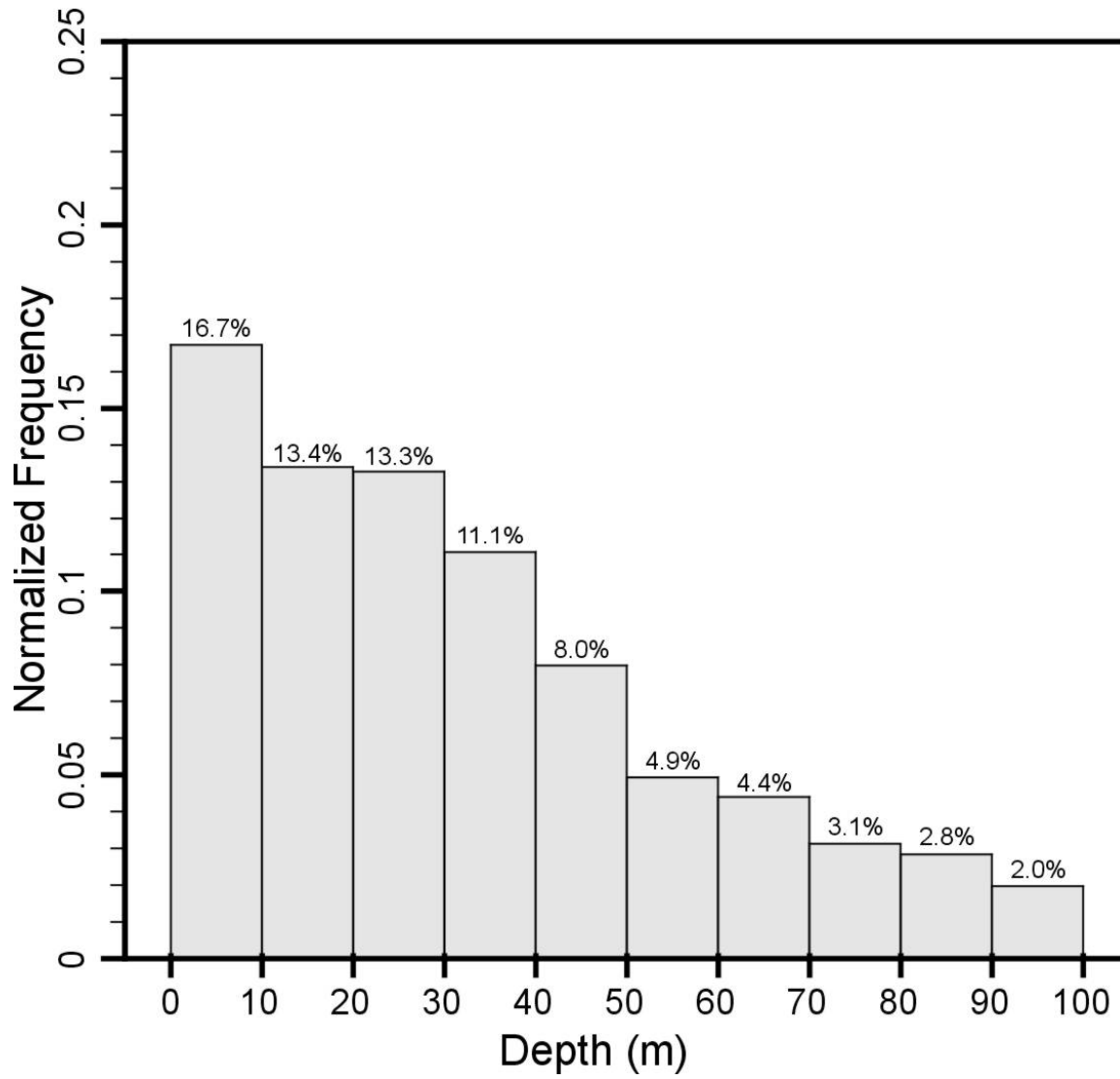
Figure 27: Normalized Histogram of Maximum Depth of Meltwater Recharge Within the Top 100-m Depth Below Surface as Predicted by the R_THMC (THM with Depth Dependent Salinity) Simulation
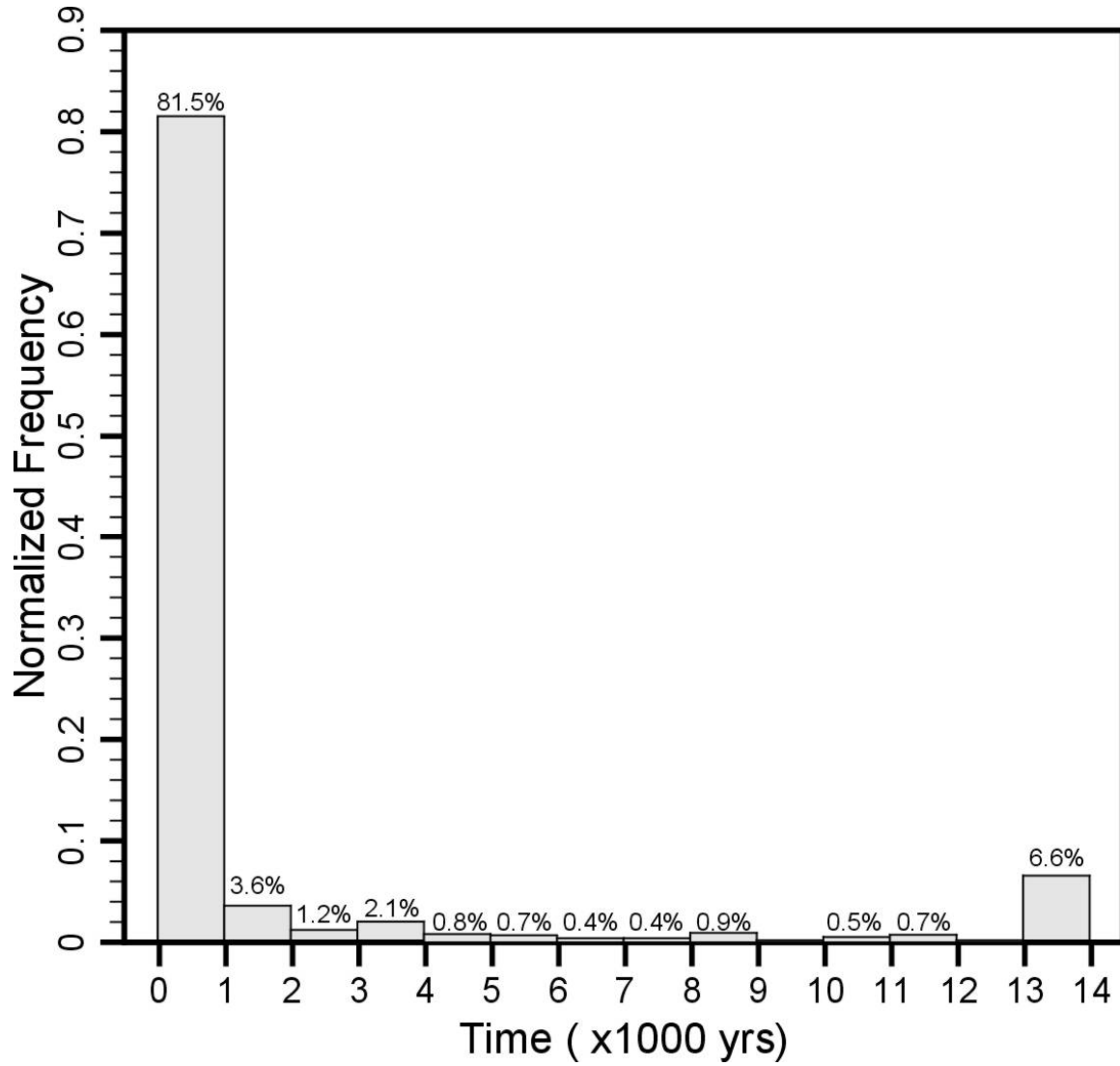
Figure 28: Normalized Histogram of Time for Meltwater to Recharge to Maximum Depth as Predicted by the R_THMC (THM with Depth Dependent Salinity) Simulation
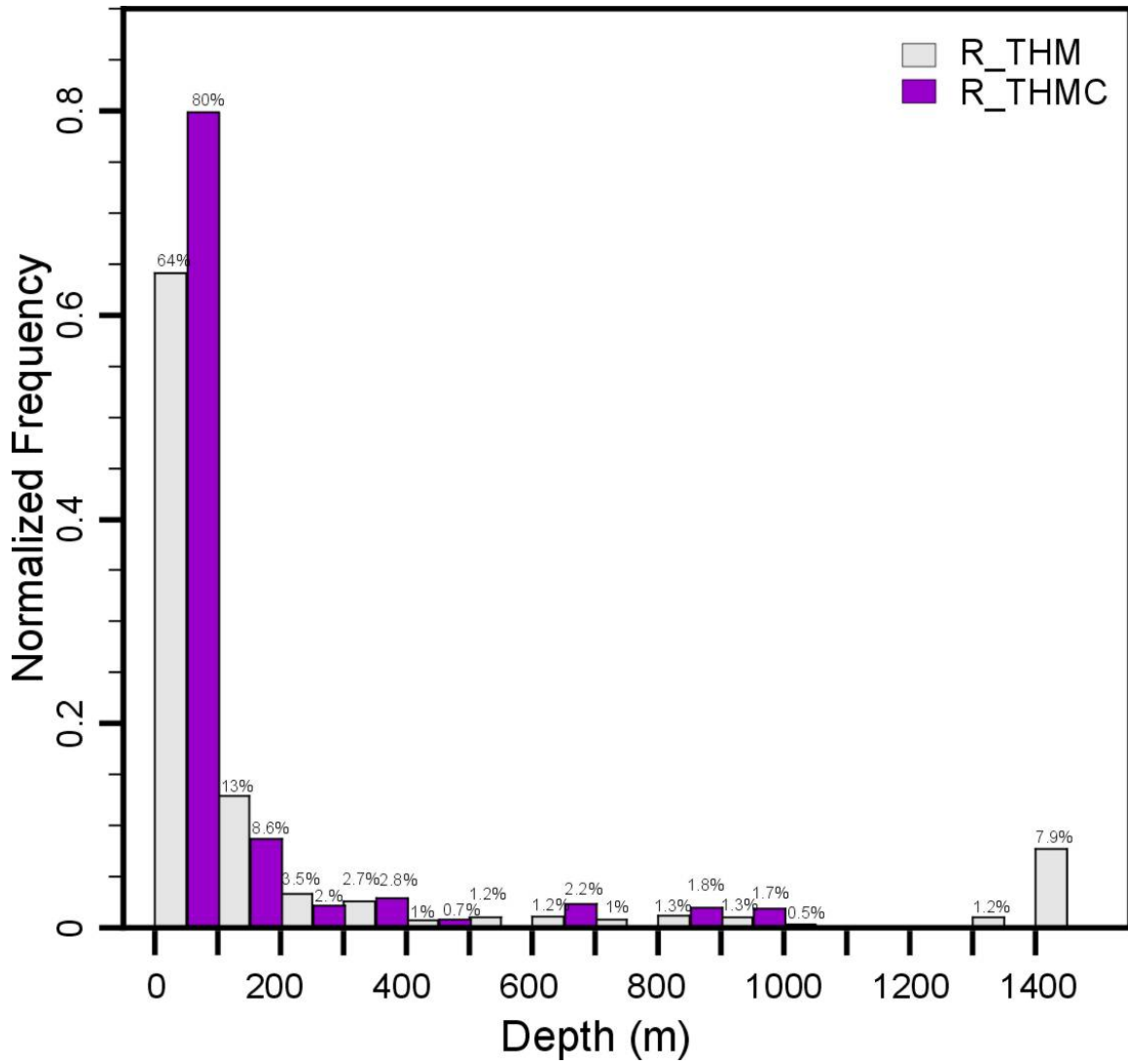
Figure 29: Normalized Histogram of Maximum Depth of Meltwater Recharge as Predicted by the 3D Simulation Runs R_THM and R_THMC (THM with Depth Dependent Salinity)
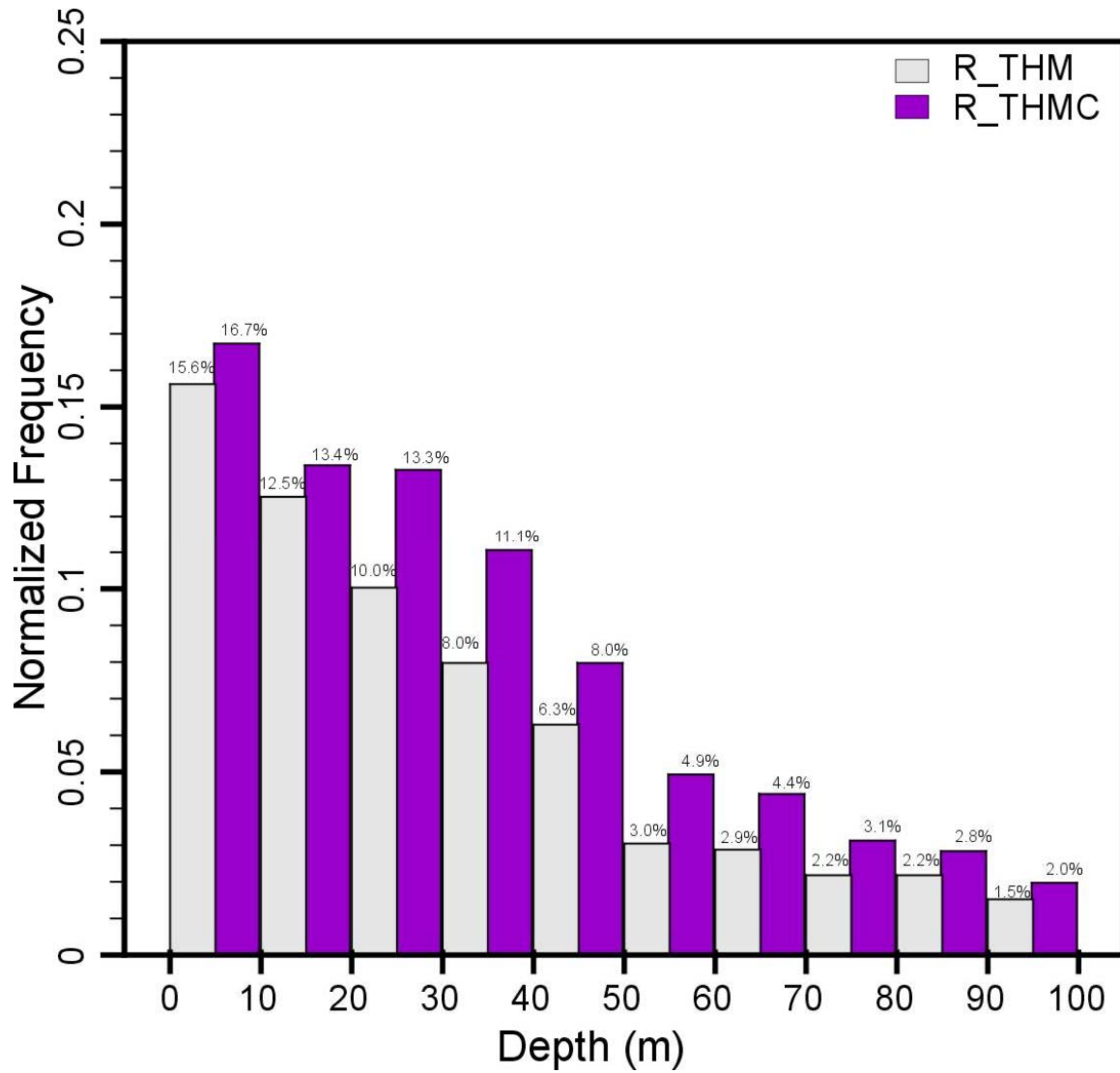
Figure 30: Normalized Histogram of Maximum Depth of Meltwater Recharge Within the Top 100-m Depth Below Surface as Predicted by the 3D Simulation Runs R_THM and R_THMC (THM with Depth Dependent Salinity)
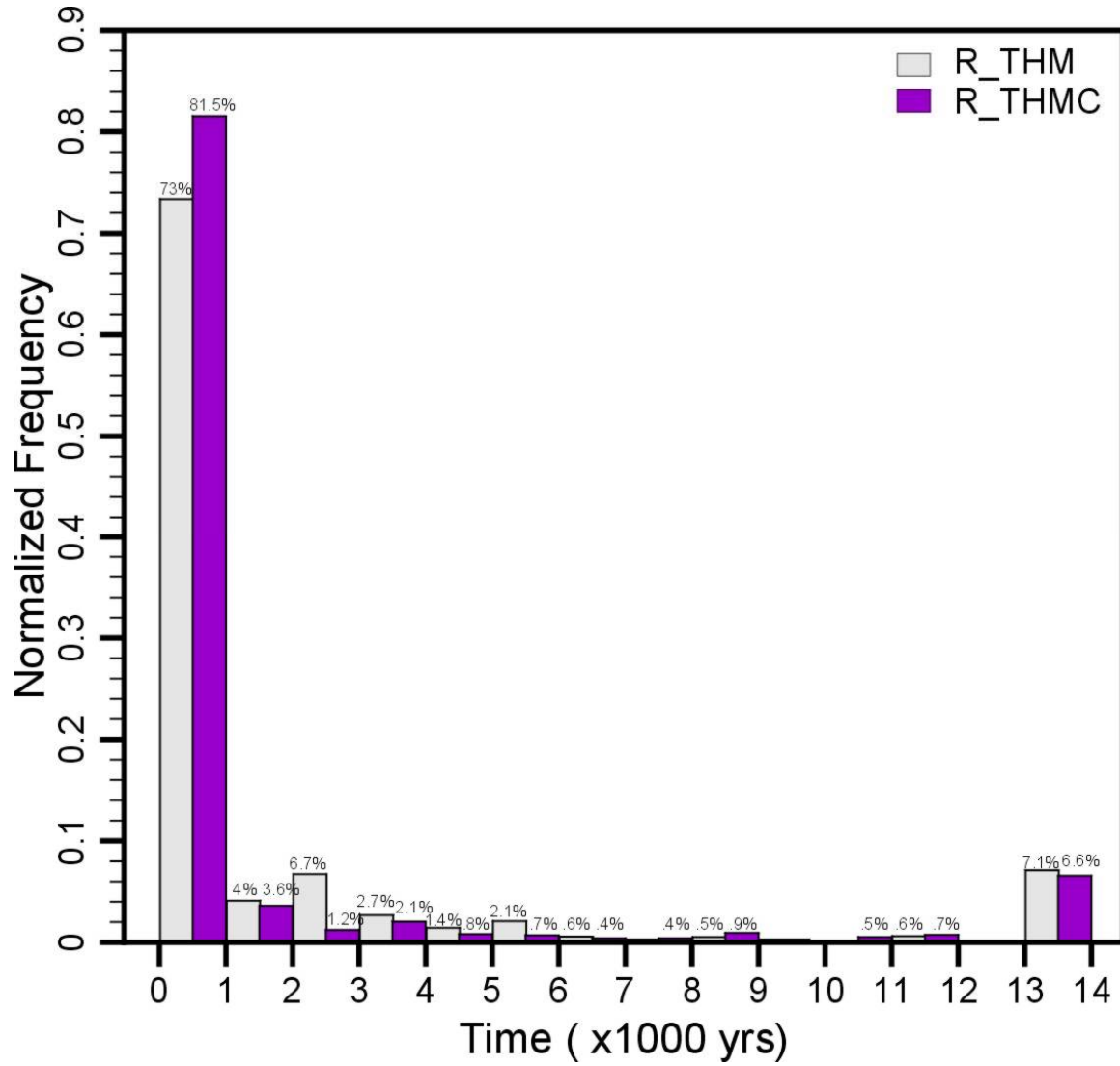
Figure 31: Normalized Histogram of Time for Meltwaters to Recharge to Maximum Depth as Predicted by 3D Simulation Runs R_THM and R_THMC (THM with Depth Dependent Salinity)
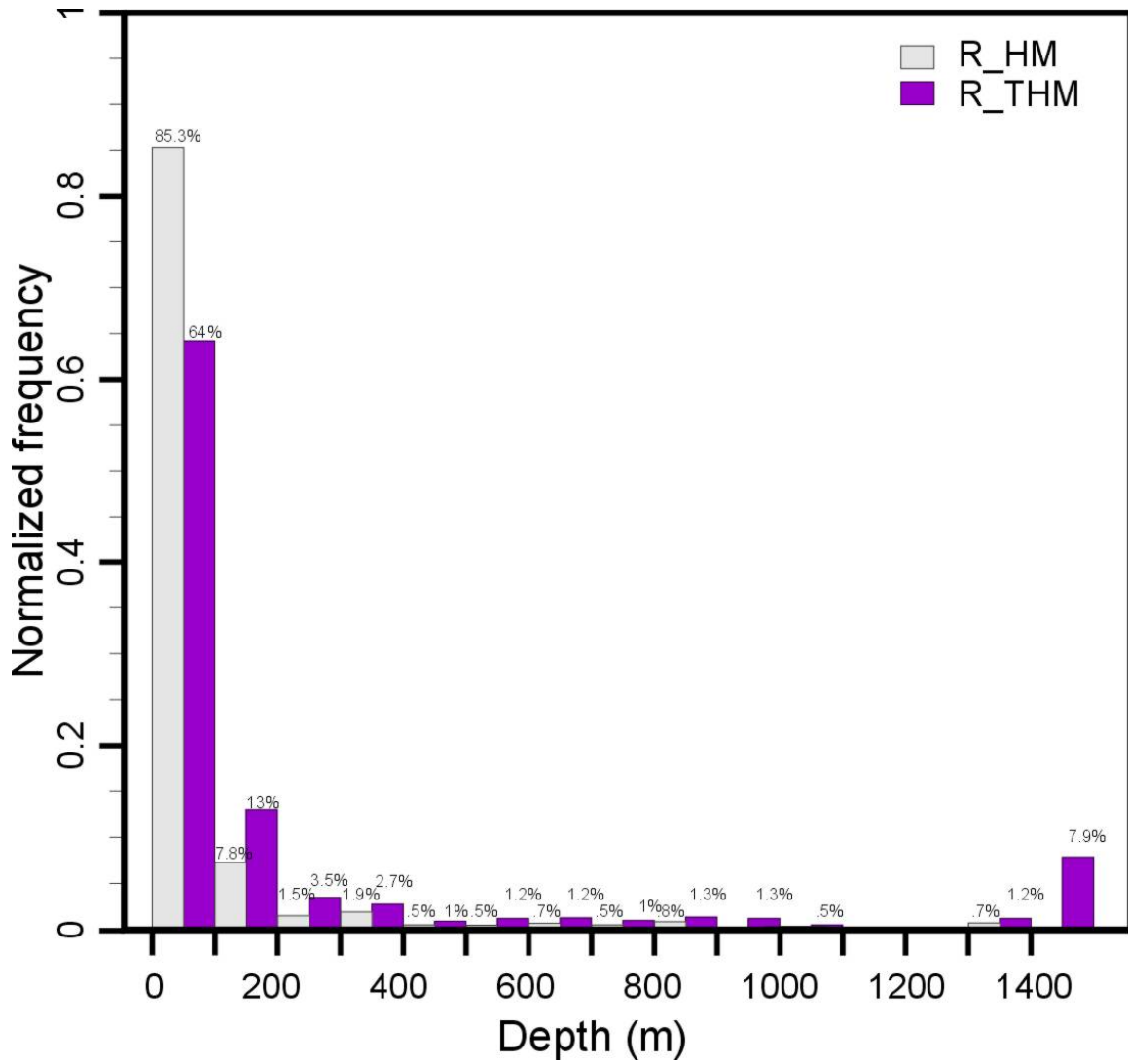
Figure 32: Normalized Histogram of Time for Meltwaters to Recharge to Maximum Depth as Predicted by 3D Simulation Runs R_HM and R_THM
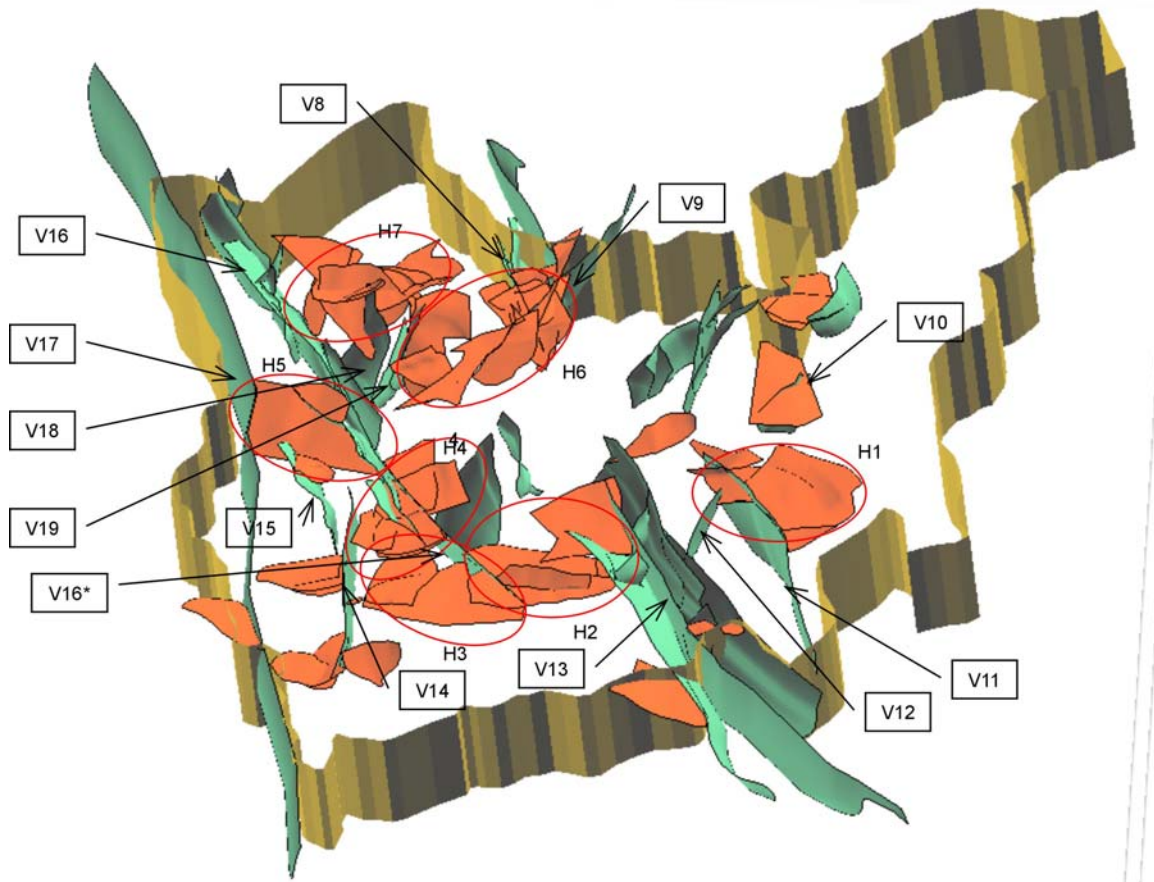
Figure 33: Vertical (Green) and Low and Intermediate Dip (Orange) Fracture Zones (FZ) Represented in the 3D Conceptual Model for Task E. These FZs can be Grouped i) by Orientation: Vertical Set #1 – V9, V10, & V12; Vertical Set #2 – V16, V17, V13, V11, V15, V14,, V18, V19, & V8; LID Set #1 – H1, H2a, H3 & H7; and LID Set #2 – H5, H2b, & H6; and ii) by Interconnectivity: Connected Set #1 – H1, H2a & b, H5, V11, V12, V13, V15, V16, and V17; Connected Set #2 – H6, V8, V9, and V19; and Unconnected FZs: H3, H7, V10, V14 and V18.
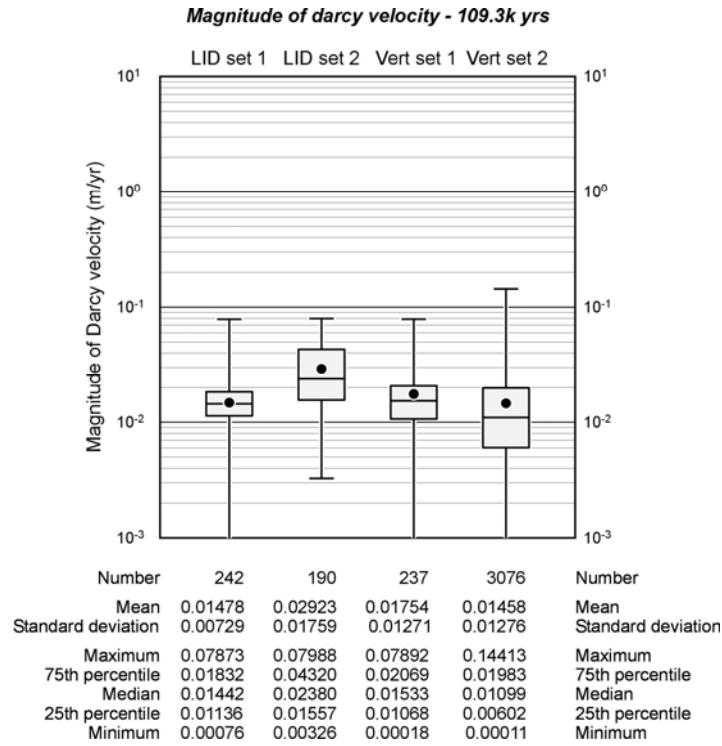
Figure 34: Box-whisker Summary Statistics Plots of Darcy Velocity Magnitude Predicted by Simulation Run R_THMC (THM with Depth Dependent Salinity) in Different FZ Sets Grouped by Orientation at 109.3 kyr
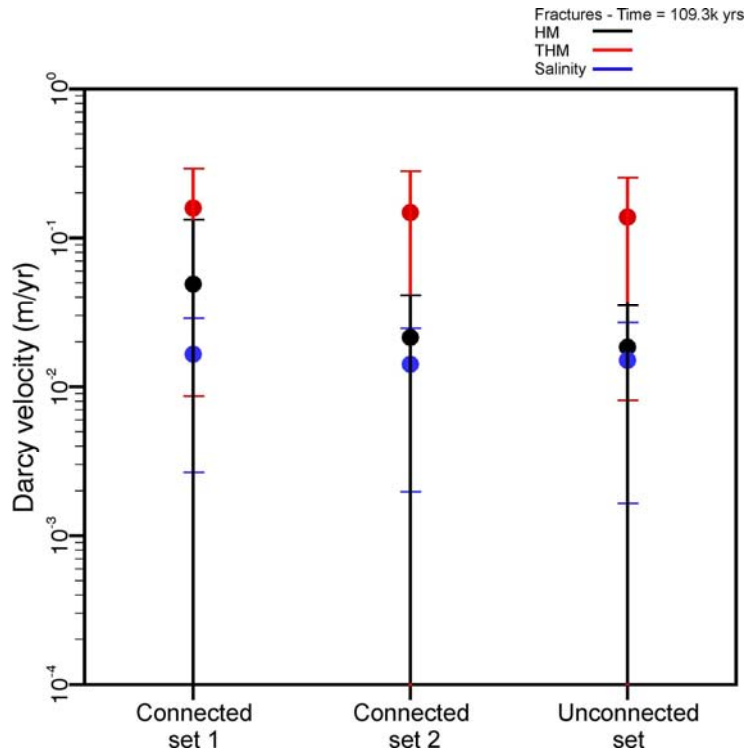
Figure 35: Mean and Standard Deviation of Darcy Velocity Magnitude Predicted by Simulation Run R_THMC (THM with Depth Dependent Salinity) in Different Interconnected (or not) FZ Sets at 109.3 kyr
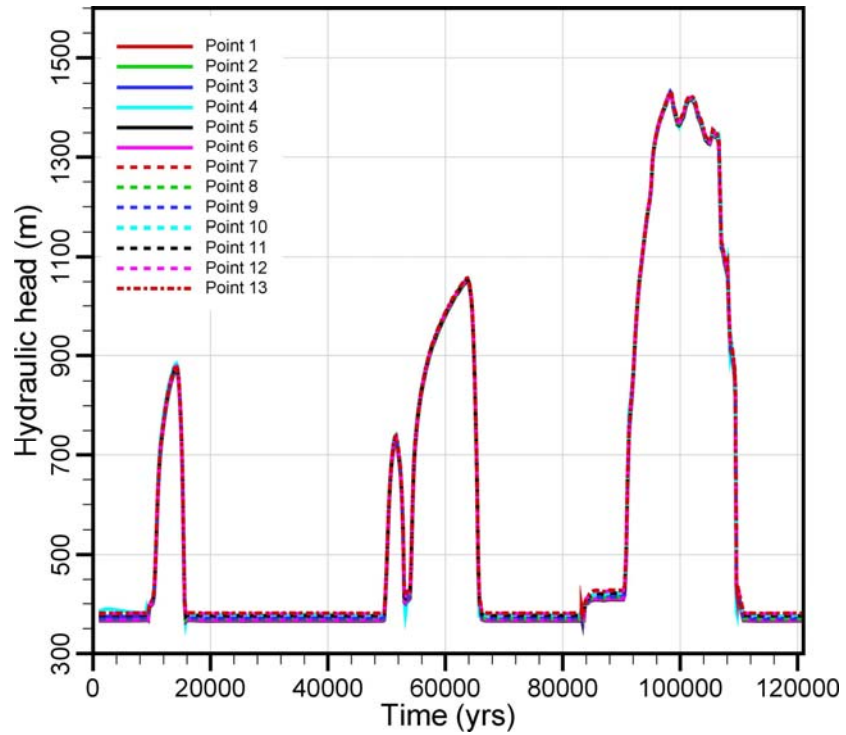
Figure 36: Temporal Evolution of Equivalent Freshwater Heads Predicted at Selected Locations by the Slice 2 THM Simulation
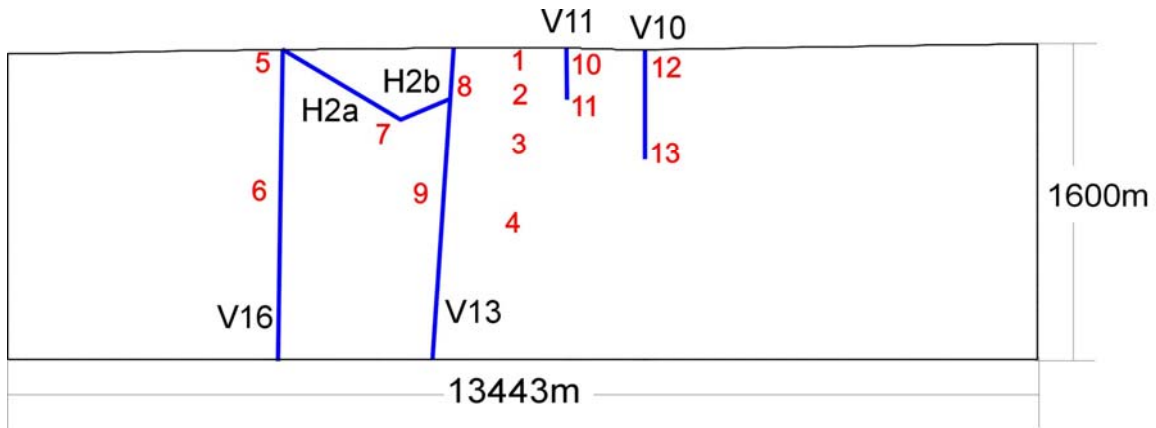
Figure 37: Locations Selected in Slice 2 for Graphic Display of Temporal Evolution of Simulation Results. Vertical exaggeration: Approximately 2.5X
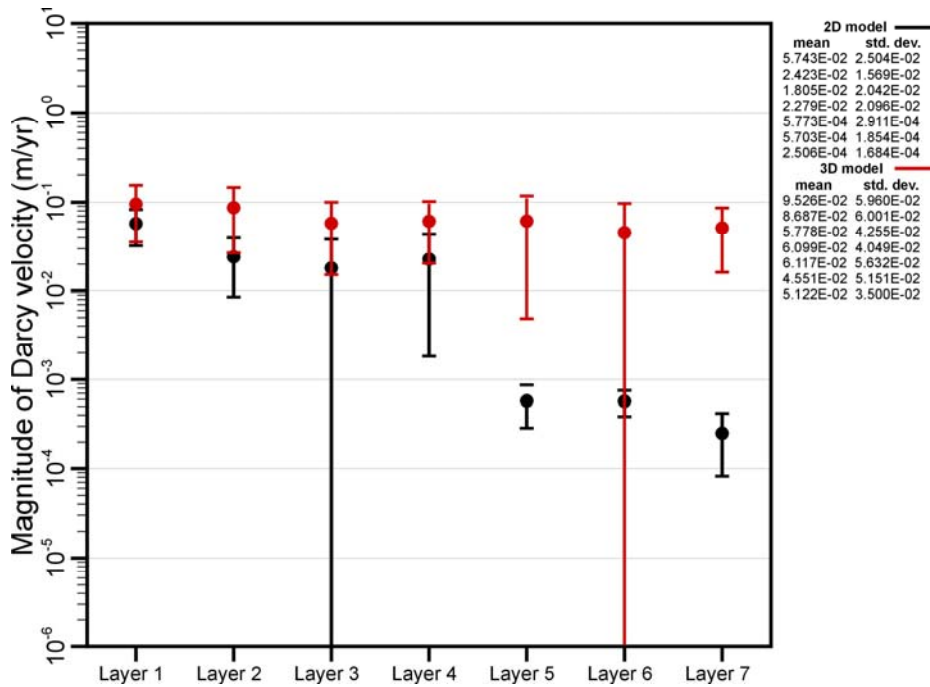
Figure 38: Comparison of Mean and Standard Deviation of Darcy Velocity Magnitude in FZs as Predicted by the 2D Slice 2 THM Simulation (Black) and in Elements Intersected by Slice 2 in the 3D S_THM Model (Red) at Depths Corresponding to Different Rock Mass Permeability Layers at 109.3 kyr

Figure 39: Meltwater Recharge Paths Estimated by Tracking 137 Water-Coincident Particles Released into the Transient Flow Field Predicted by the 2D THM Simulation Using the Cold-based Glacial Scenario
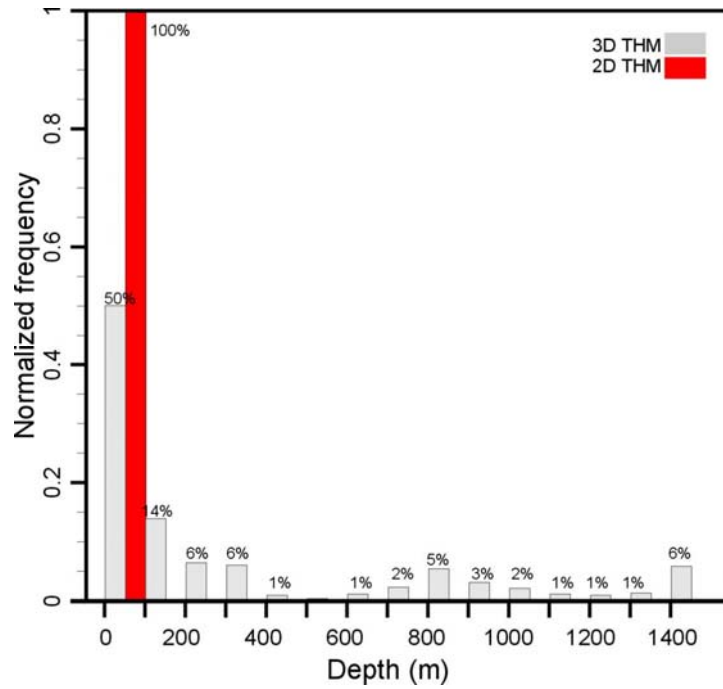
Figure 40: Normalized Histogram of Maximum Depth of Meltwater Recharge as Predicted by the 2D & 3D S_THM Simulations Over the Entire Depth of the Model

a).
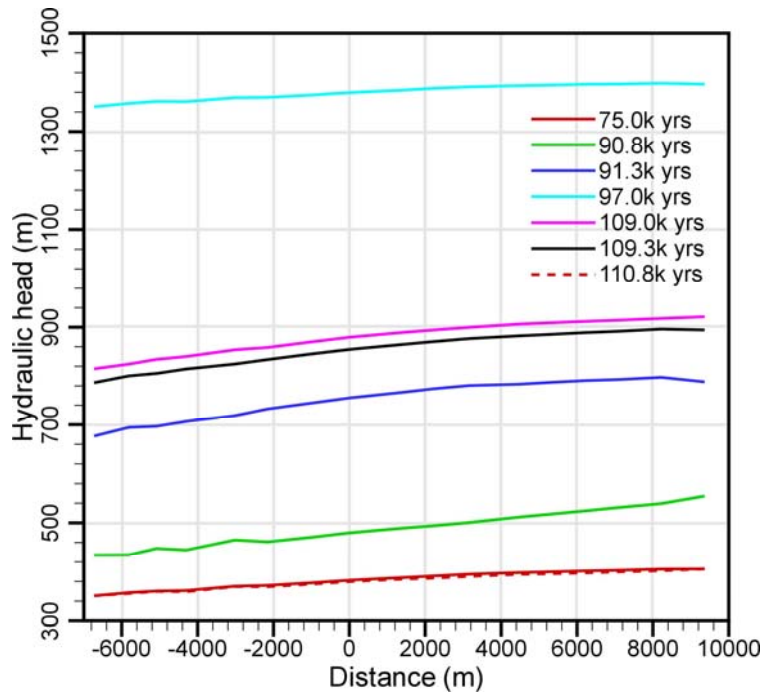
b).
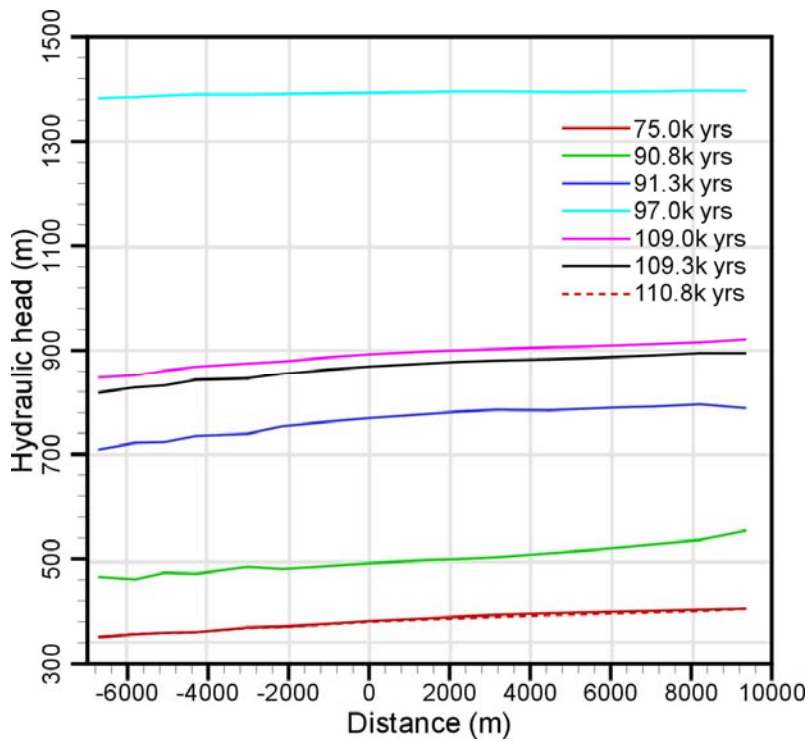
Figure 41: Hydraulic Head Versus Distance Along a Line at 670-M Below Surface for Specified Times as Predicted by the a) R_THM and b) S_THM Simulations

a).
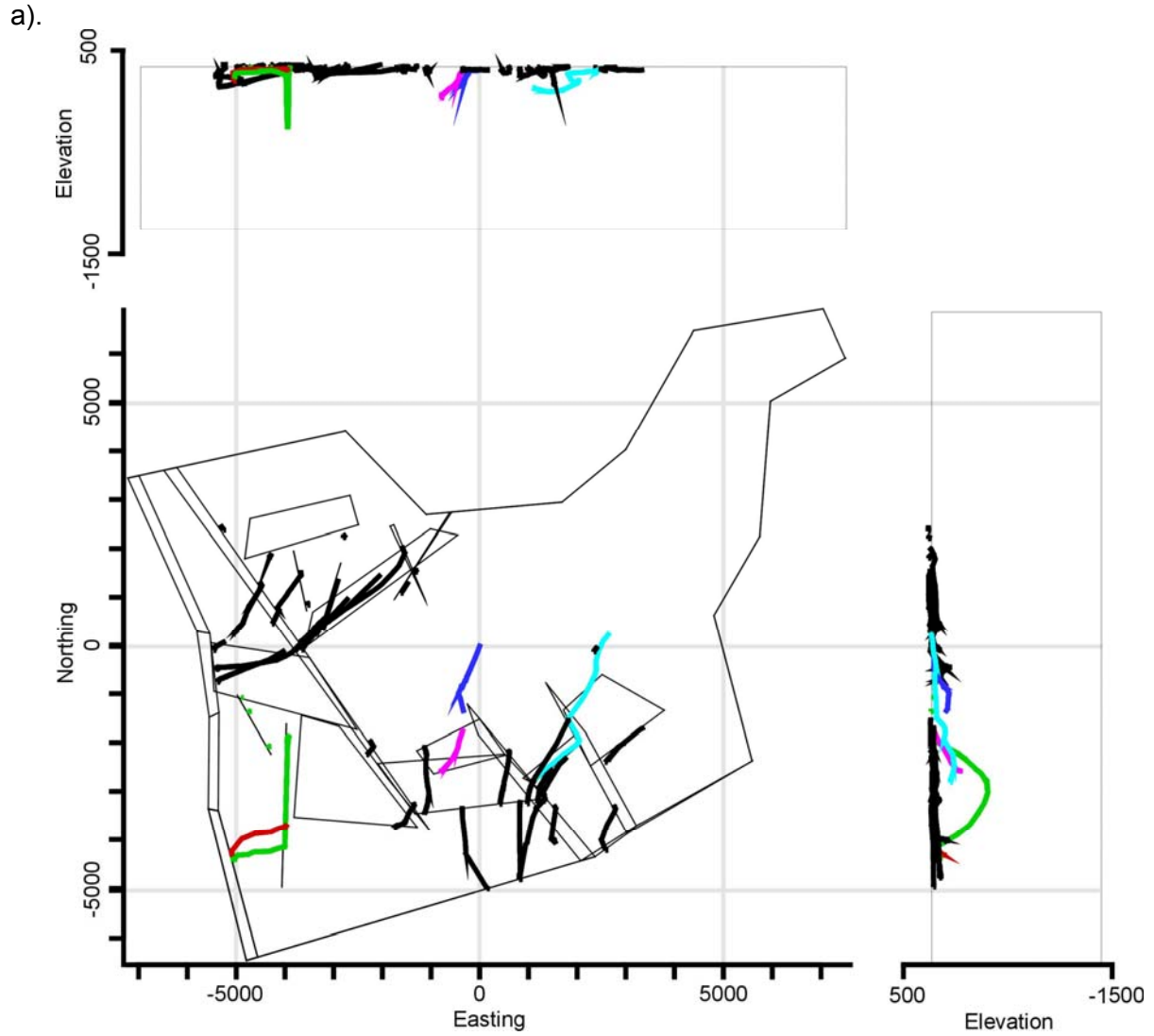
Figure 42a: Plan and Section Views of 38 Particle Tracks Starting at Beginning of Meltwater Production According to 3D R_THM. Deepest particle paths are highlighted by Colour.

b).
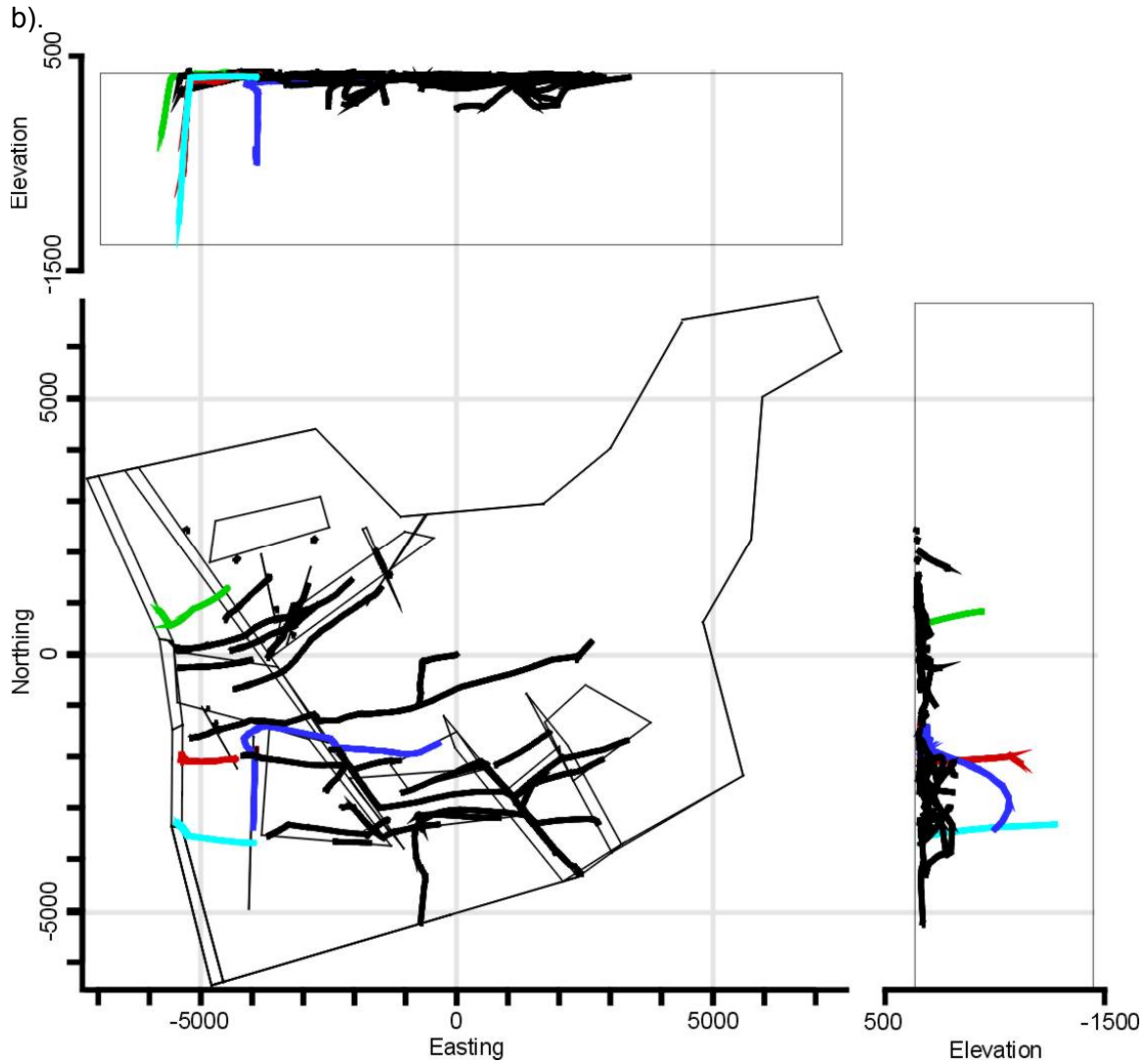
Figure 42b: Plan and Section Views of 38 Particle Tracks Starting at Beginning of Meltwater Production According to 3D S_THM Simulations. Deepest particle paths are highlighted by colour.
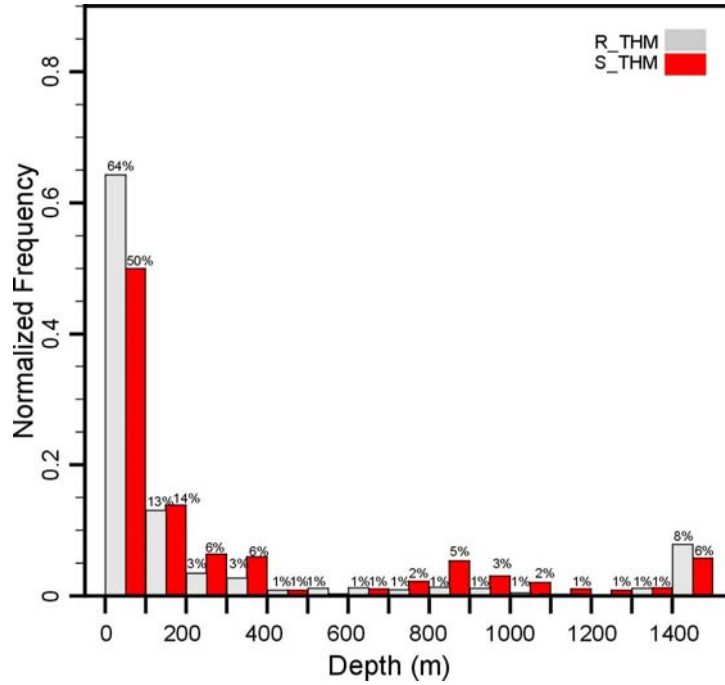
Figure 43: Normalized Histogram of Maximum Depth of Meltwater Recharge as Predicted by the 3D R_THM and S_THM Simulations over the Entire Depth of the Model
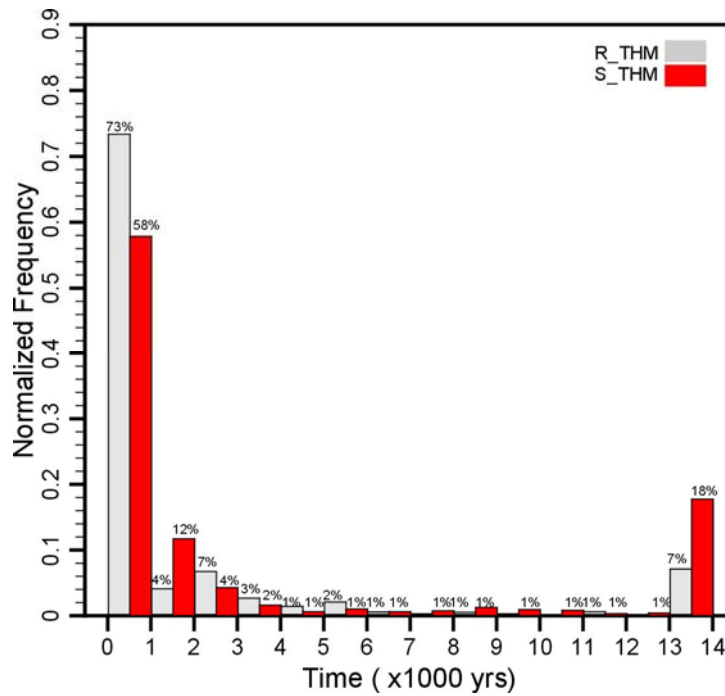
Figure 44: Normalized Histogram of Time for Meltwaters to Recharge to Maximum Depth as Predicted by the 3D R_THM and S_THM Simulations
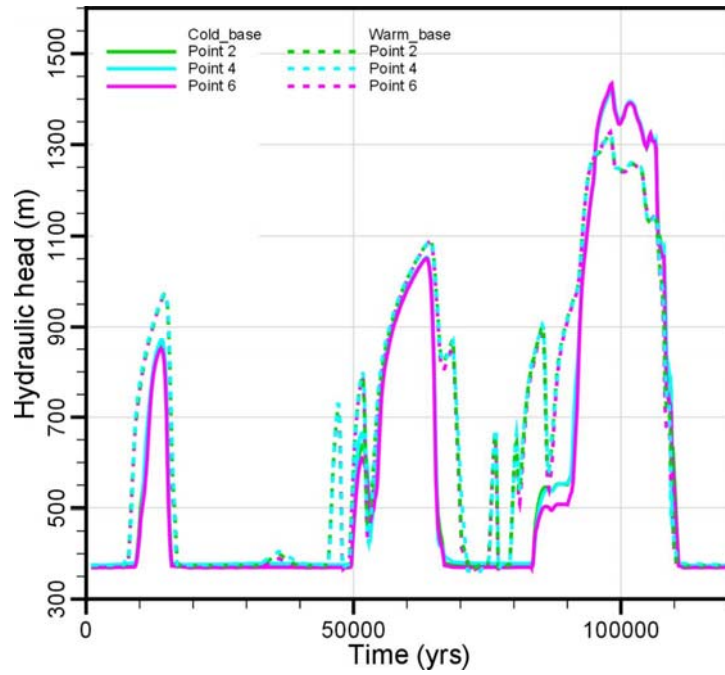
Figure 45: Comparison Of Temporal Evolution of Hydraulic Heads for 3 Points for the 2D THM Simulations Using Cold-based and Warm-based Glacial Scenarios
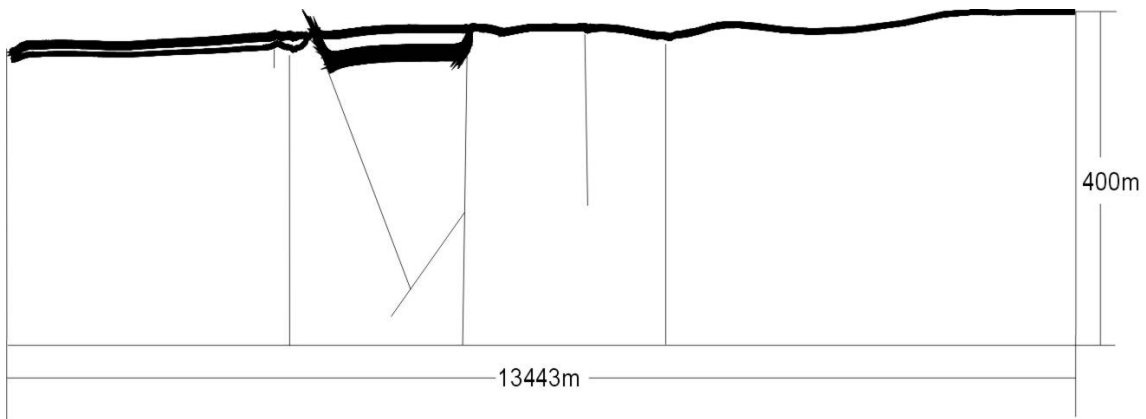
Figure 46: Meltwater Recharge Paths Estimated by Tracking 137 Water-Coincident Particles Released into the Transient Flow Field Predicted by the 2D THM Simulation Using the Warm-Based Glacial Scenario
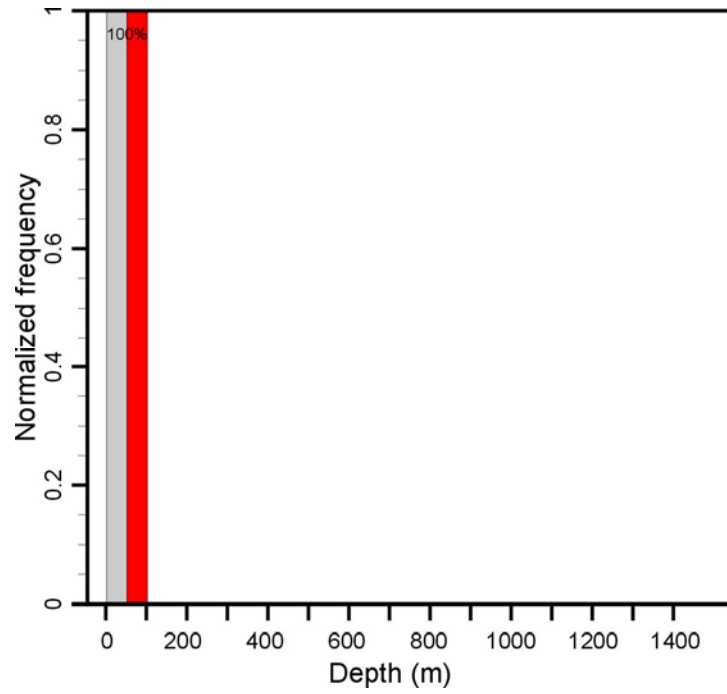
Figure 47: Normalized Histograms of Maximum Meltwater Penetration According to 2D THM Simulations for Cold-based and Warm-based Glacial Scenarios

a).
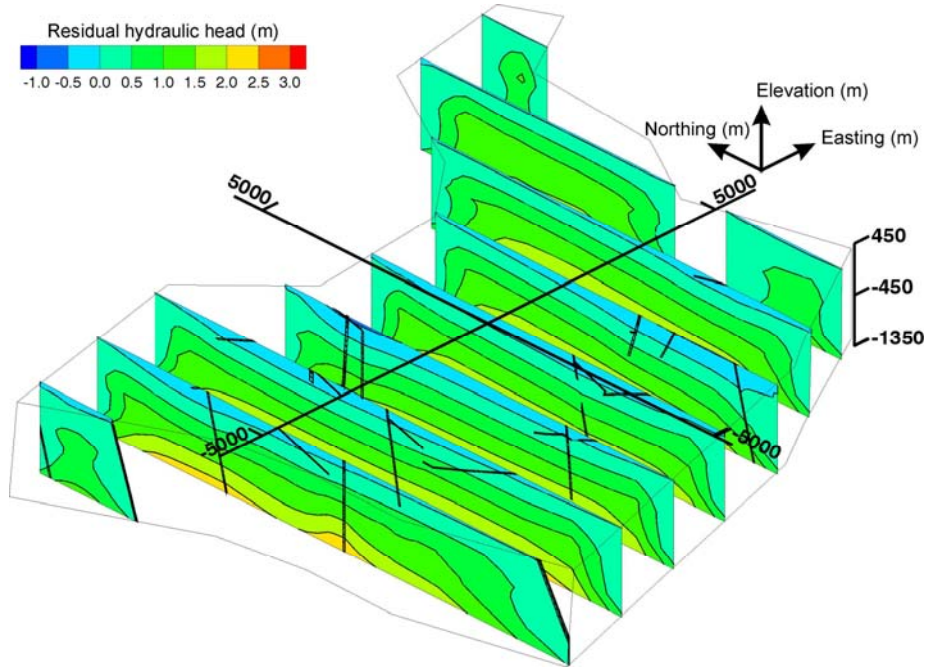
b).
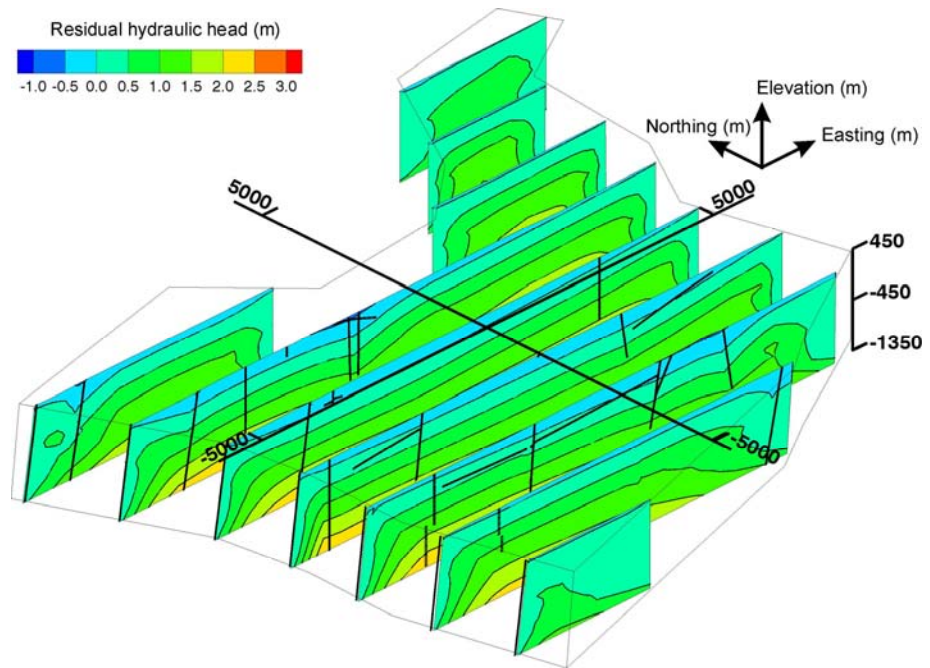
Figure 48: Anomalous Head Contours Predicted by 3D Simulation Run R_HM Plotted on a) NS and b) EW Planes
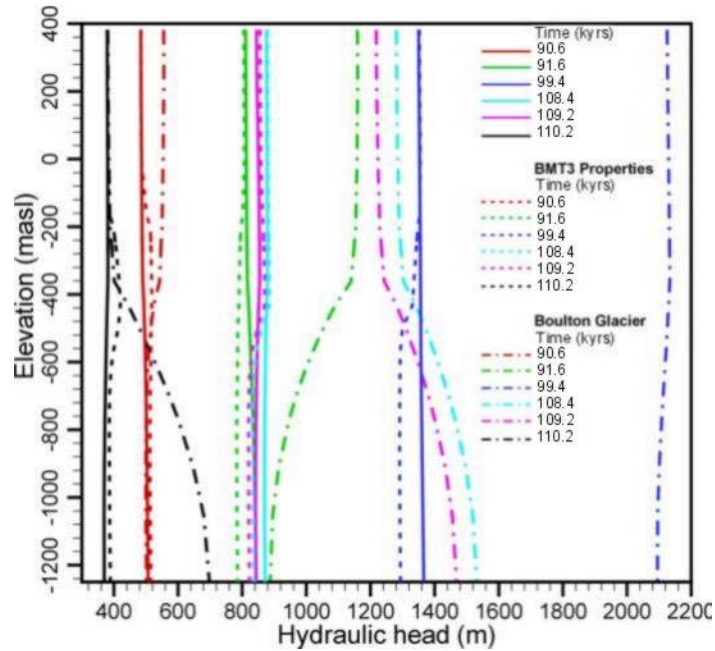
Figure 49: Vertical Profiles of Equivalent Freshwater Head at Various Model Times as Predicted by Three Sensitivity Analysis R_HM Simulation Runs. LGM is close to 98 kyr and Cycle 3 glacial retreat is complete at 109.6 kyr.
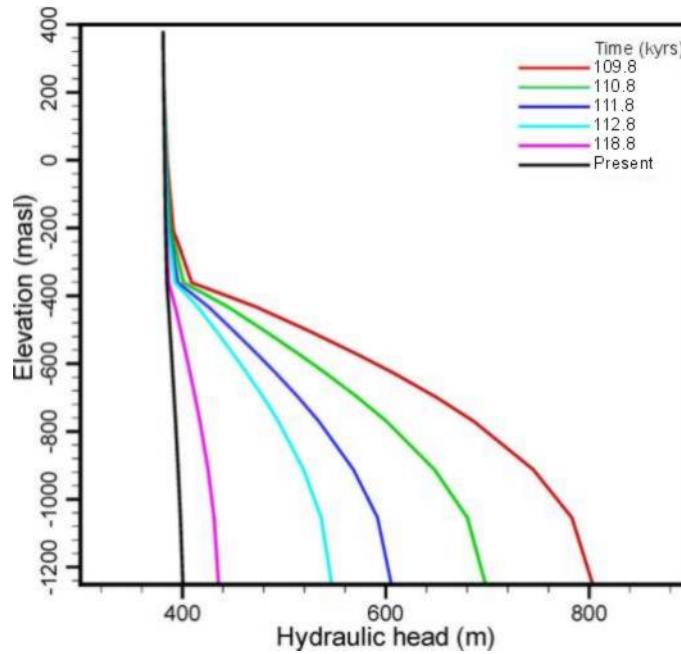
Figure 50: Vertical Profiles of Hydraulic Head Following Cycle 3 Glacial Retreat as Predicted by HM Simulation Run GC2
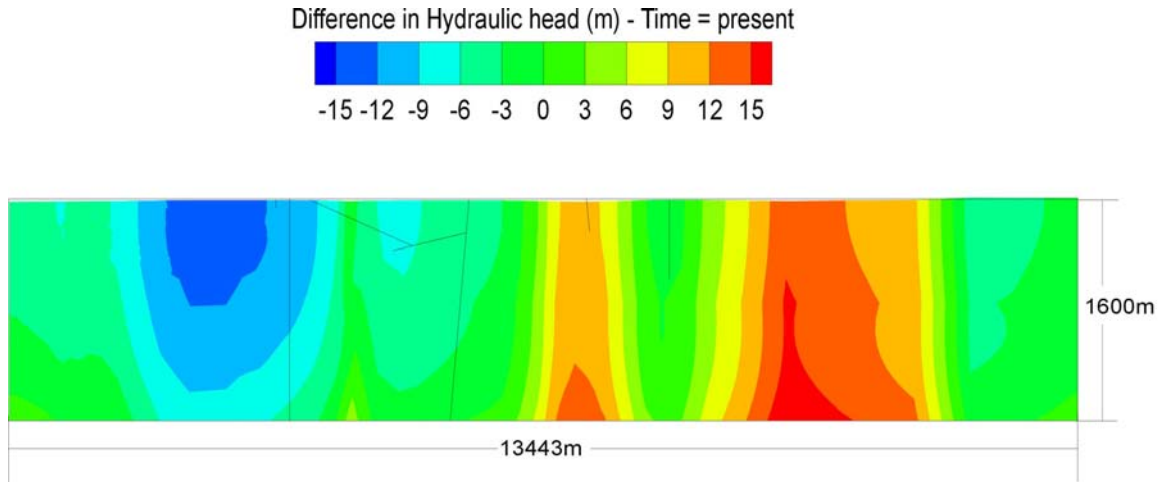
Figure 51: Anomalous Head Contours Predicted by the 2D HM Simulation Using the Cold-based Glacial Scenario
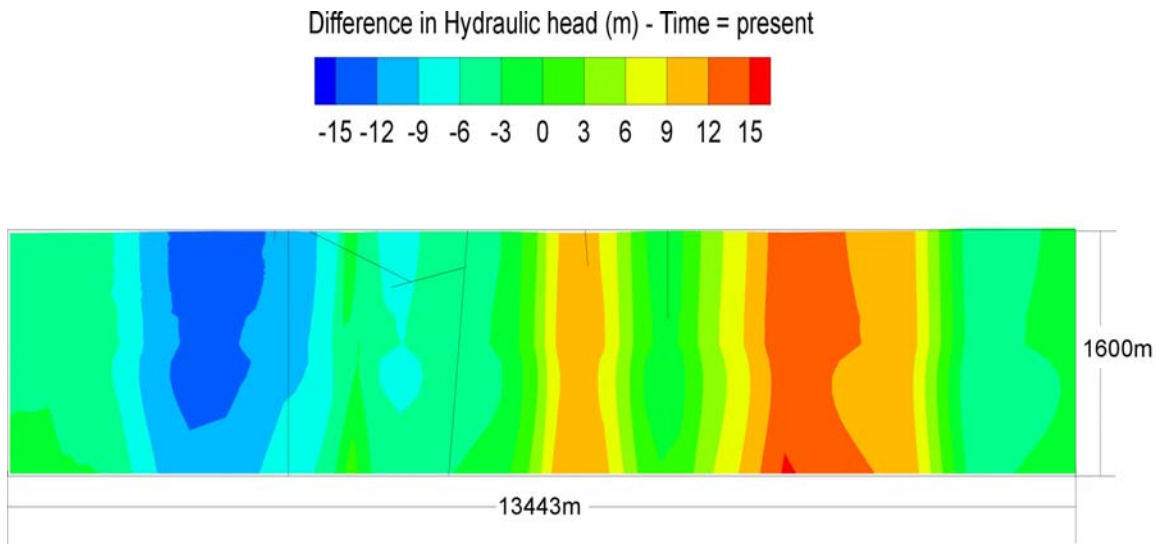
Figure 52: Anomalous Head Contours Predicted by the 2D THM Simulation Using the Cold-based Glacial Scenario
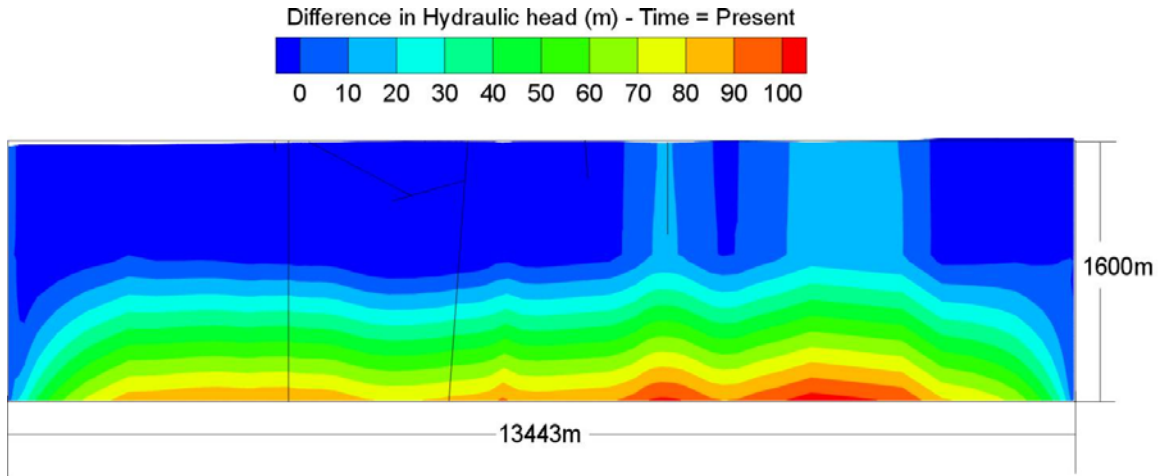
Figure 53: Anomalous Head Contours Predicted by the 2D THMC Simulation Using the Cold-based Glacial Scenario
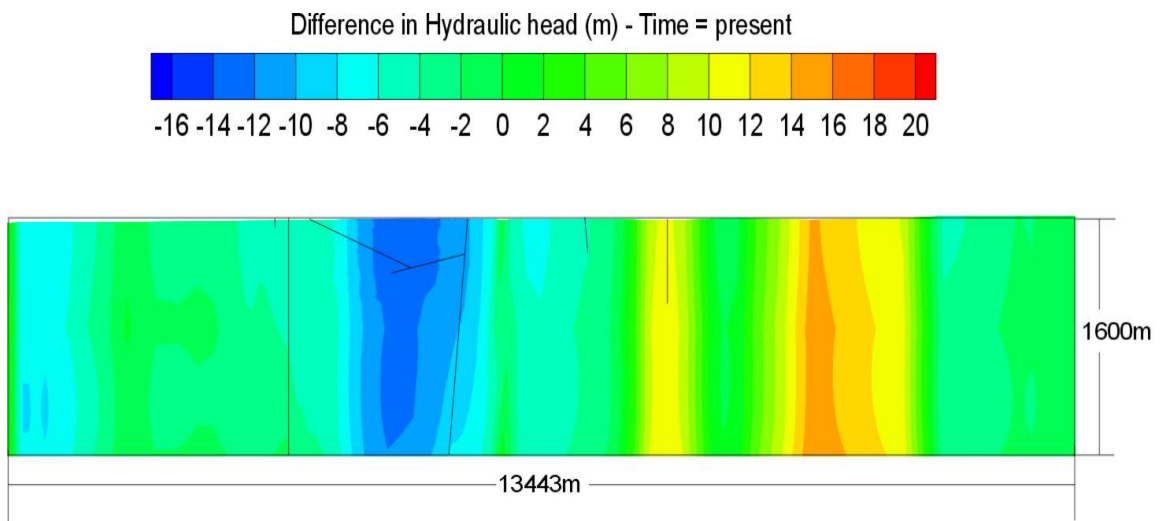
Figure 54: Anomalous Head Contours Predicted by the 2D THM Simulation Using the Warm-based Glacial Scenario
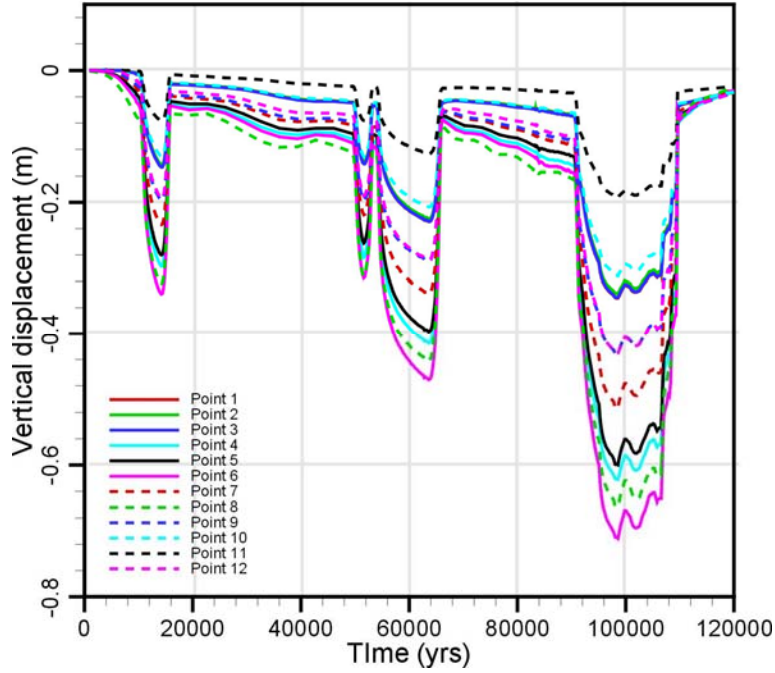
Figure 55: Temporal Evolution of Vertical Displacement from the R_THMC (THM with Depth Dependent Salinity) Simulation
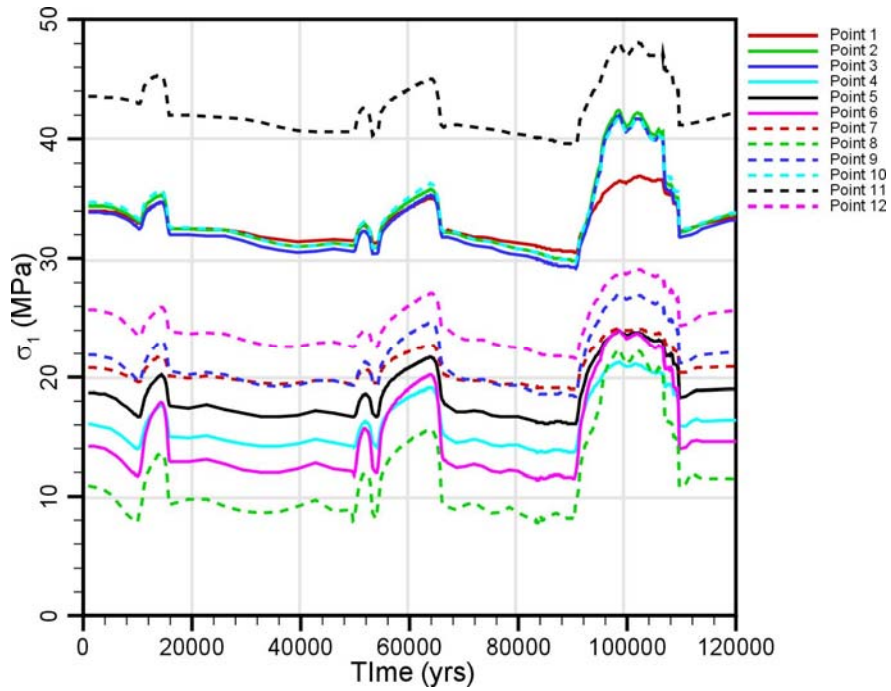
Figure 56: Temporal Evolution of Maximum Principal Effective Stress from the R_THMC (THM with Depth Dependent Salinity) Simulation
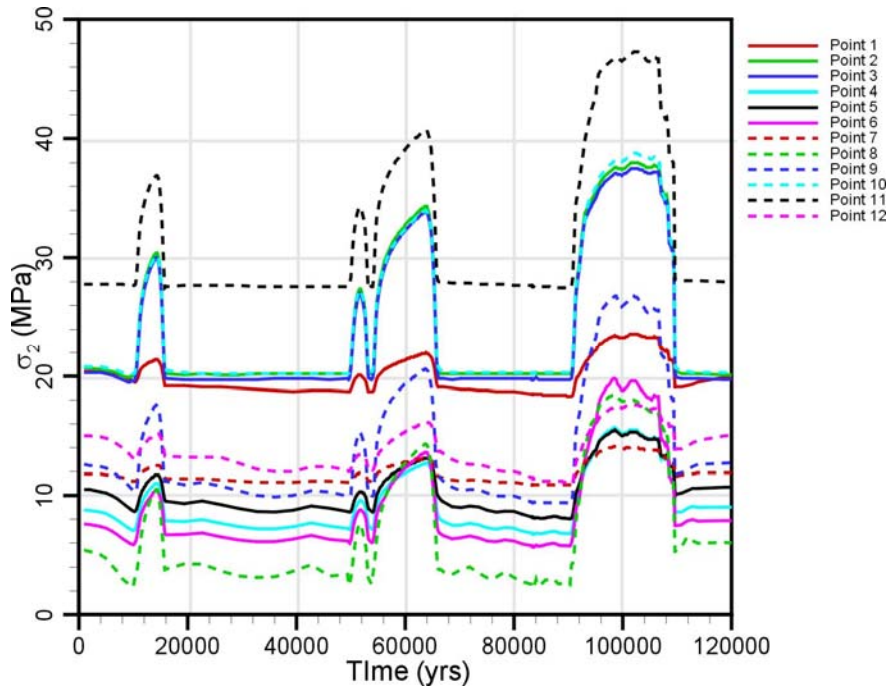
Figure 57: Temporal Evolution of Intermediate Principal Effective Stress from the R_THMC (THM with Depth Dependent Salinity) Simulation
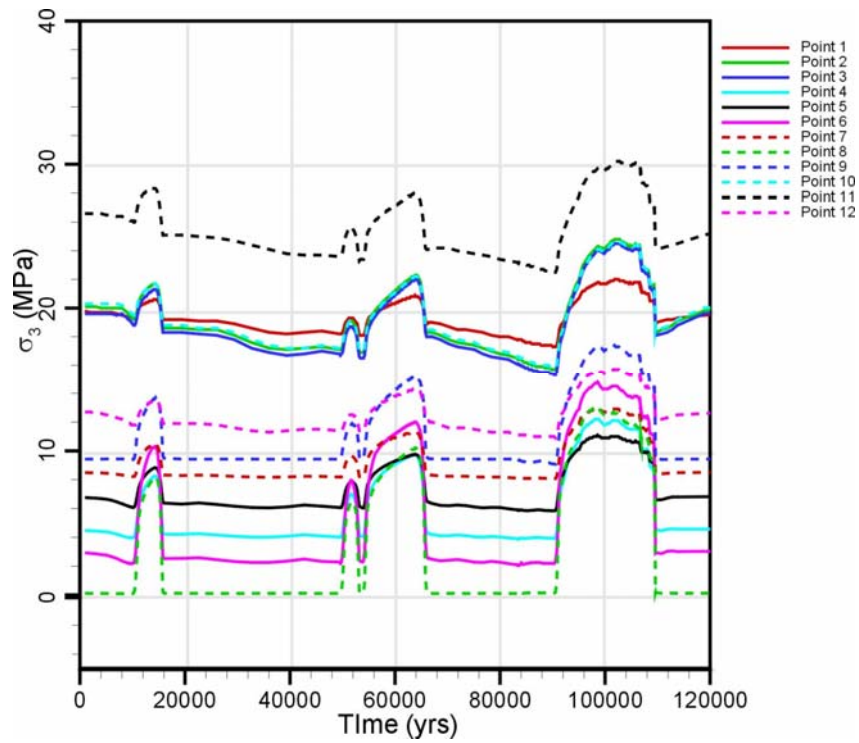
Figure 58: Temporal Evolution of Minimum Principal Effective Stress from the R_THMC (THM with Depth Dependent Salinity) Simulation

a).
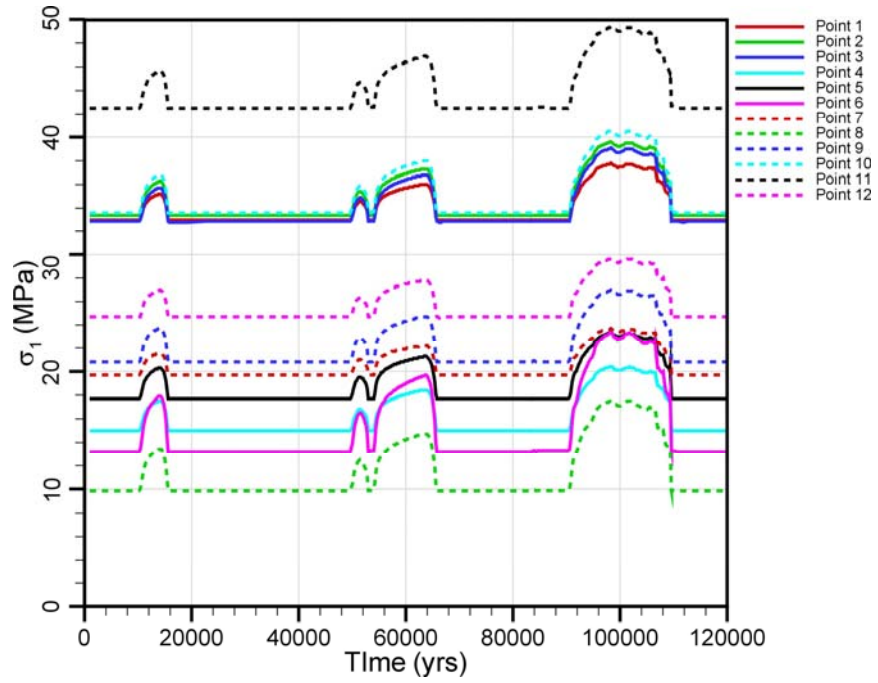
b).
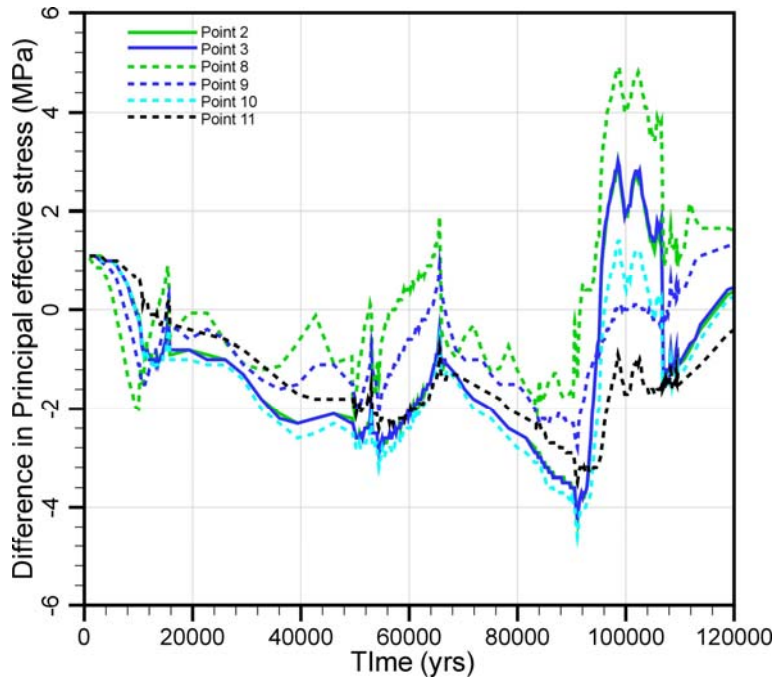
Figure 59: Temporal Evolution of a) Maximum Principal Effective Stress from the R_HM Simulation and b) The Difference in the Maximum Principal Effective Stress for Selected Points in the RM for the R_HM and R_THMC Simulations
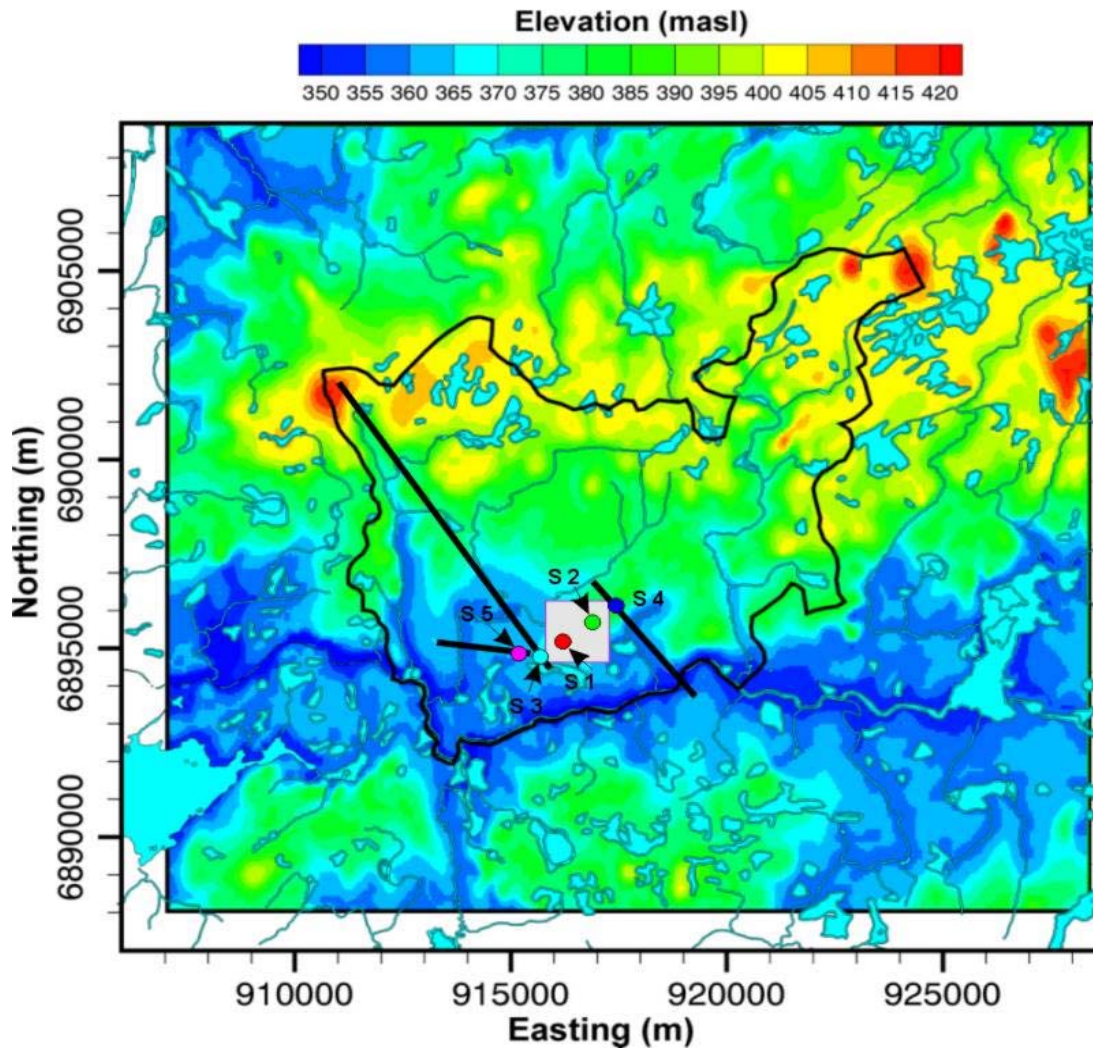
Figure 60: Locations in Rock Mass (S1 and S2) and in Nearby Subvertical Fracture Zones (S3 and S4), Together With a Point (S5) in a LID Utilized to Illustrate THM Stress Reorientation and Stability Analysis
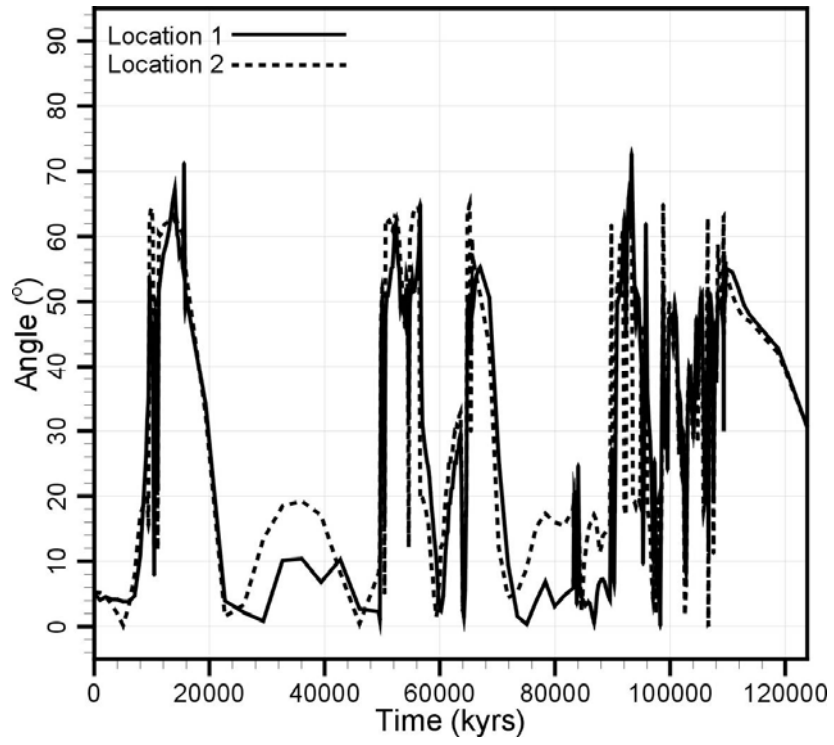
Figure 61: Rotation of Intermediate Principal Effective Stress as a Function of Time According to the R_THM Simulation for Locations S1 and S2 Depicted in Figure 60
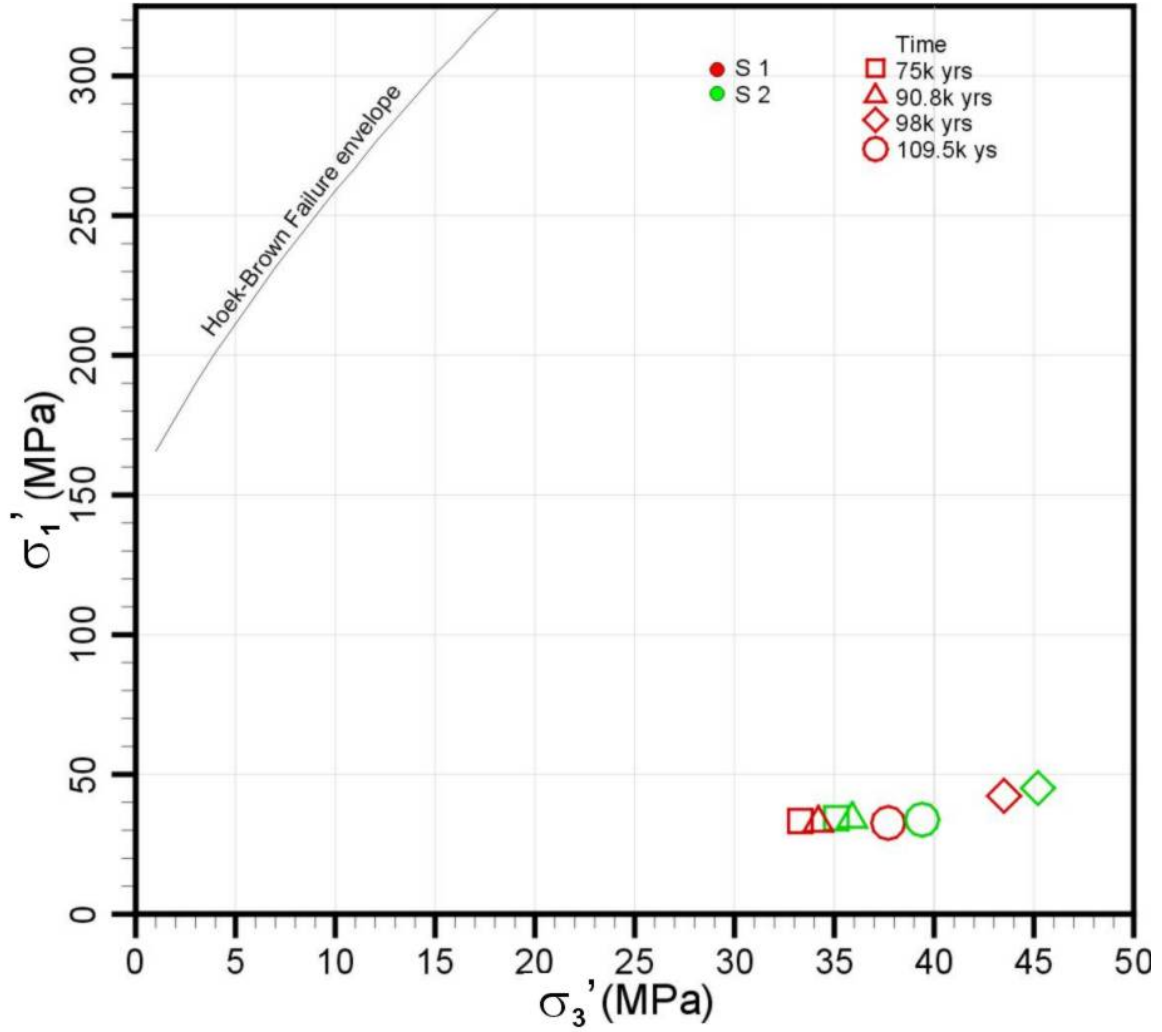
Figure 62: Effective State of Stress at Various Times from the R_THM Simulation for Points S1 and S2 in Rock Mass Relative to the Hoek-Brown Failure Envelope
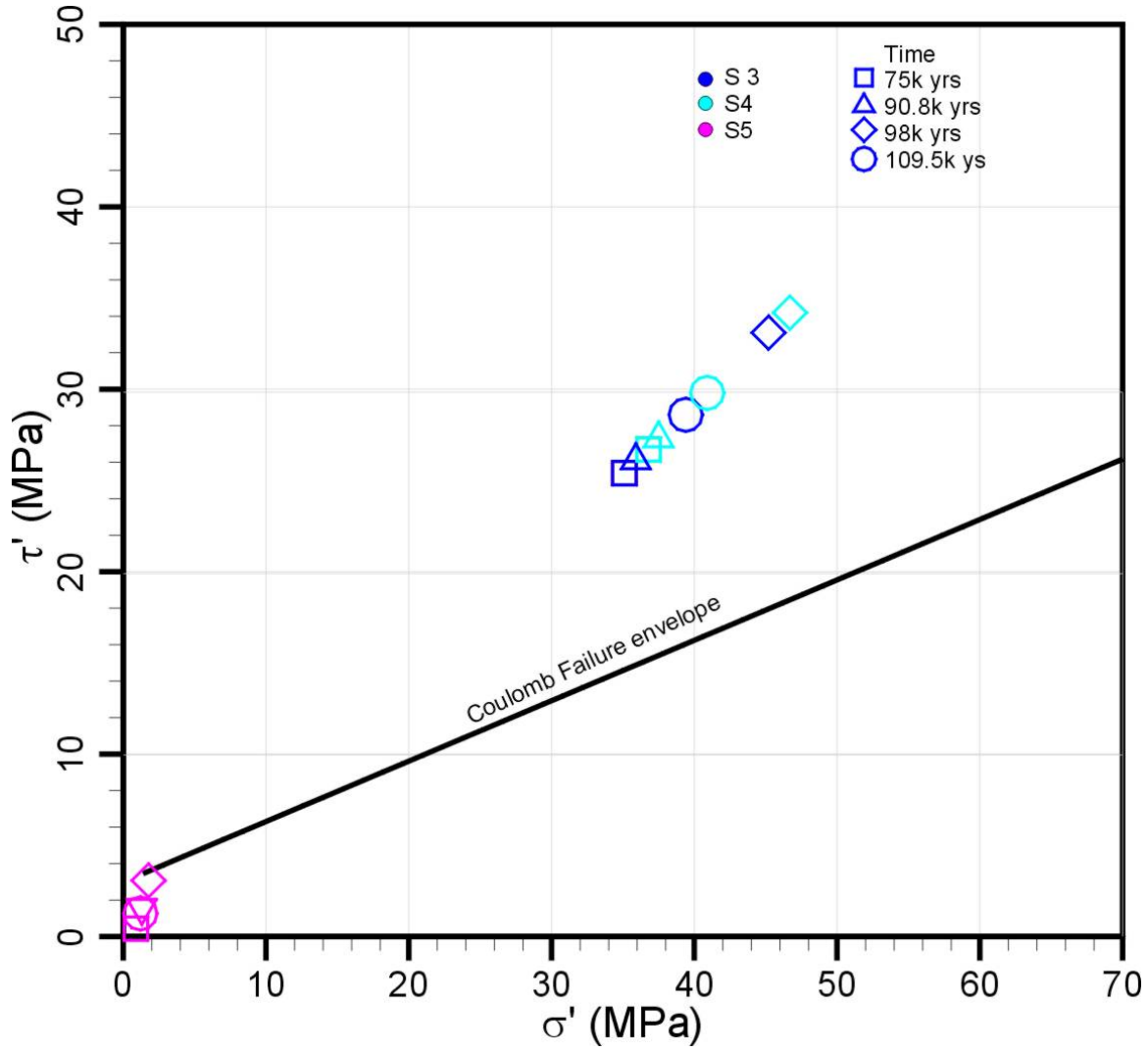
Figure 63: Effective State of Stress at Various Times from the R_THM Simulation for Points S3, S4 and S5 in Fracture Zones Relative to the Coulomb Failure Envelope

a).
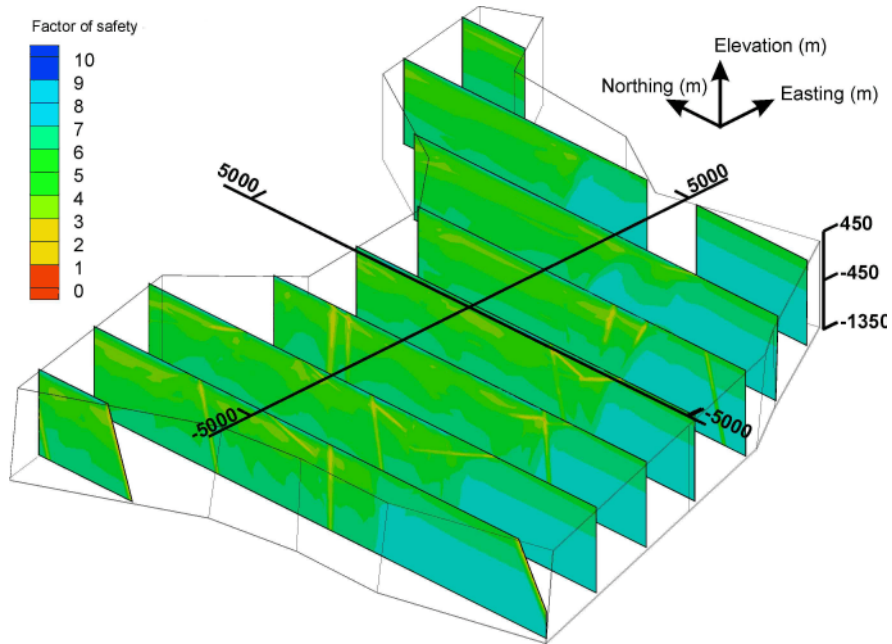
b).
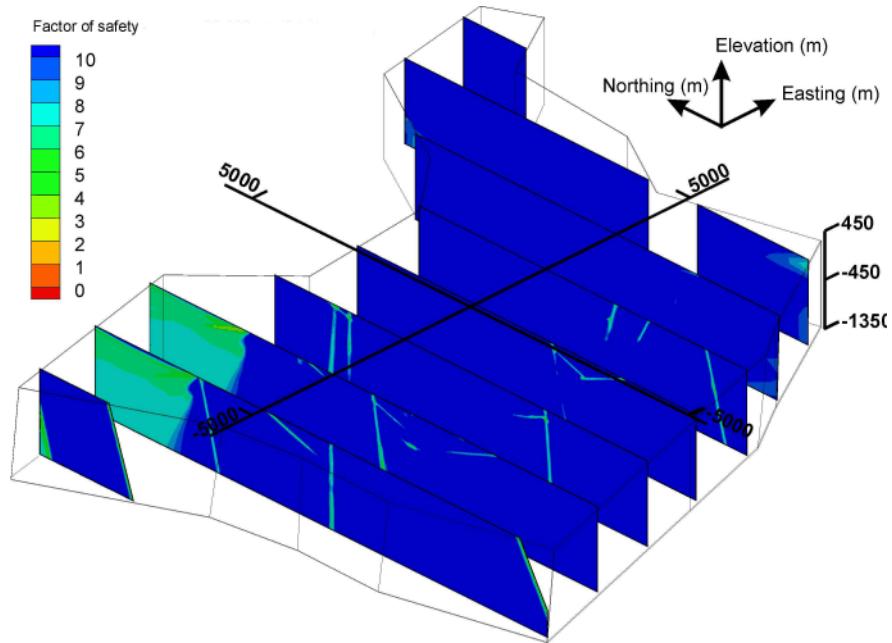
Figure 64: Predicted Distribution of Mechanical Factor of Safety from R_THM Model: a) at 90,800 Years, b) at 98,000 Years
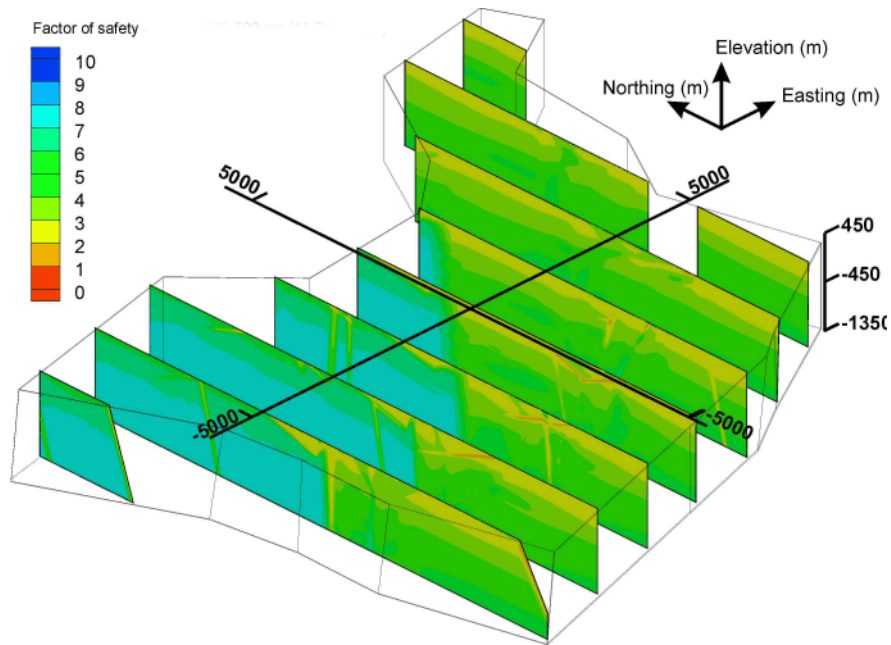
Figure 64 (continued): Predicted Distribution of Mechanical Factor of Safety from R_THM Model: c) at 109,300 Years
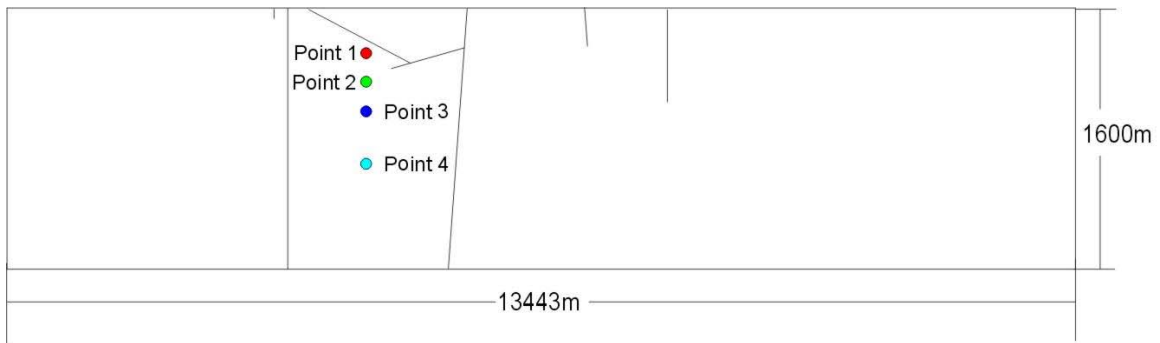
Figure 65: Points in the Rock Mass Located at Elevations of 130, -130, -320 and –680 masl Selected for Effective State of Stress and Mechanical Stability Analysis According to 2D Modelling
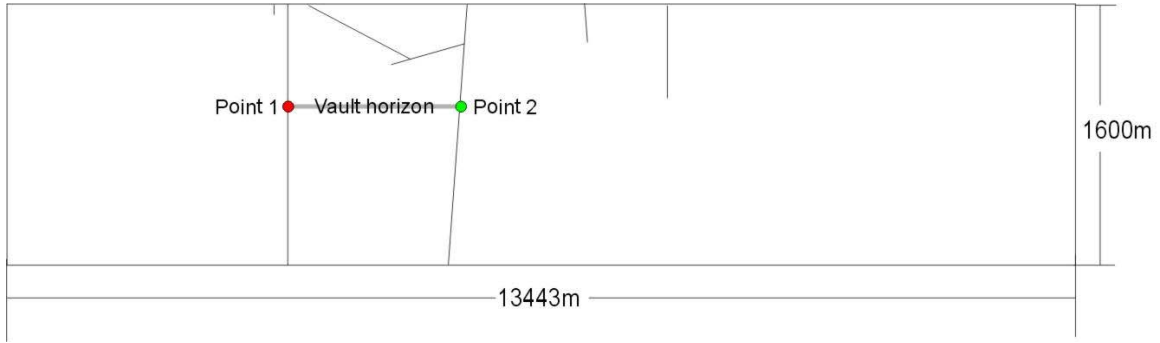
Figure 66: Points Located at 670-m Depth Below Surface in Fracture Zones Selected for Illustrating Effective State of Stress and Mechanical Stability Analysis

Cold-based THM Case
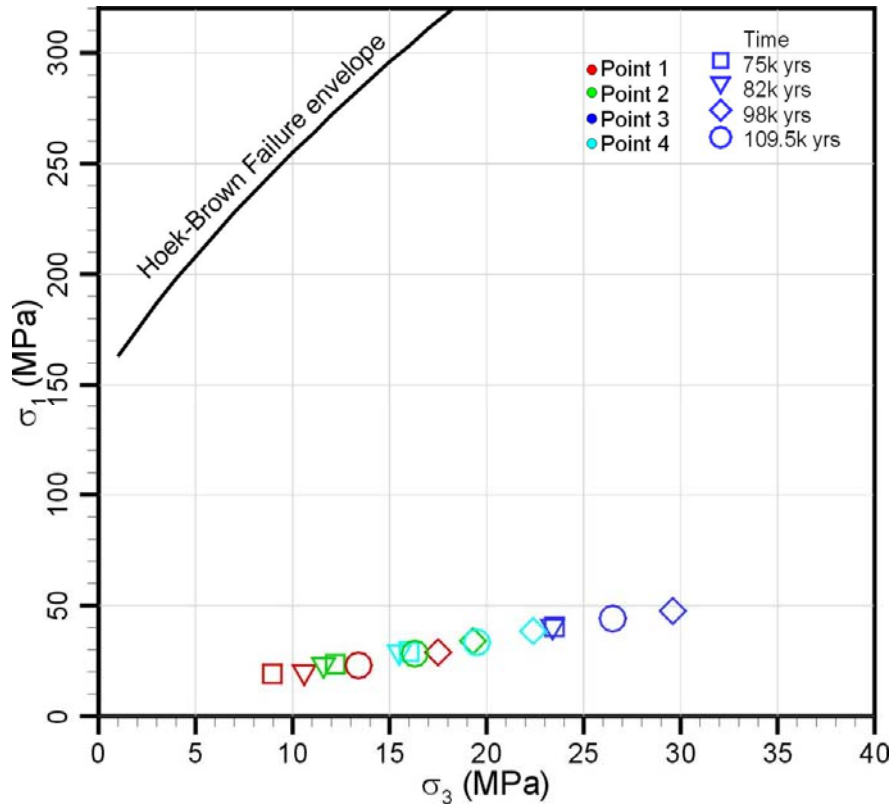
Figure 67: Effective State of Stress for Four Points in the Rock Mass at Various Times According to the 2D THM Simulation Using the Cold-based Glacial Scenario Relative to the Hoek-Brown Failure Envelope

**Warm-based THM Case**
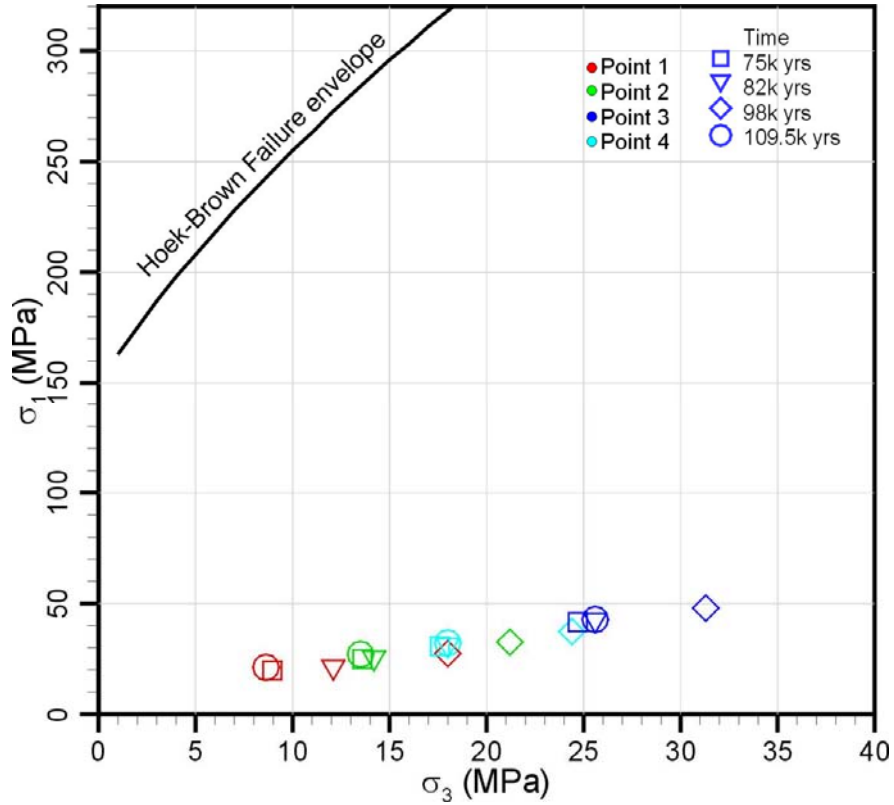
Figure 68: Effective State of Stress for Four Points in the Rock Mass at Various Times According to the 2D THM Simulation Using the Warm-based Glacial Scenario Relative to the Hoek-Brown Failure Envelope
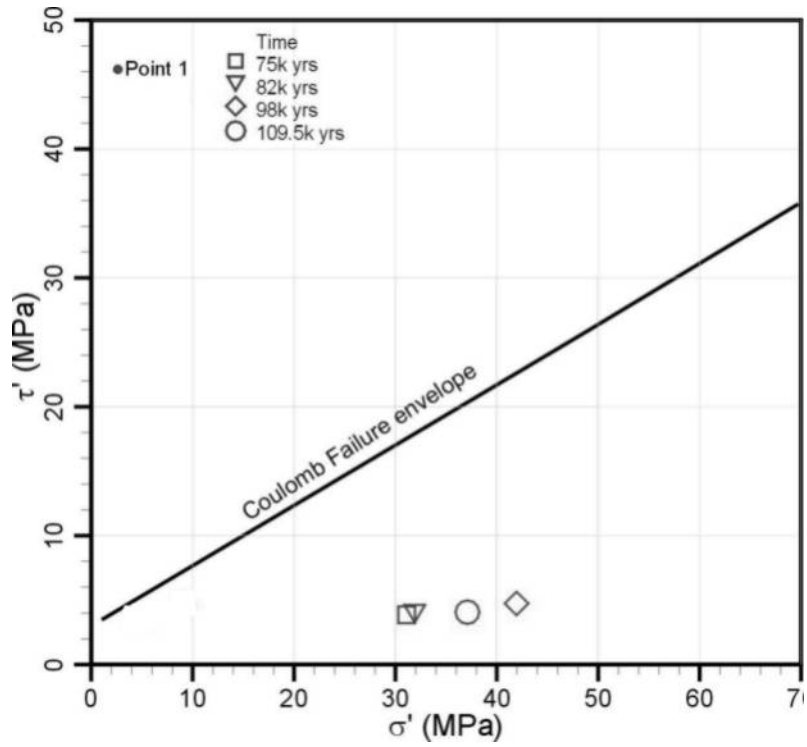
Figure 69: Effective State of Stress for Point 1 (see Figure 66) in a Fracture Zone at Various Times According to the 2D THM Simulation Using the Cold-based Glacial Scenario Relative to the Coulomb Failure Envelope
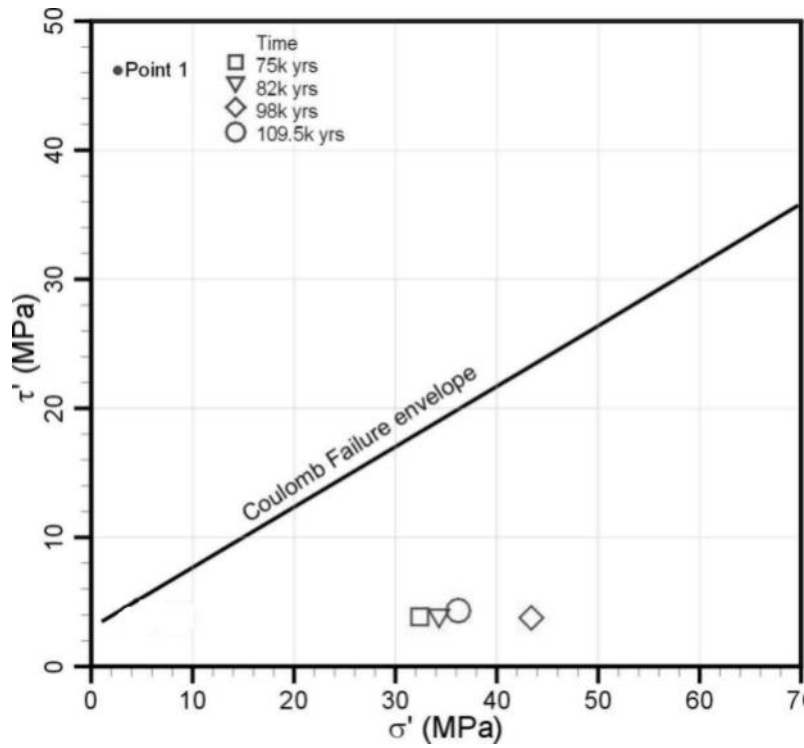
Figure 70: Effective State of Stress for Point 1 (see Figure 66) in a Fracture Zone at Various Times According to the 2D THM Simulation Using the Warm-based Glacial Scenario Relative to the Coulomb Failure Envelope
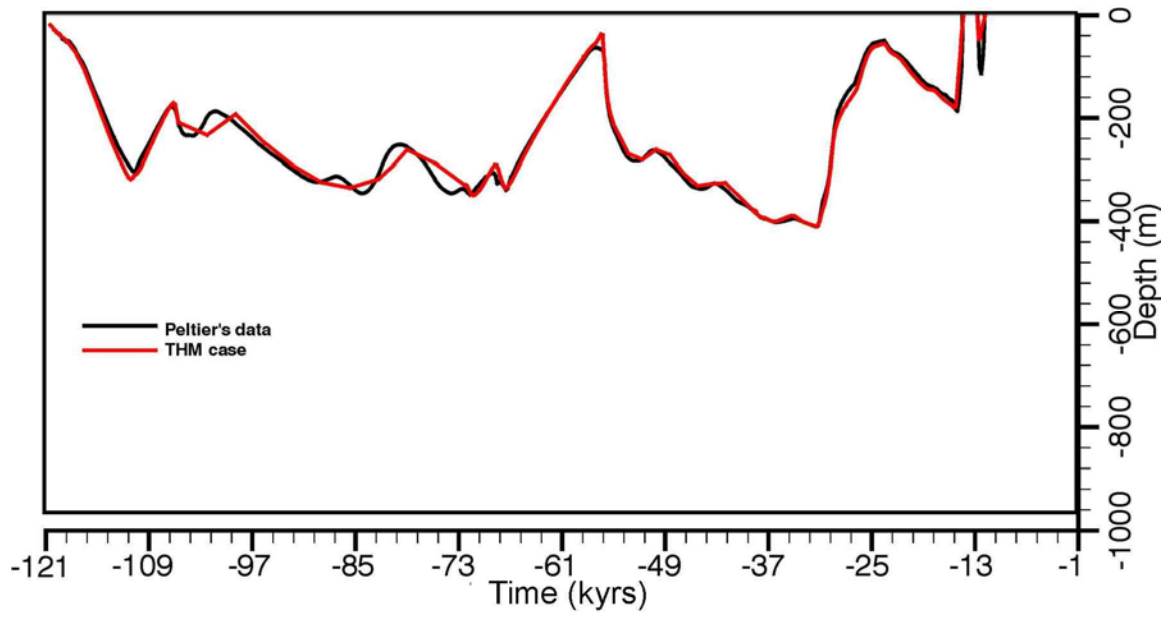
Figure 71: Comparison of Temporal Evolution of 0°C Isotherm Predicted by the 3D Task E THM Model and Peltier's Model (2004)
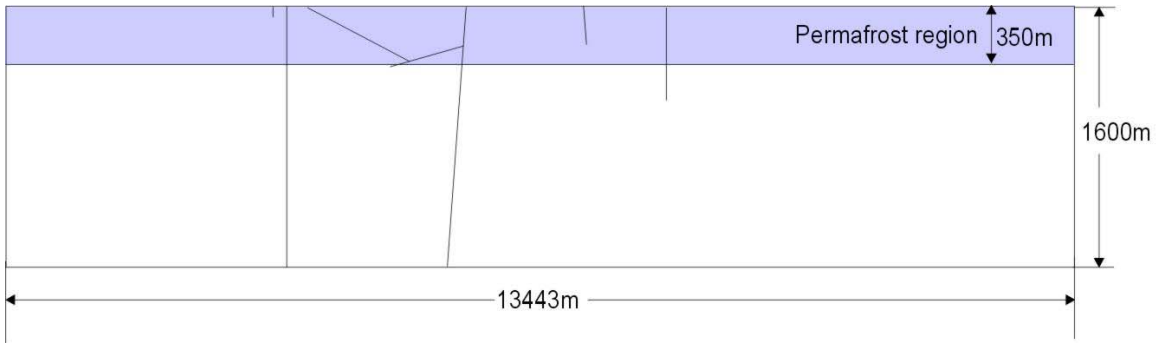
**Figure 72: Region Assigned to Permafrost for Simple Permafrost HMC Modelling**
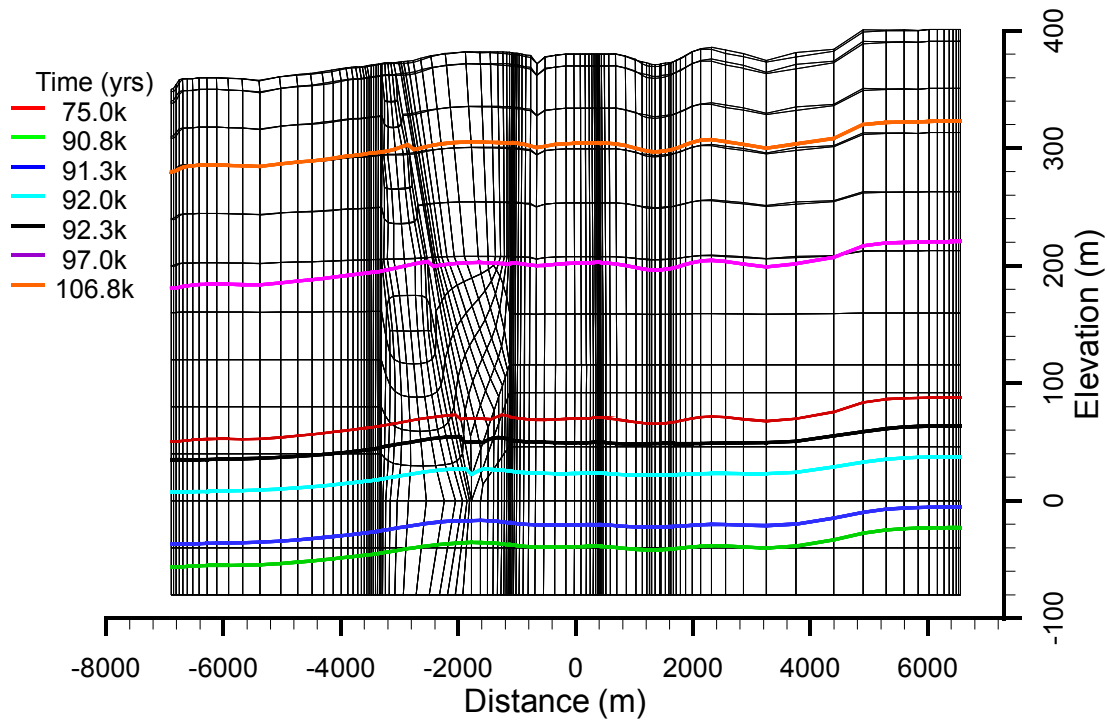
**Figure 73: Variation of Pressure-Adjusted Freezing Point with Horizontal Distance at Various Times**
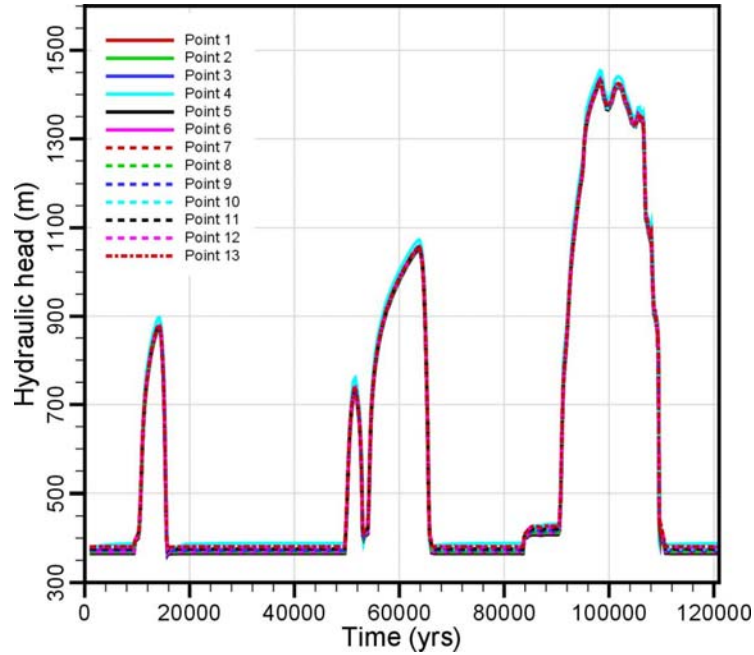
Figure 74(a): Temporal Evolution of Predicted Hydraulic Head at Selected Locations for the 2D HMC Model Using the Cold-based Glacial Scenario with No Permafrost Represented
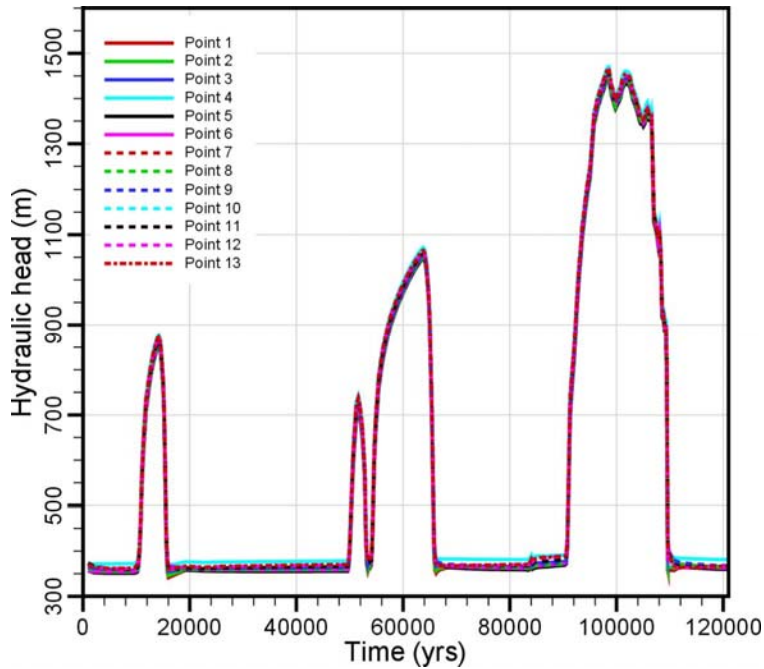

Figure 74(b): Temporal Evolution of Predicted Hydraulic Head at Selected Locations for the 2D HMC Model Using the Cold-based Glacial Scenario with a Constant and Uniform 350-m Thick Layer of Permafrost Represented as a Low-Permeability Unit
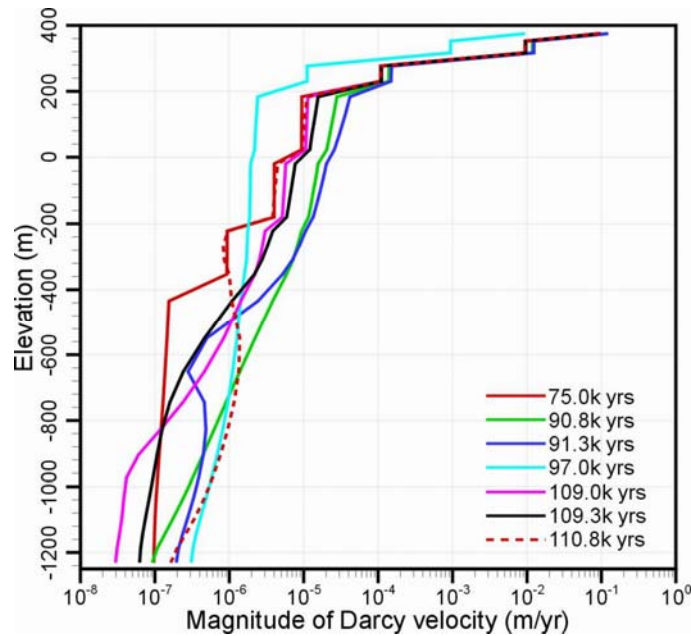
Figure 75(a): Darcy Velocity Magnitude Profile in Rock Mass Along Vertical Line Through Origin (X=0, Y=0) of Model at Various Times During the Third Glacial Cycle as Predicted by the 2D HMC Simulation with No Permafrost Represented.
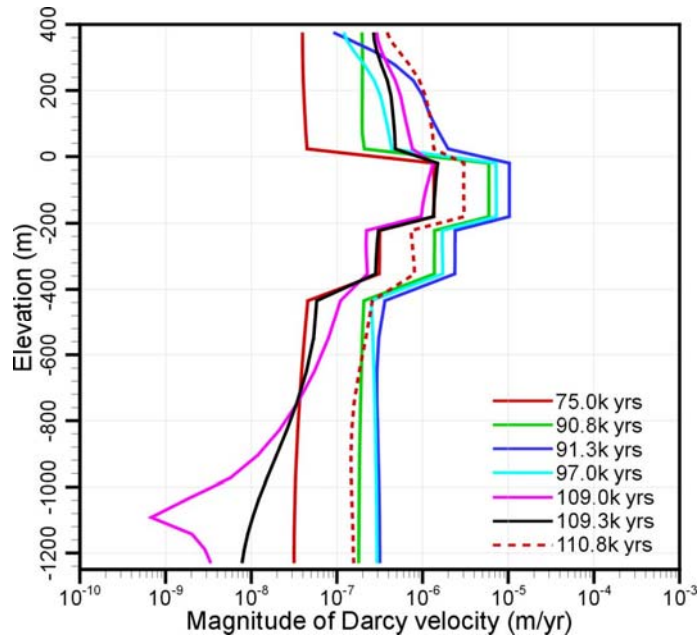

Figure 75(b): Darcy Velocity Magnitude Profile in Rock Mass Along Vertical Line Through Origin (X=0, Y=0) of Model at Various Times During the Third Glacial Cycle as Predicted by the 2D HMC Model Using the Cold-based Glacial Scenario with a Constant and Uniform 350-m Thick Layer of Permafrost Represented as a Low-Permeability Unit
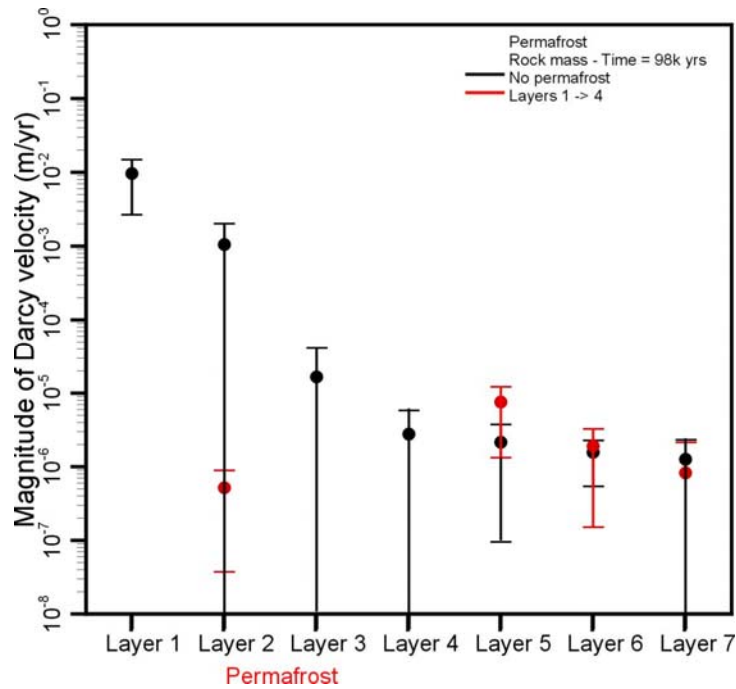
Figure 76: Comparison of Mean and Standard Deviation Of Darcy Velocity Magnitude in Different Rock Mass Permeability Units (Layers) as Predicted by the 2D HMC Simulation Runs at 98 kyr Using the Cold-based Glacial Scenario: With No Permafrost (Black) and With A Constant and Uniform 350-m Thick Layer of Permafrost Represented as a Low-Permeability Unit (Red)

An Addendum to this report contains Attachment 1, Attachment 2 and associated appendices that give further details on Task E activities including conceptual model development and early HM/THM simulations. It is available upon request as a separate document.